REPORT DOCUMENTATION PAGE

AFRL-SR-AR-TR-03-

0068

1. REPORT DATE (DD-MM-YYYY)	2. REPORT TYPE	3. DATES COVERED (From - To)
23/01/2003	Final technical	2/15/2000-9/30/2002

4. TITLE AND SUBTITLE
(U) PDF Modelling of Turbulent Combustion

5a. CONTRACT NUMBER

5b. GRANT NUMBER
F49620-00-1-0171

5c. PROGRAM ELEMENT NUMBER

6. AUTHOR(S)
Stephen B. Pope

5d. PROJECT NUMBER

5e. TASK NUMBER

5f. WORK UNIT NUMBER

7. PERFORMING ORGANIZATION NAME(S) AND ADDRESS(ES)

Cornell University
Ithaca NY 14853

8. PERFORMING ORGANIZATION REPORT NUMBER

20030326 025

9. SPONSORING / MONITORING AGENCY NAME(S) AND ADDRESS(ES)
AFOSR/NA
4015 Wilson Boulevard Rm 713
Arlington, VA 22203-1954

11. SPONSOR/MONITOR'S REPORT NUMBER(S)

12. DISTRIBUTION / AVAILABILITY STATEMENT
Approved for public release; distribution is unlimited

13. SUPPLEMENTARY NOTES

14. ABSTRACT

Significant advances have been made in several aspects of the computational modelling of turbulent combustion. PDF model calculations have been performed of turbulent piloted-jet non-premixed flames. The results demonstrated the ability of the methodology to account, accurately, for the local extinction and reignition observed experimentally in these flames. It was shown that these flames can be sensitive to the temperature of the pilot and to radiative heat loss. A new approach has been developed for the efficient computational implementation of combustion chemistry. The rate-controlled constrained equilibrium method has been combined with the *in situ* adaptive tabulation algorithm to produce a unified dimension-reduction/storage-retrieval methodology for the computationally-efficient implementation of combustion chemistry. Test calculations demonstrated that this methodology has comparable accuracy to augmented reduced mechanisms. Ideas from the conditional moment closure and the mapping closure have been combined to produce a new approach for modeling molecular mixing in turbulent reactive flows. The new methodology has been shown to describe accurately (for the first time) the mixing of two scalars. A methodology has been developed for obtaining stochastic models for Lagrangian velocity and acceleration based on DNS data from homogeneous turbulent shear flow. It has been shown that the acceleration model provides a remarkably accurate representation of the observed Lagrangian velocity-acceleration two-time correlations. In collaboration with the group of Prof. P. Givi, advances have been made in the implementation of a combined LES/PDF methodology for modeling turbulent reactive flows. The approach based on the velocity filtered density function has been applied to a spatially-developing mixing layer and shown to account well for the major processes in this flow.

15. SUBJECT TERMS
Turbulent Combustion

16. SECURITY CLASSIFICATION OF:			17. LIMITATION OF ABSTRACT	18. NUMBER OF PAGES	19a. NAME OF RESPONSIBLE PERSON
a. REPORT	b. ABSTRACT	c. THIS PAGE	UL	63	Julian M. Tishkoff
unclassified	unclassified	unclassified			19b. TELEPHONE NUMBER (include area code) (703) 696-8478

PDF MODELLING OF TURBULENT COMBUSTION

AFOSR Grant F-49620-00-1-0171

Principal Investigator: Stephen B. Pope
Mechanical & Aerospace Engineering
Cornell University
Ithaca, NY 14853

FINAL TECHNICAL REPORT
2/15/2000-9/30/2002

ABSTRACT

Significant advances have been made in several aspects of the computational modelling of turbulent combustion. PDF model calculations have been performed of turbulent piloted-jet non-premixed flames. The results demonstrated the ability of the methodology to account, accurately, for the local extinction and reignition observed experimentally in these flames. It was shown that these flames can be sensitive to the temperature of the pilot and to radiative heat loss. A new approach has been developed for the efficient computational implementation of combustion chemistry. The rate-controlled constrained equilibrium method has been combined with the *in situ* adaptive tabulation algorithm to produce a unified dimension-reduction/storage-retrieval methodology for the computationally-efficient implementation of combustion chemistry. Test calculations demonstrated that this methodology has comparable accuracy to augmented reduced mechanisms. Ideas from the conditional moment closure and the mapping closure have been combined to produce a new approach for modeling molecular mixing in turbulent reactive flows. The new methodology has been shown to describe accurately (for the first time) the mixing of two scalars. A methodology has been developed for obtaining stochastic models for Lagrangian velocity and acceleration based on DNS data from homogeneous turbulent shear flow. It has been shown that the acceleration model provides a remarkably accurate representation of the observed Lagrangian velocity-acceleration two-time correlations. In collaboration with the group of Prof. P. Givi, advances have been made in the implementation of a combined LES/PDF methodology for modeling turbulent reactive flows. The approach based on the velocity filtered density function has been applied to a spatially-developing mixing layer and shown to account well for the major processes in this flow.

INTRODUCTION

The design process for gas-turbine combustors and aerospace propulsion systems could be significantly improved if accurate and affordable CFD tools were available. While turbulent combustion models are used in the design process, the models currently employed are not sufficiently accurate. PDF methods promise the capability of greater accuracy, through their ability to treat the chemistry in sufficient detail, and to fully account for turbulence-chemistry

interactions. The work performed in this research project has significantly contributed to the development and demonstration of different aspects of PDF methods.

The research has focused on the following topics.

1/ PDF calculations of turbulent non-premixed piloted jet flames.

2/ The development of a new methodology (based on rate-controlled constrained equilibrium and *in situ* adaptive tabulation) for the efficient implementation of combustion chemistry.

3/ The development of a new approach (related to the mapping closure and the conditional moment closure) for modeling mixing in turbulent reactive flows.

4/ The development of stochastic Lagrangian models for velocity and acceleration in turbulent flows, and a methodology to determine the model coefficients involved from DNS data.

5/ The implementation and demonstration of the approach based on the combination of large eddy simulation and PDF methods.

The work on each topic is described in the following sections, and more completely in the publications given below.

PDF CALCULATIONS OF PILOTED NONPREMIXED FLAMES

The piloted nonpremixed flames studied experimentally at Sandia (Barlow & Frank 1998) provide an excellent test of turbulent combustion models. These flames show distinct levels of interaction between turbulence and chemistry because of the increasing jet bulk velocities from flame *D* to *F*: flame *D* is close to equilibrium with a small amount of local extinction, whereas flame *F* is on the verge of global extinction. In each of these flames, the amount of local extinction reaches a peak at an axial distance of about 30 jet radii, with re-ignition occurring downstream. Several advanced approaches based on LES, CMC and PDF methods have been applied to compute these phenomena and have made significant progress. Notably, the joint PDF calculations of these flames by Xu and Pope (2000) and Lindstedt et al. (2000) show the best detailed agreement obtained between computations and the experimental data.

The PDF calculations of Xu & Pope (2000) and Tang et al. (2000) are capable of calculating, quantitatively, the observed phenomena of local extinction and reignition. These calculations are based on the modelled transport equation for the joint PDF of velocity, turbulence frequency, and composition. The sub-models of this method include the simplified Langevin model (SLM) for velocity and the Jayesh-Pope model (JPM) for turbulent frequency (see Pope 2000). The molecular mixing is modeled by the Euclidean minimal spanning tree (EMST) model of Subramaniam & Pope (1998), which features mixing locally in the composition space through interacting particles with neighboring particles. The reaction mechanism used is the 19 species, 15-step augmented reduced mechanism of Sung et al. (1998) which includes *NO* chemistry, and is denoted by ARM2. The chemical reaction calculations are performed using the *in situ* adaptive tabulation (ISAT) algorithm (Pope 1997). It should be pointed out that for each full-scale PDF

method calculation, the solution to the reaction equation system (20 dimensional) is required (of order) 10^9 times. ISAT can handle these computations economically and accurately. Recent work on PDF methods for these flames–now described–concerns sensitivity to the pilot flame temperature and to radiative heat loss.

It was observed by Xu & Pope (2000) that calculations of flame *F* exhibit some sensitivity to the pilot temperature T_p which is specified as a boundary condition. The experimental data show T_p in the range 1860K-1880K, but the experimental accuracy may be no greater than 10-20K. This influence was studied systematically by performing calculations of flames *D* and *F* with pilot temperatures of T_p = 1860, 1870 and 1880K. For flame *D* it is found that the calculations are insensitive to T_p. But, as shown on Fig. 1, flame *F* exhibits extreme sensitivity. For example, at $x/R_j = 15$ and 30 the peak temperature decreases by about 500K and the mass fractions of *OH* decrease by a factor of more than two with a 10K decrease in pilot temperature. Similar trends exist for other variables. Particularly for *NO*, the results calculated using lower pilot temperatures give a perfect match with the experimental data at the first two locations shown in the figure. However, further downstream, all the modeled *NO* profiles overshot the peak value by a factor of more than two and do not predict correctly on the fuel rich side, although the temperature profiles seem to be satisfactory.

Figure 2 shows another manifestation of the sensitivity to the pilot temperature. The burning index (BI) is defined to be unity for complete combustion and zero for complete extinction. The figure shows substantially different results for T_p = 1860K and T_p = 1880K, with the experimental data generally falling between these two calculated values.

The effects of radiative heat loss were investigated by performing "adiabatic" and "radiant" calculations. In the former all heat loss is neglected: in the latter, radiative heat loss is accounted for from the primary radiating species, CO_2, H_2O, *CO* and CH_4. We adopt an optically-thin limit radiation model, although the validity of this model for the 4.3-micron band of CO_2 is still in debate. Implemented in the framework of ISAT, the model includes the above four gas-phase emitting species with their Plank mean absorption coefficients calculated by RADCAL.

For flame *D* (not shown) the effect of radiation is to reduce the peak temperature by about 30K and to decrease the peak *NO* by 15%. Figure 3 presents the conditional mean profiles of four scalars, and shows completely different picture from the flame *D* results. For T_p = 1880K, the inclusion of radiation induces significant decreases in temperature and species mass fractions at the first three axial locations. The largest differences appear at x/R_j = 30 where the peak temperature decreases more than 500K and the species mass fractions decrease by a factor of two or three. This fact indicates that thermal radiation can significantly alter the local extinction status in this flame: not only is the *NO* chemistry strongly influenced by radiation, but also the reactions of other species such as *OH* and *CO*. The last column of Fig. 3 tells us that further downstream, the flame becomes closer to the equilibrium state as re-ignition takes place and the radiation tends to be less important.

Evidently, flame *F* is extremely sensitive to a decrease in temperature, whether it arises from T_p or from radiation.

EFFICIENT IMPLEMENTATION OF COMBUSTION CHEMISTRY

It is computationally prohibitive to use detailed hydrocarbon chemistry directly in turbulent combustion calculation. Two separate approaches have been taken to reduce the computational burden: dimension reduction, and storage/retrieval. Tang & Pope (2002) have combined these two approaches into a unified methodology. Dimension reduction is achieved through rate-controlled constrained equilibrium ((RCCE Keck, 1990); and storage/retrieval through the ISAT algorithm Pope (1997)). In this context, RCCE is preferred over other reduction methodologies (e.g., QSSA, ILDM), because of the guaranteed existence and continuity of the implied low-dimensional manifold.

The combined ISAT-RCCE methodology is tested for a pairwise-mixing stirred reactor (PMSR) using the 31-species GRI 1.2 mechanism for methane. Three different tests (referred to as C_1, C_2 and C_3) are performed. In C_1 the constrained species are H_2O, CO_2, O_2, CH_4 and CO. Three more species (H_2, OH, and O) are added to form the constraint subspace in C_2, and in C_3 another three species (CH_3, C_2H_2 and C_2H_4) are included. Additional constraints are imposed on all 4 elements and enthalpy, and hence the dimension reductions are from 32 to 10, 13 and 16 for the three cases, respectively. To test the accuracy of the algorithm, we solve the entire ODE system (32-dimensional) by direct integration (DI) to get the accurate solution. Figure 4 shows the relative error in species compositions, temperature and density against their reference values for one particle (advanced over 2000 time steps in the statistically stationary state). It can be observed that, as the number of constraints increases, the error in the constrained species decreases. For C_3, the relative errors in major species (including CO and H_2) are under 3% with the errors of other constrained species being less than 10%.

In Figure 5, the accuracy of ISAT-RCCE is compared to that of the augmented reduced mechanism of Sung et al. (1998)–which is based on the same detailed mechanism and which has the same number of degrees of freedom. It may be seen that the two methods have comparable accuracy.

MODELLING TURBULENT MIXING

In PDF methods for turbulent combustion, the modeling of molecular diffusion is both crucial and difficult. In Klimenko & Pope (2002) a new methodology is developed-multiple mapping conditioning (MMC)–which combines ideas from the mapping closure (Chen et al. 1989), and from the conditional moment closure (Klimenko & Bilger 1999). In part, this approach extends the particle implementation of the mapping closure to multiple scalars.

Remarkably, the MMC model admits an analytic solution for the case of two passive scalars evolving from a triple-delta-function initial condition. This case was studied using DNS by Juneja & Pope (1996), with the three delta functions located at the vertices of an equilateral triangle in the two-dimensional composition space. The evolution predicted by MMC (Fig. 6) is in excellent agreement with the DNS. No other mixing model has been shown to be even qualitatively correct for this case.

STOCHASTIC MODELLING OF VELOCITY AND ACCELERATION

In PDF methods, the turbulence modeling is embodied in a stochastic model for the velocity following a fluid particle (see e.g., Pope 2000). The standard model-the generalized Langevin model–involves tensor coefficients. In Pope (2002a) a methodology is developed to determine these coefficients from DNS data. In Pope (2002b) this methodology is extended to a stochastic model for acceleration, which is a natural way to incorporate Reynolds-number effects.

Figure 7 shows the velocity-acceleration autocovariances predicted by the model compared to the DNS data of Sawford & Yeung (2000). As may be seen, the model is able to provide an accurate representation of these fundamental statistics.

LARGE EDDY SIMULATION

The PDF calculations reported above (e.g., Xu & Pope 2000) are based on a completely statistical approach. For some turbulent reacting flow, especially those with large-scale unsteady motions, there is good reason to use large eddy simulation (LES). In this approach, the large scales are treated deterministically, and the small scales statistically. It is important to appreciate that for turbulent combustion, the subgrid scale modeling pertaining to reaction required in LES is similar to, and just as crucial as, the modeling of turbulence-combustion interactions in statistical approaches. It is natural, therefore, to combine the ability of LES to represent large-scale unsteady motions, with the benefits of PDF methods for modeling the turbulent-chemistry interactions. The PI has a long-term collaboration with the group of Prof. Peyman Givi to develop this combined LES/PDF methodology.

Following the earlier work of Colucci et al. (1998) and Jaberi et al. (1999), recently Gicquel et al. (2002) have extended the methodology to consider the velocity filtered density function (VFDF). In this methodology, the effects of the unresolved subgrid scales (SGS) are taken into account by considering the joint probability density function of all of the components of the velocity vector. An exact transport equation is derived for the VFDF in which the effects of the SGS convection appear in closed form. The unclosed terms in this transport equation are modeled. A system of stochastic differential equations (SDEs) which yields statistically equivalent results to the modeled VFDF transport equation is constructed. These SDEs are solved numerically by a Lagrangian Monte Carlo procedure in which the Ito character of the SDEs is preserved. The consistency of the proposed SDEs and the convergence of the Monte Carlo solution are assessed by comparison with results obtained by an Eulerian LES procedure in which the corresponding transport equations for the first two SGS moments are solved. The VFDF results are compared with those obtained via several existing SGS closures. These results are also analyzed via *a priori* and *a posteriori* comparisons with results obtained by direct numerical simulation of an incompressible, three–dimensional, temporally developing mixing layer.

REFERENCES

R. S. Barlow and J.H. Frank (1998). *Proc. Combust. Inst.* Vol. 27, pp. 1087-1095.

H. Chen, S. Chen & R.H. Kraichnan (1989). *Phys. Rev. Lett.* 63:2657.

P.J. Colucci, F.A. Jaberi, P. Givi and S.B. Pope (1998). *Phys. Fluids* **10**, 499-515.

L.Y.M. Gicquel, P. Givi, F.A. Jaberi & S.B. Pope (2002). *Phys. Fluids* 14:1196.

F.A. Jaberi, P.J. Colucci, S. James, P. Givi and S.B. Pope (1999). *J. Fluid Mech.* 401, 85-121.

A. Juneja and S.B. Pope (1996). *Phys. Fluids* 8:2161.

J.C. Keck (1990). *Prog. Energy Combust. Sci.* 16:125.

A. Klimenko and R.W. Bilger (1999). *Prog. Energy Combust. Sci.* 25:595.

A. Klimenko and S. B. Pope (2002). "A model for turbulent reactive flow based on multiple mapping conditioning." *Phys. Fluid* (submitted).

R.P. Lindstedt, S.A. Louloudi, and E.M. Váos (2000). *Proc. Combust. Inst.*, **28**, 149-156.

S.B.Pope (1997). *Combust. Theor. Modelling*, 1:41-63.

S.B. Pope (2000). *Turbulent Flows*, Cambridge University Press.

S.B. Pope (2000). *Phys. Fluids* **14**:1696-1702.

S.B. Pope (2002b). *Phys. Fluids* **14**:2360-2375.

B.L. Sawford and P.K. Yeung (2000). *Phys. Fluids* 12:2033.

S. Subramaniam and S.B. Pope (1998). *Combust. Flame*, 115:487-514.

C.J. Sung, C.K. Law and J.-Y. Chen (1998). *Proc. Combust. Inst.*, Vol. 27, pp. 295-304.

Q. Tang, J. Xu and S.B. Pope (2000). *Proc. Combust. Inst.*, Vol. 28, pp. 133-139.

Q. Tang and S.B. Pope (2002). *Proc. Combust. Inst.* **29** (to be published).

J. Xu and S.B. Pope (2000). *Combust. Flame,* 123:281-307.

FIGURES

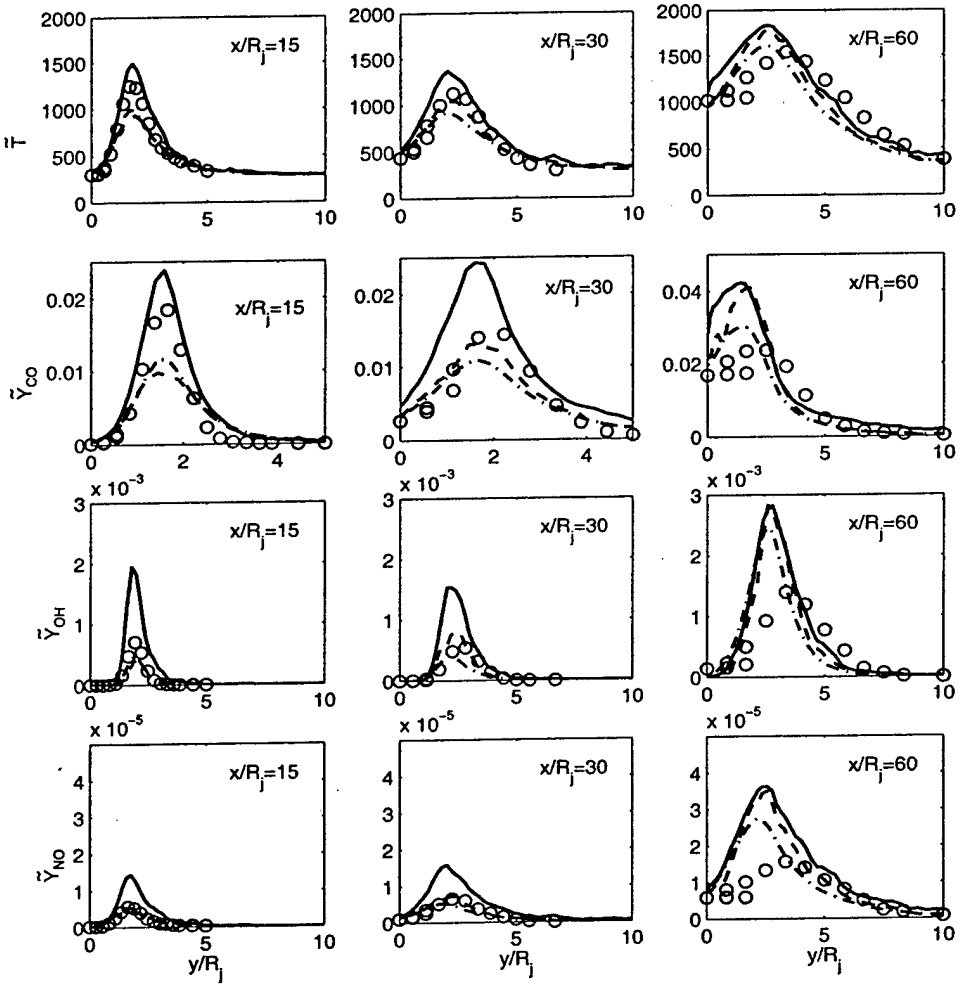

Fig. 1. Radial profiles of mean temperature and mass fractions in flame F: sensitivity to pilot temperature, T_p. Symbols, experimental data; solid line T_p = 1880K; dashed line T_p = 1870K; dot-dashed line T_p = 1860K.

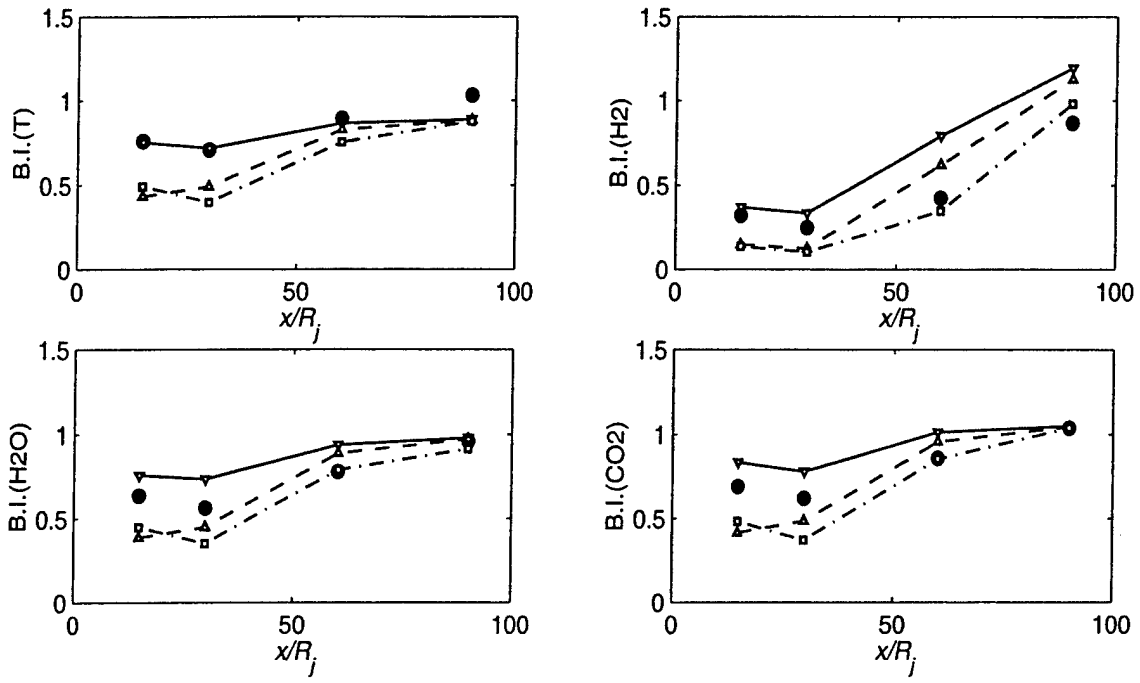

Fig. 2. Burning index (based on T and species) vs. axial distance in flame F. Symbols and lines as in Fig. 1.

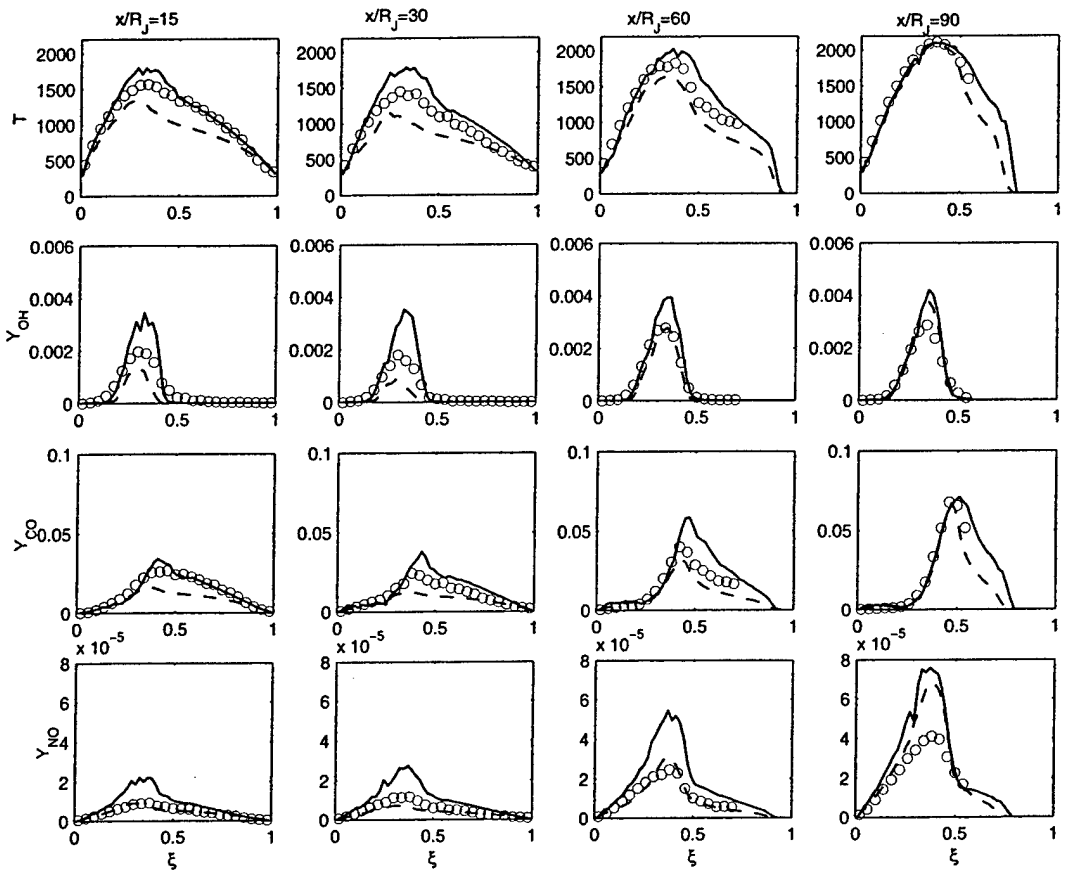

Fig. 3. Effect of radiative heat loss on means conditional on mixture fraction in flame *F*. Symbols, experimental data; solid line, adiabatic calculation; dashed line, radiant calculation.

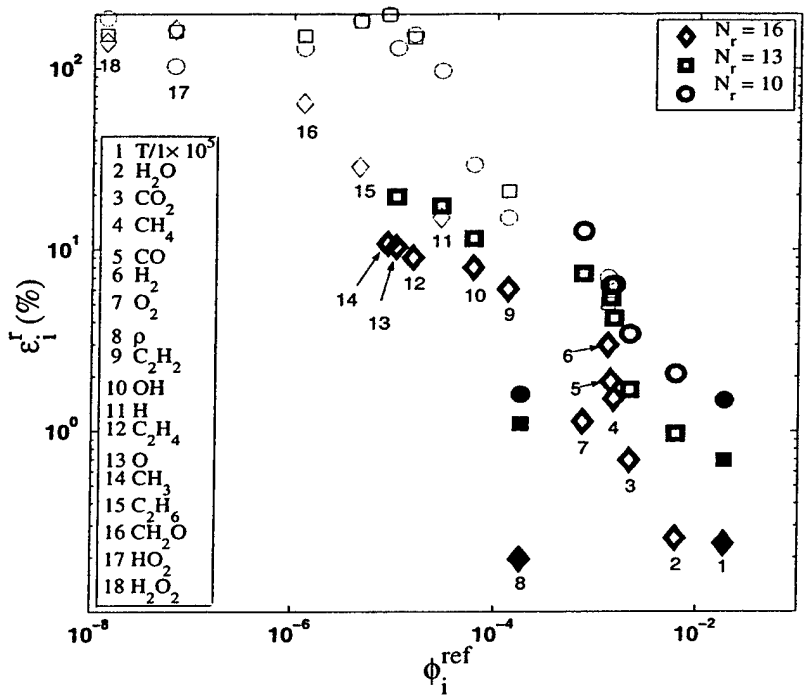

Fig.4: Relative errors for different species, temperature and density, against the reference value for each quantity, for different numbers of represented species in ISAT-RCCE. From the PMSR test case of Tang & Pope (2002).

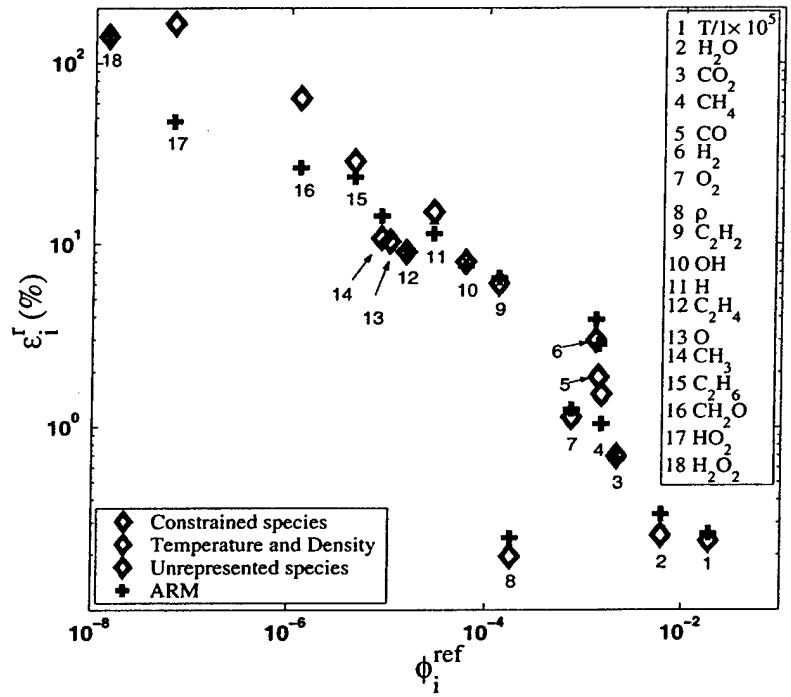

Fig. 5: Relative errors for different species, temperature and density, against the reference value for each quantity, from the PMSR test case: comparison of ISAT-RCCE (Tang & Pope 2002) with the augmented reduced mechanism (Sung et al. 1998).

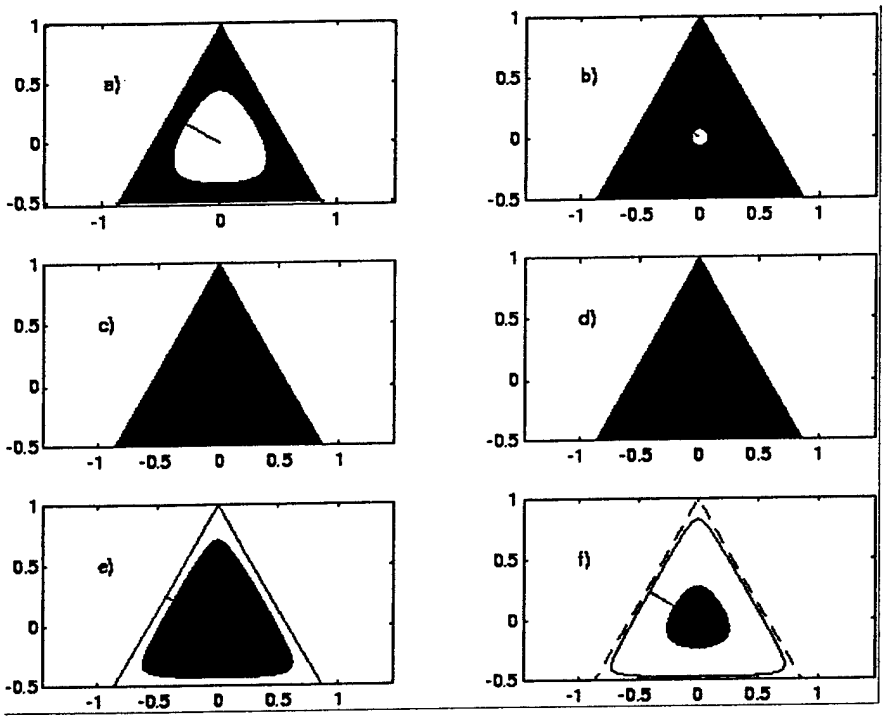

Fig. 6: Temporal evolution (a-f) of the joint PDF of two passive scalars from a triple-delta-function initial condition according to the MMC closure of Klimenko & Pope (2002).

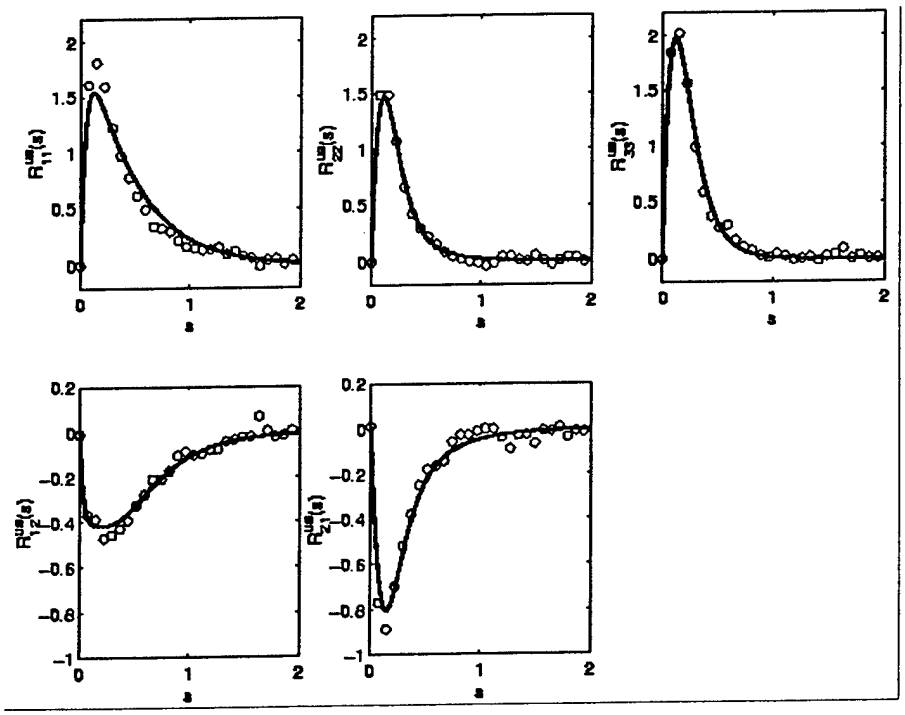

Fig. 7: Velocity-acceleration Lagrangian covariances: symbols, from the DNS data of Sawford & Yeung (2001); lines, from the stochastic model of Pope (2002b).

PERSONNEL SUPPORTED

Prof. S.B. Pope, PI
Prof. A. Klimenko, sabbatical visitor
S. Joseph, graduate student
Q. Tang, graduate student
M. Singer, graduate student
R. Cao, graduate student

DEGREES GRANTED

S. Joseph, M.S.
Q. Tang, Ph.D. (May 2003)

PUBLICATIONS

The following papers were written and/or published during the reporting period.

L.Y.M. Gicquel, P. Givi, F.A. Jaberi and S.B. Pope (2002). "Velocity filtered density function for large eddy simulation of turbulent flows," *Phys. Fluids* **14**, 1196-1213.

P. Jenny, S.B. Pope, M. Muradoglu and D.A. Caughey (2001). "A hybrid algorithm for the joint PDF equation for turbulent reactive flows," *J. Comp. Phys.* **166**, 281-252.

A.Y. Klimenko and S.B. Pope (2002). "A model for turbulent reactive flows based on multiple mapping conditioning," *Physics of Fluids* (submitted).

S.B. Pope (2001). "Large-eddy simulation using projection onto local basis functions," in: Fluid Mechanics and the Environment: Dynamical Approaches, Ed. J.L. Lumley, Springer.

S.B. Pope (2002). "Stochastic Lagrangian Models of Velocity in Homogeneous Turbulent Shear Flow," *Phys. Fluids* **14**, 1696-1702.

S.B. Pope (2002). "A stochastic Lagrangian model for acceleration in turbulent flows," *Physics of Fluids* **14**, 2360-2375.

Q. Tang, J. Xu and S.B. Pope (2000). "PDF calculations of local extinction and *NO* production in piloted-jet turbulent methane/air flames," Proceedings of the Combustion Institute, **28**, 133-139.

Q. Tang and S.B. Pope (2002). "Implementation of combustion chemistry by *in situ* adaptive tabulation of rate-controlled constrained equilibrium manifolds," *Proc. Comb. Inst.* **29** (to be published).

J. Xu and S.B. Pope (2000). "PDF calculations of turbulent nonpremixed flames with local extinction," *Combust. Flame* **123**, 281-307.

PRESENTATIONS

June 5, 2000: University of California, Santa Barbara, Institute of Theoretical Physics.

June 13, 2000: AFOSR/ARO Contractors' Meeting, Workshop Presentation, Santa Fe, NM.

July 27, 2000: Fifth International Workshop on Nonpremixed Turbulent Combustion, Delft, Netherlands.

August 1, 2000: International Symposium on Combustion, Edinburgh, two presentations plus posters.

November 20, 2000: APS/DFD Annual meeting, 3 contributed talks.

December 8, 2000: Princeton University, invited seminar.

March 26, 2001: Combustion Institute Joint Meeting, Oakland California.

June 3, 2001: IUTAM Symposium on Mixing and Combustion, Kingston, Ontario.

June 18, 2001: AFOSR/ARO Contractors' meeting, USC.

June 24, 2001: The Lumley Symposium, Cornell University.

June 28, 2001: Second Symposium on Turbulent Shear Flows Phenomena, Stockholm, Sweden; invited plenary talk.

October 18, 2001: Penn. State; colloquium.

October 19, 2001: Penn. State; invited lecture.

November 2, 2001: Delft, Netherlands; Micromixing workshop, invited lecture.

November 19, 2001: San Diego, CA; APS/DFD, 3 contributed talks.

February 5, 2002: NASA Langley; Langley Colloquium.

February 5, 2002: Hampton Air & Space Museum; Sigma Lecture, (invited public lecture).

February 20, 2002: UCLA, CA; colloquium.

February 22, 2002: Caltech, CA; colloquium.

April 8, 2002: Numerical Combustion Conference, Sorrento, Italy; 2 contributed talks.

June 29, 2002: Warrenton, VA; DOE Contractors meeting.

July 17-20, 2002: Sapporo, Japan; Seventh International Workshop on Measurement and Calculation of Turbulent Non-Premixed Flames (TNF6), invited talk.

July 21-26, 2002; Sapporo, Japan; 29th International Combustion Symposium, contributed paper.

November 23-26, 2002 APS/DFD Annual Meeting, 2 contributed talks.

TECHNOLOGY TRANSFERS AND TRANSFERS

Performer	Customer	Result	Application
Dr. S.B. Pope Cornell Univ. 607 255 4314	Dr. G.M. Goldin Fluent, Inc. Lebanon, NH 603 643 2600	Models and numerical algorithms for PDF methods	Fluent CFD code
Dr. S.B. Pope Cornell Univ. 607 255 4314	Dr. G.M. Goldin Fluent, Inc. Lebanon, NH 603 643 2600	Algorithm for efficient implementation of combustion chemistry	Fluent CFD code
Dr. S.B. Pope Cornell Univ. 607 255 4314	Dr. M.S. Anand Rolls Royce, Inc. Indianapolis, IN 317 230 2828	Algorithms for PDF methods or unstructured grids	Gas Turbine combustor computations
Dr. S.B. Pope Cornell Univ. 607 255-4314	Dr. Paul Van Slooten United Technologies Corporation East Hartford, CT 860 610 7397	PDF algorithms for gas-turbine combustor modelling	Gas Turbine combustor computations
Dr. S.B. Pope Cornell Univ. 607 255-4314	Dr. Paul Van Slooten United Technologies Corporation East Hartford, CT 860 610 7397	Chemistry interface routines for CFD codes	Gas Turbine combustor computations

Dr. S.B. Pope Cornell Univ. 607 255-4314	Dr. M.S. Anand Rolls Royce Corp Indianapolis IN 317 230-2828	Variable time-step algorithm for PDF methods for gas-turbine combustor modelling	Gas Turbine combustor computations

INTERACTIONS

June 14, 2002; Dayton

Discussion (organized by Dr. T. Jackson) with Dr. R.A. Baurle (Taitech Inc. AFRL) on combustion modeling in LES calculations of scramjets.

June 14, 2002; Dayton

Discussion (organized by M. Roquemore) with Dr. B. Sekar (AFRL) on turbulent combustion modeling activities at AFRL.

OTHER INTERACTIONS

During the reporting period the PI has visited:
Rolls Royce Corporation, Indianapolis, IN
Rocketdyne, Canoga Park, CA
Los Alamos National Lab, NM
United Technologies, Hartford, CT
NASA Langley, Hampton, VA
Air Force Research Laboratoies, Dayton OH
Fluent Inc., Lebanon, NH

Principal Investigator Annual Data Collection (PIADC) Survey Form

NOTE: If there is insufficient space on this survey to meet your data submissions, please submit additional data in the same format as identified below.

PI DATA

Name (Last, First, MI): Pope, Stephen B.

Institution: Cornell University

Contract/Grant No.: F-49620-00-1-0171

AFOSR USE ONLY
Project/Subarea
_____/____

NX _____

FY _____

NUMBER OF CONTRACT/GRANT CO-INVESTIGATORS

Faculty 1 Post Doctorates 0 Graduate Students 4 Other 0

PUBLICATIONS RELATED TO AFOREMENTIONED CONTRACT/GRANT

NOTE: List names in the following format: Last Name, First Name, MI

Include: Articles in peer reviewed publications, journals, book chapters, and editorships of books.

Do Not Include: Unreviewed proceedings and reports, abstracts, "Scientific American" type articles, or articles that are not primary reports of new data, and articles submitted or accepted for publication, but with a publication date outside the stated time frame.

Name of Journal, Book, etc.: See attached

Title of Article: _____

Author(s): _____

Publisher (if applicable): _____

Volume: _____ Page(s): _____ Month Published: _____ Year Published: _____

Name of Journal, Book, etc.: _____

Title of Article: _____

Author(s): _____

Publisher (if applicable): _____

Volume: _____ Page(s): _____ Month Published: _____ Year Published: _____

HONORS/AWARDS RECEIVED DURING CONTRACT/GRANT LIFETIME

Include: All honors and awards received during the lifetime of the contract or grant, and any life achievement honors such as (Nobel prize, honorary doctorates, and society fellowships) prior to this contract or grant.

Do Not Include: Honors and awards unrelated to the scientific field covered by the contract/grant.

Honor/Award: _____ Year Received: _____

Honor/Award Recipient(s): _____

Awarding Organization: _____

S. B. Pope	Fellow, American Physical Society	1991
S. B. Pope	Associate Fellow, AIAA	1984
S. B. Pope	Overseas Fellow, Churchill College, Cambridge	1989
S. B. Pope	Excellence in Teaching Award, Cornell University	2002

Physics of Fluids
Velocity filtered density function for large eddy simulation of turbulent flows
L.Y.M. Gicquel, P. Givi, F.A. Jaberi and S.B. Pope
AIP
Vol. 14 Pages 1196-1213 Year: 2002

J. Comp. Phys.
A hybrid algorithm for the joint PDF equation for turbulent reactive flows
P. Jenny, S.B. Pope, M. Muradoglu and D.A. Caughey
Elsevier
Vol. 166 Pages 281-252 Year: 2001

Physics of Fluids
A model for turbulent reactive flows based on multiple mapping conditioning
A.Y. Klimenko and S.B. Pope
AIP
Submitted, Year: 2002

Dynamical Approaches, Ed. J.L. Lumley
Large-eddy simulation using projection onto local basis functions in:
Fluid Mechanics and the Environment
S.B. Pope
Springer
Year: 2001

Physics of Fluids
Stochastic Lagrangian Models of Velocity in Homogeneous Turbulent Shear Flow
S.B. Pope
AIP
Vol.14 Pages 1696-1702 Year: 2002

Physics of Fluids
A stochastic Lagrangian model for acceleration in turbulent flows
S.B. Pope
AIP
Vol. 14 Pages 2360-2375 Year: 2002

Proceedings of the Combustion Institute
PDF calculations of local extinction and *NO* production in piloted-jet turbulent methane/air flames
Q. Tang, J. Xu and S.B. Pope
Vol. 28 Pages 133-139 Year: 2000

Proc. Comb. Inst.
Implementation of combustion chemistry by *in situ* adaptive tabulation of rate-controlled constrained equilibrium manifolds
Q. Tang and S.B. Pope
To be published
Vol. 29 Year: 2002

Combust. Flame
PDF calculations of turbulent nonpremixed flames with local extinction
J. Xu and S.B. Pope
Elsevier
Vol. 123 Pages 281-307 Year: 2000

Stochastic Lagrangian models of velocity in homogeneous turbulent shear flow

Stephen B. Pope
Department of Mechanical & Aerospace Engineering, Cornell University, Ithaca, New York 14853

(Received 5 November 2001; accepted 31 January 2002; published 1 April 2002)

Stochastic Lagrangian models for the velocity following a fluid particle are used both in studies of turbulent dispersion and in probability density function (PDF) modeling of turbulent flows. A general linear model is examined for the important case of homogeneous turbulent shear flow, for which there are recent direct numerical simulation (DNS) data on Lagrangian statistics. The model is defined by a drift coefficient tensor and a diffusion tensor, and it is shown that these are uniquely determined by the normalized Reynolds-stress and timescale tensors determined from DNS. With the coefficients thus determined, the model yields autocorrelation functions in good agreement with the DNS data. It is found that the diffusion tensor is significantly anisotropic—contrary to the Kolmogorov hypotheses and conventional modeling—which may be a low-Reynolds-number effect. The performance of two PDF models is also compared to the DNS data. These are the simplified Lagrangian model and the Lagrangian isotropization of production model. There are significant differences between the autocorrelation functions generated by these models and the DNS data.
 [DOI: 10.1063/1.1465421]

I. INTRODUCTION

Homogeneous turbulent shear flow is of fundamental importance in the development of models for inhomogeneous turbulent flows. Both experiments[1] and direct numerical simulations (DNS)[2] of homogeneous shear flow have been performed in which Eulerian statistics of the turbulence have been measured. More recently, a series of DNS studies has been performed[3–5] in which Lagrangian statistics have been obtained by tracking a large number of fluid particles. These studies clearly have direct relevance to stochastic Lagrangian models[6] of turbulence, which model the motion of fluid particles as diffusion processes (i.e., continuous Markov processes).[7] The purpose of this paper is to show the connection between the Lagrangian velocity autocovariance tensor obtained from DNS and stochastic Lagrangian models for fluid particle velocity.

Stochastic Lagrangian models for the velocity of a fluid particle arise in two different contexts: turbulent dispersion;[8–10] and probability density function (PDF) models.[11,12,7] In both cases the general form of the models considered (when applied to homogeneous turbulence) can be written as the linear stochastic differential equation (SDE)

$$du_i = -A_{ij}u_j\,dt + B_{ij}dW_j, \tag{1}$$

where $d\mathbf{u}(t) \equiv \mathbf{u}(t+dt) - \mathbf{u}(t)$ is the infinitesimal increment of the fluctuating component of velocity $\mathbf{u}(t)$ following the fluid particle; we refer to $\mathbf{A}(t)$ as the drift tensor; $\mathbf{B}(t)$ is the diffusion coefficient; and $d\mathbf{W}(t)$ is the infinitesimal increment of a vector-valued Wiener process which has the properties $\langle d\mathbf{W}\rangle = 0$, $\langle dW_i\,dW_j\rangle = dt\,\delta_{ij}$. Different models correspond to different specifications of the drift tensor $\mathbf{A}(t)$ and diffusion coefficient $\mathbf{B}(t)$.

For statistically stationary, homogeneous isotropic turbulence (with no mean velocity gradients) the only sensible choice of coefficients is

$$A_{ij} = \frac{\delta_{ij}}{T_L}, \tag{2}$$

and

$$B_{ij} = \left(\frac{2u'^2}{T_L}\right)^{1/2}\delta_{ij}, \tag{3}$$

where T_L is the Lagrangian integral timescale and u' is the turbulence intensity (i.e., the rms velocity fluctuation). Then, Eq. (1) reduces to an independent Langevin equation for each component of velocity

$$du_i = -u_i\frac{dt}{T_L} + \left(\frac{2u'^2}{T_L}\right)^{1/2} dW_i. \tag{4}$$

This model dates back to Taylor's 1921 original paper on turbulent dispersion.[8] The autocorrelation function given by Eq. (4) is

$$\rho(s) \equiv \langle u_1(t)u_1(t+s)\rangle/u'^2 = \exp(-|s|/T_L), \tag{5}$$

which agrees well with DNS data[13] (except at small values of $|s|/T_L$).

The central issue addressed here is the appropriate specification of $\mathbf{A}$ and $\mathbf{B}$ in homogeneous turbulent shear flow. This has been considered in the context of turbulent dispersion by Sawford and Yeung.[4,5] These authors compared Lagrangian autocorrelations predicted by two dispersion models to DNS data. Both of these models take $\mathbf{B}$ to be isotropic.

We show here that appropriate values of $\mathbf{A}$ and $\mathbf{B}$ can be deduced from the measured Lagrangian velocity autocovariance, and that the resulting model is in good agreement with

the DNS data. This agreement supports the nontrivial conclusion that the Lagrangian velocity is well represented by a linear diffusion process (except over small time intervals). The deduced value of **B** is significantly anisotropic.

The performance of two models used in PDF methods is compared to the DNS data. These are the simplified Langevin model (SLM) and the Lagrangian isotropization of production (LIPM) model.[14]

II. HOMOGENEOUS TURBULENT SHEAR FLOW

In homogeneous turbulent shear flow, the imposed mean velocity gradient is

$$\frac{\partial\langle U_i\rangle}{\partial x_j}=\mathcal{S}\delta_{i1}\delta_{j2}, \tag{6}$$

where $\mathcal{S}$ is the (constant) imposed mean shear rate. The turbulence is characterized by the Reynolds stress tensor $\langle u_iu_j\rangle$, the turbulent kinetic energy $k\equiv\frac{1}{2}\langle u_iu_i\rangle$, and the mean dissipation rate ε. All of these quantities are uniform in space and evolve in time.

An essential observation from experiments and DNS is that, after an initial transient, the turbulence tends to an approximately self-similar state. The normalized Reynolds-stress tensor

$$C_{ij}\equiv\frac{\langle u_iu_j\rangle}{k} \tag{7}$$

becomes constant, as does the ratio of turbulence-to-shear timescales, $\mathcal{S}k/\varepsilon$, and hence also the ratio of production $\mathcal{P}$ to dissipation ε. The turbulent kinetic energy equation then dictates that k and ε increase exponentially with time—as is observed. Thus when normalized by k and ε, quantities pertaining to the energy-containing scales of the turbulence are self-similar. Since the Reynolds number $k^2/(\varepsilon\nu)$ increases with time, small-scale quantities are not self-similar under this scaling.

The DNS of Sawford and Yeung[4,5] are performed from the nondimensional time $\mathcal{S}t=0$ until $\mathcal{S}t=20$. The fluid particles are introduced at $\mathcal{S}t=4$ when the self-similar state has been attained. The values $\mathcal{S}k/\varepsilon=4.83$ and $\mathcal{P}/\varepsilon=1.54$ are deduced from the values of k and $\langle u_1u_2\rangle$ from $\mathcal{S}t=4$ until $\mathcal{S}t=20$; and the average value of the normalized Reynolds stress tensor over this time interval is

$$\mathbf{C}=\begin{bmatrix}0.96 & -0.32 & 0\\ -0.32 & 0.43 & 0\\ 0 & 0 & 0.61\end{bmatrix}. \tag{8}$$

We introduce the normalized time

$$\hat{t}\equiv t\frac{\varepsilon}{k}, \tag{9}$$

and the scaled fluctuating velocity following a fluid particle

$$\hat{\mathbf{u}}(\hat{t})\equiv\frac{\mathbf{u}(t)}{k(t)^{1/2}}. \tag{10}$$

Consistent with the self-similar state of the turbulence, we assume that $\hat{\mathbf{u}}(\hat{t})$ is a statistically stationary process.

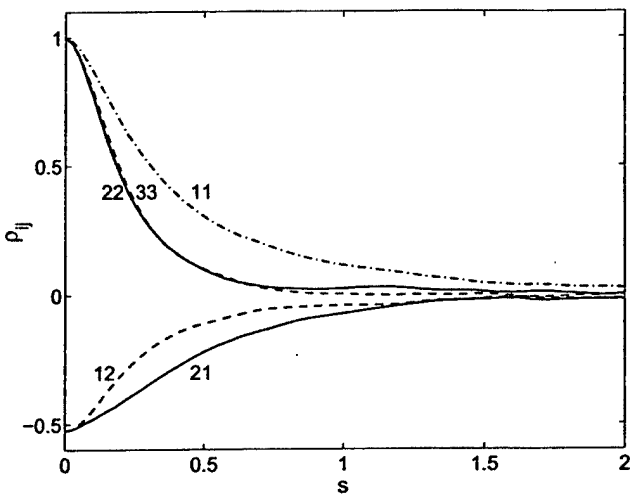

FIG. 1. Autocorrelation functions $\rho_{ij}(s)$, Eq. (14), from the DNS data of Sawford and Yeung (Ref. 5).

The autocovariance of $\hat{\mathbf{u}}(\hat{t})$ is

$$\hat{R}_{ij}(s)\equiv\langle\hat{u}_i(\hat{t})\hat{u}_j(\hat{t}+s)\rangle, \tag{11}$$

which (in view of the assumed stationarity) is independent of $\hat{t}$; and the scaled Reynolds stress is

$$\langle\hat{u}_i(t)\hat{u}_j(t)\rangle=C_{ij}=\hat{R}_{ij}(0)=\frac{\langle u_iu_j\rangle}{k}, \tag{12}$$

which is constant. Note that (unlike C_{ij}) $\hat{R}_{ij}(s)$ is not symmetric, although it has the property

$$\hat{R}_{ij}(s)=\hat{R}_{ji}(-s). \tag{13}$$

It is conventional to define autocorrelation functions by

$$\rho_{ij}(s)\equiv\frac{\hat{R}_{ij}(s)}{[C_{(i)(i)}C_{(j)(j)}]^{1/2}} \tag{14}$$

(where bracketed suffixes are excluded from the summation convention) so that the diagonal components of $\rho_{ij}(0)$ are unity. These autocorrelation functions obtained from the DNS are shown in Fig. 1. (Note that, by symmetry, $\rho_{23}=\rho_{32}=0$.)

The analysis below shows that a preferable definition of the autocorrelations is

$$R_{ij}(s)\equiv C_{ik}^{-1}\hat{R}_{kj}(s), \tag{15}$$

where C_{ik}^{-1} denotes the i-k component of the inverse of **C**. Unlike ρ_{ij}, R_{ij} is a tensor, and at the origin it is

$$R_{ij}(0)=\delta_{ij}. \tag{16}$$

These autocorrelation functions obtained from the DNS are shown in Fig. 2. [There is a small inconsistency in the extraction of numerical values from the DNS: C_{ij} is obtained as an average from $\mathcal{S}t=4$ to $\mathcal{S}t=20$, whereas $\hat{R}_{ij}(0)$ is obtained at $\mathcal{S}t=4$. As a consequence, as may be seen in Fig. 2, the numerical values do not satisfy Eq. (16) exactly.]

Based on $R_{ij}(s)$, we define the (normalized) integral timescales by

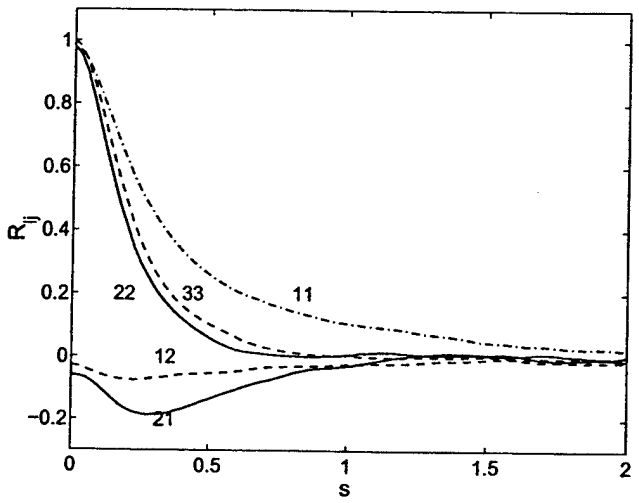

FIG. 2. Autocorrelation functions $R_{ij}(s)$, Eq. (15), from the DNS data of Sawford and Yeung (Ref. 5).

$$T_{ij} \equiv \int_0^\infty R_{ij}(s)\,ds. \tag{17}$$

The values deduced from the DNS data are

$$\mathbf{T} = \begin{bmatrix} 0.44 & -0.06 & 0 \\ -0.11 & 0.22 & 0 \\ 0 & 0 & 0.24 \end{bmatrix}. \tag{18}$$

III. STOCHASTIC MODEL

The stochastic model considered is Eq. (1) written for $\hat{\mathbf{u}}(\hat{t})$. It is convenient to use matrix notation, and so the equation is written

$$d\hat{\mathbf{u}} = -\mathbf{A}\hat{\mathbf{u}}\,d\hat{t} + \mathbf{B}\,d\hat{\mathbf{W}}, \tag{19}$$

where $\langle d\hat{\mathbf{W}}\,d\hat{\mathbf{W}}^T\rangle = \mathbf{I}\,dt$, with $\mathbf{I}$ being the identity, and T denoting the transpose.

The drift matrix $\mathbf{A}$ is constant and it is required that its eigenvalues have positive real parts. The value of $\mathbf{A}$ deduced from the DNS (below) has the simplest structure—real positive eigenvalues and independent eigenvectors. In this case $\mathbf{A}$ can be decomposed as

$$\mathbf{A} = \mathbf{V}\mathbf{\Lambda}\mathbf{V}^{-1}, \tag{20}$$

where the columns of $\mathbf{V}$ are the eigenvectors of $\mathbf{A}$, and $\mathbf{\Lambda}$ is the diagonal matrix of eigenvalues.

The diffusion coefficient matrix $\mathbf{B}$ is also constant and, without loss of generality,[7] we take it to be symmetric ($\mathbf{B} = \mathbf{B}^T$).

A. Autocorrelation function

It is readily deduced from Eq. (19) that the autocovariance matrix $\hat{\mathbf{R}}(s)$ [Eq. (11)] satisfies the ordinary differential equation

$$\frac{d\hat{\mathbf{R}}^T}{ds} = -\mathbf{A}\hat{\mathbf{R}}^T, \quad \text{for } s \geqslant 0. \tag{21}$$

By post-multiplying both sides of this equation by $\mathbf{C}^{-1}$, we find that $\mathbf{R}(s)$ [defined by Eq. (15)] satisfies the same equation

$$\frac{d\mathbf{R}^T}{ds} = -\mathbf{A}\mathbf{R}^T, \quad \text{for } s \geqslant 0, \tag{22}$$

with the simple initial condition $\mathbf{R}^T(0) = \mathbf{I}$. The solution to this equation (satisfying the initial condition) is[15]

$$\mathbf{R}^T(s) = \exp(-\mathbf{A}s) = \sum_{n=0}^{\infty} \frac{(-1)^n}{n!}\mathbf{A}^n s^n, \quad \text{for } s \geqslant 0, \tag{23}$$

as may be verified by differentiating with respect to s. It has been assumed that the eigenvalues of $\mathbf{A}$ have positive real parts, which is a sufficient condition for $\exp(-\mathbf{A}s)$ to converge to zero as s tends to infinity.

In the case that $\mathbf{A}$ has linearly independent eigenvectors the solution can be written

$$\mathbf{R}^T(s) = \mathbf{V}\exp(-\mathbf{\Lambda}s)\mathbf{V}^{-1}, \quad \text{for } s \geqslant 0, \tag{24}$$

and similarly for $\hat{\mathbf{R}}$

$$\hat{\mathbf{R}}(s)^T = \mathbf{V}\exp(-\mathbf{\Lambda}s)\mathbf{V}^{-1}\mathbf{C}, \quad \text{for } s \geqslant 0. \tag{25}$$

Thus each component of the autocovariance is a linear combination of three decaying exponentials—decaying because the eigenvalues are required to be positive.

For the autocorrelation timescales, $\mathbf{T}$ [Eq. (17)] we obtain

$$\mathbf{T}^T \equiv \int_0^\infty \mathbf{R}^T(s)\,ds = \int_0^\infty \exp(-\mathbf{A}s)\,ds = \mathbf{A}^{-1}. \tag{26}$$

The conclusion from this development is that the matrix of autocorrelation timescales $\mathbf{T}$ of the process $\hat{\mathbf{u}}(\hat{t})$ generated by the stochastic model Eq. (19) is uniquely determined by the drift matrix $\mathbf{A}$ as

$$\mathbf{T} = (\mathbf{A}^{-1})^T. \tag{27}$$

This conclusion depends on the eigenvalues of $\mathbf{A}$ having positive real parts.

B. Covariance

It follows from Eq. (19) that the covariance $\mathbf{C} = \langle \hat{\mathbf{u}}\hat{\mathbf{u}}^T \rangle$ evolves by

$$\frac{d\mathbf{C}}{dt} = -\mathbf{A}\mathbf{C} - \mathbf{C}\mathbf{A}^T + \mathbf{B}\mathbf{B}^T. \tag{28}$$

Given that $\mathbf{B}$ is symmetric and that the process is stationary, this leads to the relation

$$\mathbf{B}^2 = \mathbf{A}\mathbf{C} + \mathbf{C}\mathbf{A}^T. \tag{29}$$

C. Specification of stochastic model coefficients

Can the model coefficients $\mathbf{A}$ and $\mathbf{B}$ be chosen so that the autocovariance $\hat{\mathbf{R}}(s)$ from the model matches that obtained from DNS of homogeneous turbulent shear flow? Clearly the answer is "no," since the empirical autocovariances will not be of the simple form implied by the model—i.e., sums of

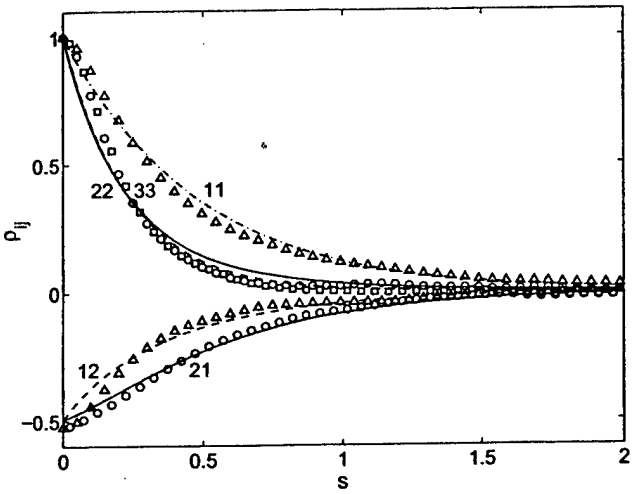

FIG. 3. Comparison of autocorrelation functions $\rho_{ij}(s)$, Eq. (14), from the DNS data (symbols) and from the stochastic model (lines) with coefficients determined from the data [Eq. (32) and Eq. (33)]. (ρ_{22} circles and solid line; ρ_{33} squares and dashed line.)

three exponentials. Nevertheless, the preceding analysis shows that **A** and **B** can be chosen to match the covariance **C** and the timescales **T**. Specifically, given **T**, **A** is determined by

$$\mathbf{A}=(\mathbf{T}^{-1})^T \tag{30}$$

[see Eq. (27)]; then **B** is determined as the symmetric square root of

$$\mathbf{B}^2=\mathbf{AC}+\mathbf{CA}^T \tag{31}$$

[see Eq. (29)]. Evidently this specification requires that **T** be nonsingular. An additional requirement is that **T** and **C** be such that $\mathbf{B}^2$ given by Eq. (31) is positive semi-definite.

For the values of **C** and **T** obtained from the DNS of homogeneous turbulent shear flow, the values of **A** and $\mathbf{B}^2$ obtained from Eq. (30) and Eq. (31) are

$$\mathbf{A}=\begin{bmatrix} 2.45 & 1.24 & 0 \\ 0.65 & 4.90 & 0 \\ 0 & 0 & 4.22 \end{bmatrix}, \tag{32}$$

and

$$\mathbf{B}^2=\begin{bmatrix} 3.90 & -1.18 & 0 \\ -1.18 & 3.84 & 0 \\ 0 & 0 & 5.14 \end{bmatrix}. \tag{33}$$

D. Comparison of autocorrelation functions

Figure 3 shows the comparison between the autocorrelation functions $\rho_{ij}(s)$ obtained from DNS compared to those from the model [with coefficients given by Eq. (32) and Eq. (33)]. Inevitably there are qualitative differences at the origin. For ρ_{11}, for example, the DNS value departs from unity at the origin as $1-\rho_{11}(s)\sim s^2$, whereas the model departs as $1-\rho_{11}(s)\sim|s|$. This leads to the model values of $\rho_{11}(s)$ being below the DNS values at small times; and then, from the matching of the integral timescales, it is not surprising that at some later times the model value exceeds the DNS value. Given these inevitable differences, the agreement between the model and the DNS is as good as could be expected. In particular the model captures the difference between ρ_{11} and the other two diagonal components (which are nearly equal); and the differences between ρ_{12} and ρ_{21}.

IV. GENERALIZED LANGEVIN MODEL

In PDF methods, the stochastic Lagrangian model for velocity that is employed is the generalized Langevin model (GLM).[11,12,7] Applied to homogeneous turbulence, the model for $\mathbf{u}(t)$ is

$$du_i=-\frac{\partial\langle U_i\rangle}{\partial x_j}u_j\,dt+G_{ij}u_j\,dt+(C_0\varepsilon)^{1/2}dW_i, \tag{34}$$

where the constant C_0 is generally ascribed the value 2.1. The coefficient G_{ij} can depend on $\langle u_iu_j\rangle$, ε and $\partial\langle U_i\rangle/\partial x_j$: two particular specifications of G_{ij} are considered below.

The transformation of Eq. (34) to an SDE for $\hat{\mathbf{u}}(\hat{t})$ results in the general stochastic model, Eq. (19), with coefficients

$$A_{ij}=\frac{1}{2}\left(\frac{\mathcal{P}}{\varepsilon}-1\right)\delta_{ij}+\frac{k}{\varepsilon}\frac{\partial\langle U_i\rangle}{\partial x_j}-\frac{k}{\varepsilon}G_{ij}, \tag{35}$$

and

$$B_{ij}=C_0^{1/2}\delta_{ij}. \tag{36}$$

Equation (35) can be rearranged to yield the value of $(k/\varepsilon)G_{ij}$ implied by the DNS:

$$\frac{k}{\varepsilon}\mathbf{G}=\begin{bmatrix} -2.18 & 3.59 & 0 \\ -0.65 & -4.63 & 0 \\ 0 & 0 & -3.95 \end{bmatrix}. \tag{37}$$

Since **B** is found to be anisotropic—as discussed further in the next subsection—no choice of C_0 in Eq. (36) yields the correct diffusion coefficient. Nevertheless, the magnitude of the diffusion is characterized by

$$\hat{C}_0\equiv\tfrac{1}{3}\,\mathrm{trace}(\mathbf{B}^2), \tag{38}$$

the value of which deduced from the DNS is $\hat{C}_0=4.3$. By comparison, the standard model Eq. (36) yields $\hat{C}_0=C_0=2.1$.

A. Anisotropy of the diffusion coefficient

The GLM, and also dispersion models, take the diffusion coefficient **B** to be isotropic, Eq. (36). The reason generally advanced for this specification is consistency with the Kolmogorov hypotheses. For (dimensional) time intervals s in the inertial subrange, $\tau_\eta\ll s\ll k/\varepsilon$ (where τ_η is the Kolmogorov timescale), the Kolmogorov hypotheses predict that the second-order Lagrangian structure function is isotropic and linear in s, i.e.,

$$\langle[u_i(t+s)-u_i(t)][u_j(t+s)-u_j(t)]\rangle=C_0\varepsilon s\,\delta_{ij}, \tag{39}$$

where C_0 is a Kolmogorov constant. The GLM yields precisely this results if C_0 is taken to be C_0.

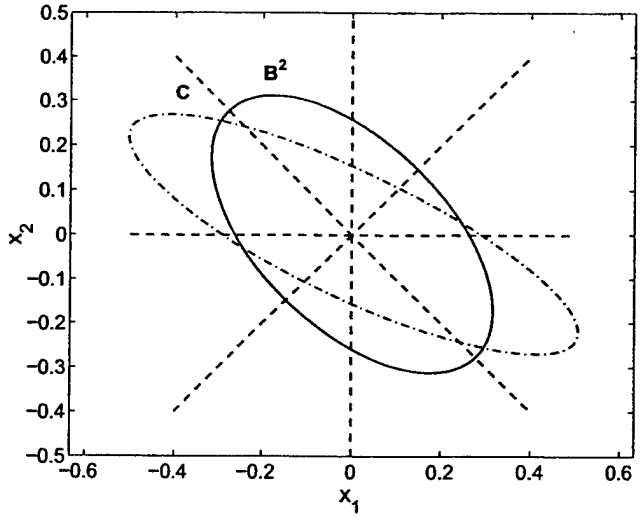

FIG. 4. The scaled tensors $\mathbf{B}^2$ and $\mathbf{C}$ shows as ellipses in the x_1-x_2 plane. The dot-dashed line is $x_i x_j C_{ij}^{-2}=(C_{ii})^{-2}$, and the solid line is the corresponding ellipse for $\mathbf{B}^2$. Shown for reference are dashed lines at 0°, 45°, 90°, and 135°.

However, the value of $\mathbf{B}^2$ deduced from the DNS is decidedly anisotropic: the eigenvalues of $\mathbf{B}^2$ (which are all equal to $C_0=2.1$ in the GLM) are found to be 2.69, 5.06, and 5.14. It is possible that this anisotropy is a Reynolds-number effect, which vanishes at sufficiently high Reynolds number. This possibility could be investigated through DNS at different Reynolds numbers.

It is also possible that the anisotropy in the deduced value of $\mathbf{B}^2$ persists at high Reynolds numbers, not because the Kolmogorov hypothesis [Eq. (39)] is incorrect, but because the stochastic Lagrangian model, Eq. (19), is too simple to represent the multi-timescale aspects of anisotropic turbulence.

Given the observation that $\mathbf{B}^2$ is anisotropic, it is natural to consider modifications to the GLM to incorporate such anisotropy. The natural way to introduce anisotropy in the model is to make the diffusion coefficient dependent on the normalized Reynolds stresses $\mathbf{C}$. But any such model implies that the principal axes of $\mathbf{B}^2$ and $\mathbf{C}$ are aligned, which is not supported by the data. Figure 4 shows the ellipses in the x_1-x_2 plane corresponding to the tensors $\mathbf{B}^2$ and $\mathbf{C}$. The misalignment of the principal axes is evident. In fact, to within 1°, the minor axis of $\mathbf{B}^2$ is aligned with the major axis of the mean rate-of-stain tensor $\mathbf{S}$ (i.e., the 45° line $x_2=x_1$). Hence an anisotropic model for $\mathbf{B}^2$ could be constructed based on $\mathbf{S}$ that is consistent with the DNS data. More data—from different flows and at different Reynolds numbers—are needed before an anisotropic model for $\mathbf{B}^2$ of any generality can be constructed.

B. Simplified Langevin model

In this and the next subsection we examine two specific forms of the generalized Langevin model, corresponding to particular specifications of G_{ij}.

For the simplified Langevin model (SLM) considered here, the specification is

TABLE I. Values of the mean timescale $T\equiv\frac{1}{3}$ trace($\mathbf{T}$), the normalized Reynolds stress C_{ij}, and the turbulence-to-shear timescale ratio $\mathcal{S}k/\varepsilon$ from the DNS of Sawford and Yeung (Ref. 5) and from SLM and LIPM for different values of C_0 and α_2.

	DNS	SLM	SLM	LIPM	LIPM
C_0	-	2.1	3.4	2.1	4.4
α_2	-	-	-	3.5	11.9
T	0.30	0.43	0.30	0.63	0.30
C_{11}	0.96	1.10	0.98	1.02	1.02
C_{22}	0.43	0.45	0.51	0.49	0.49
C_{33}	0.61	0.51	0.51	0.49	0.49
C_{12}	−0.32	−0.39	−0.34	−0.36	−0.36
$\mathcal{S}k/\varepsilon$	4.83	4.02	4.47	4.28	4.28

$$G_{ij}=-\left(\frac{1}{2}+\frac{3}{4}C_0\right)\frac{\varepsilon}{k}\delta_{ij}, \tag{40}$$

so that the matrix $\mathbf{A}$ [Eq. (35)] is

$$\mathbf{A}=\begin{bmatrix}\lambda & \sigma & 0\\ 0 & \lambda & 0\\ 0 & 0 & \lambda\end{bmatrix}, \tag{41}$$

with

$$\lambda=\frac{1}{2}\frac{\mathcal{P}}{\varepsilon}+\frac{3}{4}C_0, \tag{42}$$

and

$$\sigma=\mathcal{S}k/\varepsilon.$$

Evidently all three eigenvalues of $\mathbf{A}$ are equal to λ, and the eigenvectors are not independent—two are equal to $[1\,0\,0]^T$. Consequently, the autocovariance $\hat{\mathbf{R}}(s)$ is not given by Eq. (25), but instead the solution to Eq. (21) is

$$\hat{\mathbf{R}}(s)=e^{-\lambda s}\begin{bmatrix}C_{11}-\sigma s C_{12} & C_{12} & 0\\ C_{21}-\sigma s C_{22} & C_{22} & 0\\ 0 & 0 & C_{33}\end{bmatrix}. \tag{43}$$

Given a specified value of C_0 and the DNS value of $\mathcal{P}/\varepsilon$, Eq. (31) can be solved to determine the normalized Reynolds stresses $\mathbf{C}$ given by SLM in homogeneous turbulent shear flow, and then the autocovariances can be evaluated from Eq. (43). We consider two values of C_0: the standard value $C_0=2.1$; and the value $C_0=3.4$ for which the SLM timescale λ^{-1} matches the average DNS timescale $T\equiv\frac{1}{3}$ trace ($\mathbf{T}$). The values of $\mathbf{C}$ obtained are shown in Table I.

The autocorrelations $\rho_{ij}(s)$ obtained with $C_0=3.4$ are compared to the DNS data in Fig. 5. As expected, the agreement is much better with the timescales matched ($C_0=3.4$) than otherwise ($C_0=2.1$, not shown). The model correctly predicts the equality of ρ_{22} and ρ_{33} and their distinction from ρ_{11}, but the quantitative agreement is noticeably poorer than in Fig. 3.

The model predicts a more substantial difference between $\rho_{12}(s)$ and $\rho_{21}(s)$ than is evident in the DNS—a behavior which is easily understood. The only off-diagonal term [σ in Eq. (41)] enters the SDE for velocity as

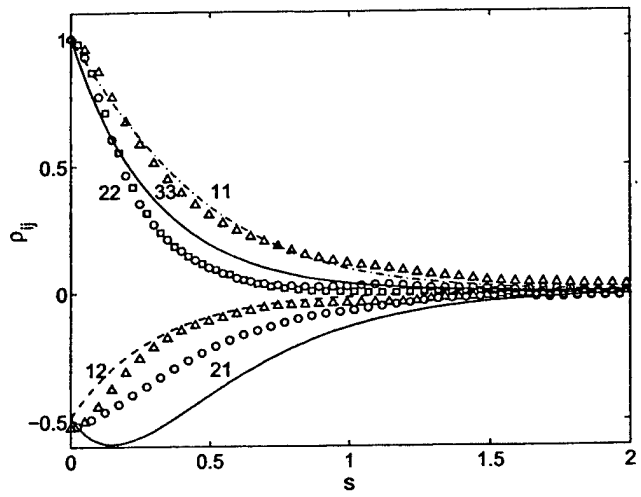

FIG. 5. Comparison of autocorrelation functions $\rho_{ij}(s)$, Eq. (14), from DNS (symbols) and from SLM with $C_0=3.4$. (For SLM, $\rho_{22}=\rho_{33}$.)

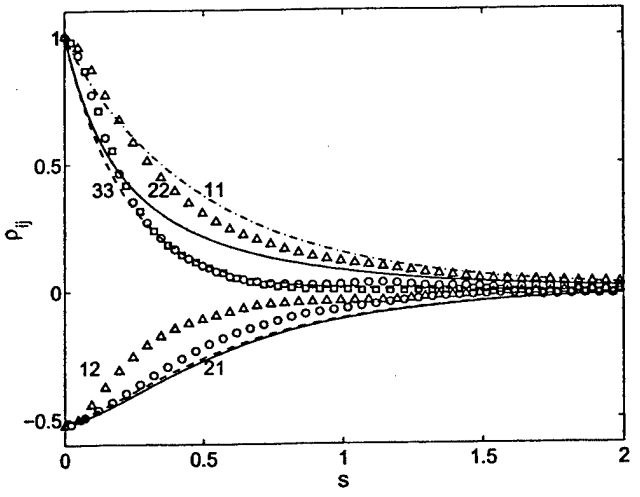

FIG. 6. Comparison of autocorrelation functions $\rho_{ij}(s)$, Eq. (14), from DNS (symbols) and from LIPM with $C_0=4.4$ and $\alpha_2=11.9$ (lines). Dashed lines, ρ_{12} and ρ_{33}; solid lines, ρ_{21} and ρ_{22}.

$$d\hat{u}_1=-\frac{\mathcal{S}k}{\varepsilon}\hat{u}_2\,d\hat{t}\ldots. \tag{44}$$

Thus large positive (or negative) values of $\hat{u}_2$ tend to lead to large negative (or positive) values of $\hat{u}_1$ after a time lag. Thus the peak correlation $|\langle\hat{u}_2(\hat{t})\hat{u}_1(\hat{t}+s)\rangle|$—or equivalently the minimum of $\rho_{21}(s)$—occurs for a positive value of s. The model overestimates this effect, because it takes no account of rapid pressure fluctuations which tend to counteract the effects of mean shear.

C. Lagrangian isotropization of production model (LIPM)

The LIPM[14,7] corresponds closely to the Launder, Reece, and Rodi[16] Reynolds-stress model. Using standard values for the model constants β_{1-3} and γ_{1-6}, the LIPM equation for $\mathbf{G}$ is

$$\frac{k}{\varepsilon}\mathbf{G}=\alpha_1\mathbf{I}+\alpha_2(\mathbf{b}-3\mathbf{b}^2)+\frac{\mathcal{S}k}{\varepsilon}\begin{bmatrix}-\frac{3}{5}b_{12} & \frac{4}{5}+\frac{3}{5}b_{11} & 0\\ -\frac{1}{5}-\frac{3}{5}b_{22} & \frac{3}{5}b_{12} & 0\\ 0 & 0 & 0\end{bmatrix}, \tag{45}$$

where $\mathbf{b}$ is the anisotropy tensor

$$\mathbf{b}=\frac{1}{2}\mathbf{C}-\frac{1}{3}\mathbf{I}, \tag{46}$$

the standard value of the constant α_2 is $\alpha_2=3.5$, and the coefficient α_1 is given by

$$\alpha_1=-\left(\frac{1}{2}+\frac{3}{4}C_0\right)+\frac{3}{10}\frac{\mathcal{P}}{\varepsilon}+3\alpha_2\mathrm{trace}(\mathbf{b}^3). \tag{47}$$

With the standard value $C_0=2.1$, the model yields reasonable values of the normalized Reynolds stresses, but the average time scale $T\equiv\frac{1}{3}\,\mathrm{trace}(\mathbf{T})$ is more than twice the DNS value; see Table I. As a consequence, the model (with $C_0=2.1$) produces autocorrelations $\rho_{ij}(s)$ (not shown) in very poor agreement with the DNS data.

To provide a more meaningful comparison, the constants C_0 and α_2 are adjusted to match the average timescale, while leaving the normalized Reynolds stresses the same. The autocorrelations given by LIPM with these values ($C_0=4.4$, $\alpha_2=11.9$) are compared to the DNS data in Fig. 6. The agreement is quite poor. Except at small times, $\rho_{22}(s)$ is incorrectly predicted to be larger than $\rho_{33}(s)$; and evidently the effect of the rapid pressure is overpredicted as there is little difference between $\rho_{12}(s)$ and $\rho_{21}(s)$.

This last point can be seen directly in the matrix $\mathbf{A}$, which for LIPM is

$$\mathbf{A}=\begin{bmatrix}2.86 & 1.99 & 0\\ 2.21 & 6.11 & 0\\ 0 & 0 & 4.48\end{bmatrix}. \tag{48}$$

The direct effect of shear appears in the 1–2 component, and in SLM the 2–1 component is zero. In $\mathbf{A}$ deduced from the DNS data [Eq. (32)], A_{21} as about half of A_{12}; but for LIPM A_{21} exceeds A_{12}.

V. CONCLUSIONS

As previously observed by Sawford and Yeung[4,5] in the context of turbulent dispersion, Lagrangian data from DNS of homogeneous turbulence is valuable in the development and testing of stochastic Lagrangian models. After an initial transient, homogeneous turbulent shear becomes (approximately) self-similar, so that the appropriately scaled Lagrangian velocity fluctuation $\hat{\mathbf{u}}(\hat{t})$ becomes a statistically stationary random process.

The stochastic Lagrangian model considered for $\hat{\mathbf{u}}(\hat{t})$ is the diffusion process Eq. (19) in which the drift coefficient depends linearly on $\hat{\mathbf{u}}(\hat{t})$ through the drift matrix $\mathbf{A}$, and the (anisotropic) diffusion coefficient $\mathbf{B}$ is constant. An analysis of this model shows that there is a unique specification of $\mathbf{A}$

and **B** [Eq. (30) and Eq. (31)] such that the covariance matrix **C** and the timescale matrix **T** match those obtained from DNS. The autocorrelation functions predicted by the model are in good agreement with the DNS data (except at small times). The model for $\hat{\mathbf{u}}(\hat{t})$ is a continuous, Gaussian, Markov process; and it is a significant conclusion that such a simple process provides a good model for the Lagrangian velocity in homogeneous turbulent shear flow. (It is known that the one-point one-time joint PDF of velocity is jointly normal[1] in this flow.)

Contrary to conventional modelling assumptions, if is found that the diffusion coefficient **B** is significantly anisotropic. Whether or not this is a low Reynolds-number effect is an important question which can be addressed in future DNS studies.

The magnitude of the diffusion coefficient can be characterized by $\hat{C}_0 \equiv \frac{1}{3}\,\mathrm{trace}(\mathbf{B}^2)$ and the value deduced from the DNS data is $\hat{C}_0 = 4.3$. This is substantially larger than the corresponding value $C_0 = 2.1$ normally used in PDF models.

There is evidence that the appropriate value of C_0 depends on Reynolds number.[13,10] In the DNS, the Taylor-scale Reynolds number based on x_1-direction statistics increases from $R_\lambda \approx 40$ to $R_\lambda \approx 110$ during the course of the simulation. Sawford and Yeung[5] provide an empirical expression for C_0 as a function of R_λ, which increase from $C_0 = 3.7$ at $R_\lambda = 40$ to $C_0 = 5.4$ at $R_\lambda = 110$. The value $C_0 = 4.3$ deduced from the DNS lies within this range, but Reynolds-number effects are not addressed here.

The autocorrelation functions predicted by two generalized Langevin models are compared to the DNS data in Figs. 5 and 6. In the simplified Langevin model (SLM), no account is taken of the rapid pressure fluctuations, and as a consequence the difference between $\rho_{12}(s)$ and $\rho_{21}(s)$ is overpredicted. The Lagrangian IP model (LIPM)—which includes a model for the rapid pressure—yields autocorrelations in poor agreement with the DNS data.

In the specification of both the drift and diffusion coefficients, there is clearly scope for considerable improvement in generalized Langevin models.

ACKNOWLEDGMENTS

The author is grateful to Professor P. K. Yeung and Dr. B. L. Sawford for making available their DNS data; to Professor D. L. Koch and J. Chen for discussions on the solution of the stochastic model equations; and to Professor R. O. Fox for clarifying the necessary conditions for the satisfaction of Eq. (23). This work was supported by Air Force Office of Scientific Research Grant No. F49620-00-1-0171.

[1] S. Tavoularis and S. Corrsin, "Experiments in nearly homogeneous turbulent shear flow with a uniform mean temperature gradient. Part 1," J. Fluid Mech. **104**, 311 (1981).
[2] M. M. Rogers and P. Moin, "The structure of the vorticity field in homogeneous turbulent flows," J. Fluid Mech. **176**, 33 (1987).
[3] P. Shen and P. K. Yeung, "Fluid particle dispersion in homogeneous turbulent shear," Phys. Fluids **9**, 3472 (1997).
[4] B. L. Sawford and P. K. Yeung, "Eulerian acceleration statistics as a discriminator between Lagrangian stochastic models in uniform shear flow," Phys. Fluids **12**, 2033 (2000).
[5] B. L. Sawford and P. K. Yeung, "Lagrangian statistics in uniform shear flow: Direct numerical simulation and Lagrangian stochastic models," Phys. Fluids **13**, 2627 (2001).
[6] S. B. Pope, "Lagrangian PDF methods for turbulent flows," Annu. Rev. Fluid Mech. **26**, 23 (1994).
[7] S. B. Pope, *Turbulent Flows* (Cambridge University Press, Cambridge, 2000).
[8] G. I. Taylor, "Diffusion by continuous movements," Proc. London Math. Soc. **20**, 196 (1921).
[9] D. J. Thomson, "Criteria for the selection of stochastic models of particle trajectories in turbulent flows," J. Fluid Mech. **180**, 529 (1987).
[10] B. L. Sawford, "Rotation in Lagrangian stochastic models of turbulent dispersion," Boundary-Layer Meteorol. **93**, 411 (1999).
[11] S. B. Pope, "A Lagrangian two-time probability density function equation for inhomogeneous turbulent flows," Phys. Fluids **26**, 3448 (1983).
[12] D. C. Haworth and S. B. Pope, "A generalized Langevin model for turbulent flows," Phys. Fluids **29**, 387 (1986).
[13] P. K. Yeung and S. B. Pope, "Lagrangian statistics from direct numerical simulations of isotropic turbulence," J. Fluid Mech. **207**, 531 (1989).
[14] S. B. Pope, "On the relationship between stochastic Lagrangian models of turbulence and second-moment closures," Phys. Fluids **6**, 973 (1994).
[15] C. W. Gardiner, *Handbook of Stochastic Methods for Physics, Chemistry and the Natural Sciences*, 2nd ed. (Springer-Verlag, Berlin, 1985).
[16] B. E. Launder, G. J. Reece, and W. Rodi, "Progress in the development of a Reynolds-stress turbulence closure," J. Fluid Mech. **68**, 537 (1975).

Velocity filtered density function for large eddy simulation of turbulent flows

L. Y. M. Gicquel and P. Givi[a)]
Department of Mechanical and Aerospace Engineering, University at Buffalo, State University of New York, Buffalo, New York 14260-4400

F. A. Jaberi
Department of Mechanical Engineering, Michigan State University, East Lansing, Michigan 48824-1226

S. B. Pope
Sibley School of Mechanical and Aerospace Engineering, Cornell University, Ithaca, New York 14853-1301

(Received 30 April 2001; accepted 29 November 2001)

A methodology termed the "velocity filtered density function" (VFDF) is developed and implemented for large eddy simulation (LES) of turbulent flows. In this methodology, the effects of the unresolved subgrid scales (SGS) are taken into account by considering the joint probability density function of all of the components of the velocity vector. An exact transport equation is derived for the VFDF in which the effects of the SGS convection appear in closed form. The unclosed terms in this transport equation are modeled. A system of stochastic differential equations (SDEs) which yields statistically equivalent results to the modeled VFDF transport equation is constructed. These SDEs are solved numerically by a Lagrangian Monte Carlo procedure in which the Itô–Gikhman character of the SDEs is preserved. The consistency of the proposed SDEs and the convergence of the Monte Carlo solution are assessed by comparison with results obtained by an Eulerian LES procedure in which the corresponding transport equations for the first two SGS moments are solved. The VFDF results are compared with those obtained via several existing SGS closures. These results are also analyzed via *a priori* and *a posteriori* comparisons with results obtained by direct numerical simulation of an incompressible, three-dimensional, temporally developing mixing layer. [DOI: 10.1063/1.1436496]

I. INTRODUCTION

The probability density function (PDF) approach has proven useful for large eddy simulation (LES) of turbulent reacting flows.[1–15] The formal means of conducting such LES is by consideration of the "filtered density function" (FDF) which is essentially the filtered fine-grained PDF of the transport quantities. In all previous contributions, the FDF of the "scalar" quantities is considered: Gao and O'Brien,[3] Colucci *et al.*,[6] Réveillon and Vervisch,[7] and Zhou and Pereira[12] developed a transport equation for the FDF in constant density turbulent reacting flows. Jaberi *et al.*[8] extended the methodology for LES of variable density flows by consideration of the "filtered mass density function" (FMDF), which is essentially the mass weighted FDF. The fundamental property of the PDF methods is exhibited by the closed form nature of the chemical source term appearing in the transport equation governing the FDF (FMDF). This property is very important as evidenced in several applications of FDF for LES of a variety of turbulent reacting flows.[6–10,12] However, since the FDF of only the scalar quantities are considered, all of the "hydrodynamic" effects are modeled. In all previous LES/FDF simulations, these effects have been modeled via "non-FDF" methods.

The objective of the present work is to extend the FDF methodology to also include the subgrid scale (SGS) velocity vector. This is facilitated by consideration of the joint "velocity filtered density function" (VFDF). With the definition of the VFDF, the mathematical framework for its implementation in LES is established. A transport equation is developed for the VFDF in which the effects of SGS convection are shown to appear in closed form. The unclosed terms in this equation are modeled in a fashion similar to that in the Reynolds-averaged simulation (RAS) procedures. A Lagrangian Monte Carlo procedure is developed and implemented for numerical simulation of the modeled VFDF transport equation. The consistency of this procedure is assessed by comparing the first two moments of the VFDF with those obtained by the Eulerian finite difference solutions of the same moments transport equations. The results of the VFDF simulations are compared with those predicted by the Smagorinsky[16] closure, and the "dynamic" Smagorinsky model.[17–19] The VFDF results are also assessed via comparisons with direct numerical simulation (DNS) data of a three-dimensional (3D) temporally developing mixing layer in a context similar to that of Vreman *et al.*[20]

This work deals with LES of the velocity field in a constant density, nonreacting flow. Consideration of the joint

a)Author to whom correspondence should be addressed. Telephone: (716) 645-2593 (ext. 2320); Fax: (716) 645-3875. Electronic mail: givi@eng.buffalo.edu

Note that these models (i.e., the first two terms on the right-hand sides of Eqs. (18) and (19) are the same, but that they model slightly different quantities. With this closure, the two terms in G_{ij} and ε jointly represent the SGS pressure-strain and SGS dissipation. These are modeled as[11,26]

$$G_{ij}=-\omega\left(\frac{1}{2}+\frac{3}{4}C_0\right)\delta_{ij}, \quad \varepsilon=C_\varepsilon k^{3/2}/\Delta_L, \quad \omega=\varepsilon/k, \tag{20}$$

where ω is the SGS mixing frequency, Δ_L is the filter width, $k=\frac{1}{2}\tau_L(u_i,u_i)$ is the SGS kinetic energy, and $\varepsilon=\frac{1}{2}\varepsilon_{ii}$ is the SGS dissipation rate.

With the GLM, the two forms of the VFDF transport equation are

$$\begin{aligned}\frac{DP_L}{Dt}=&-\frac{\partial}{\partial x_k}[(v_k-\langle u_k\rangle_L)P_L]+\frac{\partial\langle p\rangle_L}{\partial x_i}\frac{\partial P_L}{\partial v_i}+\nu\frac{\partial^2 P_L}{\partial x_k\partial x_k}\\&+\nu\frac{\partial\langle u_i\rangle_L}{\partial x_k}\frac{\partial\langle u_j\rangle_L}{\partial x_k}\frac{\partial^2 P_L}{\partial v_i\partial v_j}+2\nu\frac{\partial\langle u_i\rangle_L}{\partial x_k}\frac{\partial^2 P_L}{\partial x_k\partial v_i}\\&-\frac{\partial}{\partial v_i}[G_{ij}(v_j-\langle u_j\rangle_L)P_L]+\frac{1}{2}C_0\varepsilon\frac{\partial^2 P_L}{\partial v_i\partial v_i},\end{aligned} \tag{21}$$

for VFDF1, and

$$\begin{aligned}\frac{DP_L}{Dt}=&-\frac{\partial}{\partial x_k}[(v_k-\langle u_k\rangle_L)P_L]+\frac{\partial\langle p\rangle_L}{\partial x_i}\frac{\partial P_L}{\partial v_i}\\&-\frac{\partial\langle\sigma_{ik}\rangle_L}{\partial x_k}\frac{\partial P_L}{\partial v_i}-\frac{\partial}{\partial v_i}[G_{ij}(v_j-\langle u_j\rangle_L)P_L]\\&+\frac{1}{2}C_0\varepsilon\frac{\partial^2 P_L}{\partial v_i\partial v_i}\end{aligned} \tag{22}$$

for VFDF2. Hereinafter, Eqs. (21) and (22) are referred to as "VFDF1" and "VFDF2," respectively. The difference between these two equations is in the different treatment of the closed viscous terms.

D. Transport equations for moments

The zeroth, first, and second moment equations corresponding to these two formulations are

for VFDF1:

$$\frac{\partial\langle u_i\rangle_L}{\partial x_i}=0,$$

$$\begin{aligned}&\frac{\partial\langle u_j\rangle_L}{\partial t}+\frac{\partial\langle u_i\rangle_L\langle u_j\rangle_L}{\partial x_i}\\&\quad=-\frac{\partial\langle p\rangle_L}{\partial x_j}+\nu\frac{\partial^2\langle u_j\rangle_L}{\partial x_i\partial x_i}-\frac{\partial\tau_L(u_i,u_j)}{\partial x_i},\end{aligned} \tag{23}$$

$$\begin{aligned}&\frac{\partial}{\partial t}[\tau_L(u_i,u_j)]+\frac{\partial}{\partial x_k}[\langle u_k\rangle_L\tau_L(u_i,u_j)]\\&\quad=-\frac{\partial}{\partial x_k}\left[\tau_L(u_i,u_j,u_k)-\nu\frac{\partial}{\partial x_k}[\tau_L(u_i,u_j)]\right]\\&\qquad+G_{ik}\tau_L(u_j,u_k)+G_{jk}\tau_L(u_i,u_k)-\tau_L(u_i,u_k)\frac{\partial\langle u_j\rangle_L}{\partial x_k}\\&\qquad-\tau_L(u_j,u_k)\frac{\partial\langle u_i\rangle_L}{\partial x_k}+C_0\varepsilon\delta_{ij},\end{aligned} \tag{24}$$

for VFDF2:

$$\frac{\partial\langle u_i\rangle_L}{\partial x_i}=0,$$

$$\begin{aligned}&\frac{\partial\langle u_j\rangle_L}{\partial t}+\frac{\partial\langle u_i\rangle_L\langle u_j\rangle_L}{\partial x_i}\\&\quad=-\frac{\partial\langle p\rangle_L}{\partial x_j}+\nu\frac{\partial^2\langle u_j\rangle_L}{\partial x_i\partial x_i}-\frac{\partial\tau_L(u_i,u_j)}{\partial x_i},\end{aligned} \tag{25}$$

$$\begin{aligned}&\frac{\partial}{\partial t}[\tau_L(u_i,u_j)]+\frac{\partial}{\partial x_k}[\langle u_k\rangle_L\tau_L(u_i,u_j)]\\&\quad=-\frac{\partial}{\partial x_k}[\tau_L(u_i,u_j,u_k)]+G_{ik}\tau_L(u_j,u_k)+G_{jk}\tau_L(u_i,u_k)\\&\qquad-\tau_L(u_i,u_k)\frac{\partial\langle u_j\rangle_L}{\partial x_k}-\tau_L(u_j,u_k)\frac{\partial\langle u_i\rangle_L}{\partial x_k}+C_0\varepsilon\delta_{ij}.\end{aligned} \tag{26}$$

It may be seen that the zeroth and first moment equations are identical (and exact); whereas the second central moment equations differ by the additional viscous term in VFDF1 [Eq. (24)]. A comparison of these modeled equations with Eq. (5) shows that the GLM model implies

$$-\Pi_{ij}-(\varepsilon_{ij}-\tfrac{2}{3}\varepsilon\delta_{ij})=-C_1\omega[\tau_L(u_i,u_j)-\tfrac{2}{3}k\delta_{ij}], \qquad C_1=1+\tfrac{3}{2}C_0. \tag{27}$$

This is the same as the Rotta[33] model as shown by Pope.[34] There are two model constants in the VFDF equation. In RAS, typically[34,35] $C_\varepsilon\approx 1$, and $C_0\approx 2.1$ ($C_1=4.15$). As shown in Refs. 27, 34 boundedness of the GLM coefficients $C_0>0$ guarantees that the SGS stress is realizable.

IV. EQUIVALENT STOCHASTIC SYSTEMS

The solution of the VFDF transport equation provides all the statistical information pertaining to the velocity vector. The most convenient means of solving this equation is via the Lagrangian Monte Carlo scheme. The basis of this scheme relies upon the principle of equivalent systems.[26,32] Two systems with different instantaneous behaviors may have identical statistics and satisfy the same PDF transport equation. In this context, the general diffusion process is considered via the following system of stochastic differential equations (SDEs):[26,31,36,37]

$$\begin{aligned}d\mathcal{X}(t)=&D_i(\mathcal{X}(t),\mathcal{U}(t);t)dt+B(\mathcal{X}(t),\mathcal{U}(t);t)dW_i^x(t),\\d\mathcal{U}_i(t)=&M_i(\mathcal{X}(t),\mathcal{U}(t);t)dt+E(\mathcal{X}(t),\mathcal{U}(t);t)dW_i^v(t)\\&+F_{ij}(\mathcal{X}(t),\mathcal{U}(t);t)dW_j^x(t),\end{aligned} \tag{28}$$

where $\mathcal{X}_i$ and $\mathcal{U}_i$ are probabilistic representations of $\mathbf{x}$ and $\boldsymbol{u}$, respectively. The coefficients D_i and M_i are the "drift" in the phase space of position and velocity, respectively. The terms B and E are the "diffusion" coefficients for physical and velocity spaces, respectively; and W_i^x and W_i^v denote independent Wiener–Lévy processes.[38] The tensor F_{ij} represents the dependency between the velocity and physical spaces. This term is needed to satisfy the Itô condition for

$B \neq 0$. A comparison of the Fokker–Planck equation of Eq. (28) with the modeled VFDF1 transport equation, Eq. (21) yields

$$M_i \equiv -\frac{\partial \langle p \rangle_L}{\partial x_i} + 2\nu \frac{\partial^2 \langle u_i \rangle_L}{\partial x_k \partial x_k} + G_{ij}(\mathcal{U}_j - \langle u_j \rangle_L), \quad D_i \equiv \mathcal{U}_i,$$
$$B \equiv \sqrt{2\upsilon}, \quad E \equiv \sqrt{C_0 \varepsilon}, \quad F_{ij} \equiv \sqrt{2\nu} \frac{\partial \langle u_i \rangle_L}{\partial x_j}. \tag{29}$$

Therefore, the proper SDEs which represent VFDF1 in the Lagrangian sense are

$$d\mathcal{X}_i(t) = \mathcal{U}_i(t)dt + \sqrt{2\nu} dW_i^x(t),$$
$$d\mathcal{U}_i(t) = \left[-\frac{\partial \langle p \rangle_L}{\partial x_i} + 2\nu \frac{\partial^2 \langle u_i \rangle_L}{\partial x_k \partial x_k} + G_{ij}(\mathcal{U}_j(t) - \langle u_j \rangle_L) \right] dt + \sqrt{C_0 \varepsilon} dW_i^v(t) + \sqrt{2\nu} \frac{\partial \langle u_i \rangle_L}{\partial x_j} dW_j^x(t). \tag{30}$$

This stochastic system is the same as that developed by Dreeben and Pope[29–31] for RAS.

For VFDF2, due to the absence of diffusion in physical space we must have $B = 0$. Therefore, the corresponding SDEs are

$$d\mathcal{X}_i(t) = \mathcal{U}_i(t)dt,$$
$$d\mathcal{U}_i(t) = \left[-\frac{\partial \langle p \rangle_L}{\partial x_i} + \frac{\partial \langle \sigma_{ik} \rangle_L}{\partial x_k} + G_{ij}(\mathcal{U}_j(t) - \langle u_j \rangle_L) \right] dt + \sqrt{C_0 \varepsilon} dW_i^v(t). \tag{31}$$

This system is the same as that suggested by Pope[26] and Haworth and Pope[27] for RAS.

The primary difference between the two formulations VFDF1 and VFDF2 is due to molecular effects in the spatial diffusion of the VFDF. This is explicitly included in the VFDF1 formulation and is also present in the corresponding second moment equation. This difference is expected to be important in flows where viscous effects are important; e.g., flow near solid boundaries.[29–31] Both of these formulation are considered in our numerical simulations as discussed below.

V. NUMERICAL SOLUTION PROCEDURE

Numerical solution of the modeled VFDF transport equation is obtained by a Lagrangian Monte Carlo procedure. The basis of this procedure is the same as that in RAS[39–41] and in previous LES/FDF.[6,8] But there are some subtle differences which are explained here. In the Lagrangian description, the VFDF is represented by an ensemble of N statistically identical Monte Carlo particles. Each of these particles carries information pertaining to its velocity $\mathbf{U}^{(n)}(t)$ and position $\mathbf{X}^{(n)}(t)$, $n = 1,2,...N$. This information is updated via temporal integration of Eq. (28). The simplest means of performing this integration is via the Euler–Maruyamma approximation[42]

$$X_i^n(t_{k+1}) = X_i^n(t_k) + D_i^n(t_k)\Delta t + B^n(t_k)(\Delta t)^{1/2} \zeta_i^n(t_k),$$
$$U_i^n(t_{k+1}) = U_i^n(t_k) + M_i^n(t_k)\Delta t + E^n(t_k)(\Delta t)^{1/2} \xi_i^n(t_k) + F_{ij}^n(t_k)(\Delta t)^{1/2} \zeta_j^n(t_k), \tag{32}$$

where $D_i^n(t_k) = D_i(\mathbf{X}^{(n)}(t_k), \mathbf{U}^{(n)}(t_k); t)$, $B^{(n)}(t_k) = B(\mathbf{X}^{(n)}(t_k), \mathbf{U}^{(n)}(t_k); t), \ldots$ and $\xi_i^n(t_k)$, $\zeta_j^n(t_k)$ are independent standardized Gaussian random variables. This formulation preserves the Markovian character of the diffusion processes[43,44] and facilitates affordable computations. Higher-order numerical schemes for solving Eq. (28) are available,[42] but one must be cautious in using them for LES.[6] Since the diffusion term in Eq. (28) strongly depends on the stochastic processes, the numerical scheme must be consistent with Itô–Gikhman[45,46] calculus. Equation (32) exhibits this property.

The statistics are evaluated by consideration of the ensemble of particles in a "finite volume" centered at a spatial location. This ensemble provides "one-time" statistics. This finite volume is characterized by a cubic box of length Δ_E. This is necessary as, with probability one, no particle will coincide with the point as considered.[32] Here, a cubic box of size Δ_E is used to construct the ensemble mean, variances and covariances of the velocity vector. These values are used in the finite difference LES solver of Eq. (4) as described below.

The SGS dissipation rate and the SGS mixing frequency as required in the solution of the VFDF are evaluated on the finite difference grid points and interpolated to the particle's location. Ideally, for reliable Eulerian statistics and minimum numerical dispersion, it is desired to have the size of the sample domain infinitesimally small (i.e., $\Delta_E \to 0$) and the number of particles within this domain infinitely large. That is

$$P_L(\boldsymbol{v};\mathbf{x},t) \xleftarrow[\substack{N_E \to \infty \\ \Delta_E \to 0}]{} \mathcal{P}_{N_E}(\boldsymbol{v};\mathbf{x},t) \equiv \frac{1}{N_E} \sum_{n \in \Delta_E} \delta(\boldsymbol{v} - \boldsymbol{u}^{(n)}), \tag{33}$$

where $\mathcal{P}_{N_E}$ is the Eulerian PDF constructed from the particle ensemble, $n \in \Delta_E$ denotes the particles contained in an ensemble box of length Δ_E centered at $\mathbf{x}$; and N_E is the total number of particles within the box. With a finite number of particles, obviously a larger Δ_E is needed. This compromise between the statistical accuracy and dispersive accuracy implies that the optimum magnitude of Δ_E cannot, in general, be specified *a priori*.[11,26] This does not diminish the capability of the procedure, but exemplifies the importance of the parameters governing the statistics.

To provide an estimate of the proper Δ_E size, a "point estimator" procedure is considered. With this procedure, the mean values (the first moments of the VFDF) are evaluated by ensemble averaging, and spatial variations of these mean values within the box are ignored. With the discrete representation [Eq. (32)], the first two moments in this procedure are evaluated via

TABLE I. Recapitulation of the VFDF solution procedures.

	Finite difference variables	Particle solver variables	Particle statistics used by the finite difference solver	Finite difference variables used by particle solver	Redundant quantities
VFDF 1	$\langle u_i\rangle_L$	X_i	$\tau_L(u_i,u_j)$	$\langle u_i\rangle_L, \frac{\partial\langle p\rangle_L}{\partial x_i}$	$\langle u_i\rangle_L$
	$\langle p\rangle_L$	U_i		$\frac{\partial\langle u_i\rangle_L}{\partial x_k}, \frac{\partial^2\langle u_i\rangle_L}{\partial x_k\partial x_k}$	
VFDF 2	$\langle u_i\rangle_L$	X_i	$\tau_L(u_i,u_j)$	$\langle u_i\rangle_L, \frac{\partial\langle p\rangle_L}{\partial x_i}$	$\langle u_i\rangle_L$
	$\langle p\rangle_L$	U_i		$\frac{\partial^2\langle u_i\rangle_L}{\partial x_k\partial x_k}$	
LES-FD	$\langle u_i\rangle_L, \langle p\rangle_L$	X_i	$\tau_L(u_i,u_j,u_k)$	$\langle u_i\rangle_L, \frac{\partial\langle p\rangle_L}{\partial x_i}$	$\langle u_i\rangle_L$
	$\tau_L(u_i,u_j)$	U_i		$\frac{\partial^2\langle u_i\rangle_L}{\partial x_k\partial x_k}$	$\tau_L(u_i,u_j)$

$$\langle u_i\rangle_L \xleftarrow[\substack{N_E\to\infty\\ \Delta_E\to 0}]{} \frac{1}{N_E}\sum_{n\in\Delta_E} U_i^{(n)} \equiv \langle U_i\rangle_E,$$

$$\tau_L(u_i,u_j) \xleftarrow[\substack{N_E\to\infty\\ \Delta_E\to 0}]{} \frac{1}{N_E-1}\sum_{n\in\Delta_E} (U_i^{(n)}-\langle U_i\rangle_E)(U_j^{(n)}-\langle U_j\rangle_E). \tag{34}$$

The point estimator is obviously subject to both statistical errors and dispersive errors for $\Delta_E \neq 0$.

To determine the pressure field, the "mean-field solver" is based on the "compact parameter" finite difference scheme of Carpenter.[47] This is a variant of the McCormack[48] scheme in which fourth-order compact differences are used to approximate the spatial derivatives, and a second-order symmetric predictor-corrector sequence is employed for time discretization. The numerical algorithm is a hyperbolic solver which considers a fully compressible flow. Here, the simulations are conducted with a low Mach number ($M \leq 0.3$) to minimize compressibility effects. All the finite difference operations are conducted on fixed and equally sized grid points. The transfer of information from these points to the location of the Lagrangian particles is conducted via interpolation. A second-order (bilinear) interpolation scheme is used for this purpose. The results of previous work indicate no significant improvements with the use of higher order interpolation schemes.[6]

The mean-field solver also determines the filtered velocity field. That is, there is a "redundancy" in the determination of the first filtered moments as both the finite difference and the Monte Carlo procedures provides the solution of this field. This redundancy is actually very useful in monitoring the accuracy of the simulated results. Detailed discussions pertaining to this issue are provided in Refs. 8, 39–41.

To establish the consistency of the VFDF solver, another LES is also conducted in which the modeled transport equations for the filtered velocity and the generalized SGS stresses are solved strictly via the finite difference scheme. These simulations are referred to as LES-FD and are only applied for the case corresponding to VFDF2. That is, Eqs. (25) and (26) are considered. Since the SGS transport terms $\tau_L(u_i,u_j,u_k)$ are unclosed in Eq. (26), the values corresponding to these terms are taken from the Monte Carlo solver and substituted in the SGS stress transport equations. The attributes of all of the scheme are summarized in Table I, with further discussions in Refs. 6, 39–41.

VI. RESULTS

A. Flows simulated

Simulations are conducted of a two-dimensional (2D) planar jet, and a 3D temporally developing mixing layer. The jet flow simulations are conducted primarily for establishing the consistency of the Lagrangian Monte Carlo solver. For this purpose, 2D simulations are sufficient. To analyze the overall performance of the VFDF and to demonstrate its full capabilities and drawbacks, 3D simulations are required.

In the planar jet, a fluid issues from a jet of width D into a co-flowing stream with a lower velocity. The size of the domain in the streamwise (x) and cross-stream (y) directions are $0 \leq x \leq 14D$ and $-3.5D \leq y \leq 3.5D$. The ratio of the co-flowing stream velocity to that of the jet at the inlet is kept fixed at 0.5. A double-hyperbolic tangent profile is utilized to assign the velocity distribution at the inlet plane. The formation of the large scale coherent structures are expedited by imposing low amplitude perturbations at the inlet. In the finite difference simulations, the characteristic boundary condition procedure of Ref. 49 is used at the inlet, free-shear boundary conditions are used at the free-streams and the pressure boundary condition of Ref. 50 is used at the outflow.

The temporal mixing layer consists of two parallel streams traveling in opposite directions with the same speed.[51–53] A hyperbolic tangent profile is utilized to assign the velocity distribution at the initial time. The simulations are conducted for a cubic box, $0 \leq x \leq L$, $-L/2 \leq y \leq L/2$, $0 \leq z \leq L$, where x, y, and z denote the streamwise, the cross-stream and the spanwise directions, respectively; and the length, L is specified such that $L = 2^{N_P}\lambda_u$, where N_P is the

desired number of successive vortex pairings and λ_u is the wavelength of the most unstable mode corresponding to the mean streamwise velocity profile imposed at the initial time. The flowfield is parameterized in a procedure somewhat similar to that by Vreman *et al.*[20] The formation of the large-scale structures are expedited through eigenfunction based initial perturbations.[54,55] This includes two-dimensional[20,52,56] and three-dimensional[52,57] perturbations with a random phase shift between the 3D modes. This results in the formation of two successive vortex pairings and strong three-dimensionality.

The flow variables are normalized with respect to selected reference quantities. In the jet flow, the jet exit velocity, and the jet width are the reference scales. In the temporal mixing layer, the reference length is the half initial vorticity thickness, $L_r=\delta_v(t=0)/2$ ($\delta_v=\Delta U/|\partial\overline{\langle u_1\rangle_L}/\partial y|_{\max}$, where $\overline{\langle u_1\rangle_L}$ is the Reynolds averaged value of the filtered streamwise velocity and ΔU is the velocity difference across the layer). The reference velocity is $U_r=\Delta U/2$.

B. Numerical specifications

All finite difference simulations are conducted on equally spaced grid points with grid spacings $\Delta x=\Delta y=\Delta z$ (for 3D)$=\Delta$. The resolution for LES of the planar jet consists of 201×101 grid points. This allows simulations with a Reynolds number $Re=U_rD/\nu=14{,}000$. The simulations of the temporal mixing layer are conducted on 193^3 and 33^3 points for DNS and LES, respectively. This allows simulations with $Re=U_rL_r/\nu=50$.

To filter the DNS data, a top-hat function[21] of the form below is used

$$G(\mathbf{x}'-\mathbf{x})=\prod_{i=1}^{N_D}\tilde{G}(x_i'-x_i),$$
$$\tilde{G}(x_i'-x_i)=\begin{cases}\dfrac{1}{\Delta_L} & |x_i'-x_i|\leq\dfrac{\Delta_L}{2}\\[2ex] 0 & |x_i'-x_i|>\dfrac{\Delta_L}{2}\end{cases}, \tag{35}$$

in which N_D denotes the number of dimensions, and $\Delta_L=2\Delta$.[58] No attempt is made to investigate the sensitivity of the results to the filter function[24] or the size of the filter.[59]

For VFDF simulations of the temporal mixing layer, the Monte Carlo particles are initially distributed throughout the computational region. For the jet flow, the particles are supplied in the inlet region $-1.75D\leq y\leq 1.75D$. As the particles convect downstream, this zone distorts as it conforms to the flow as determined by the hydrodynamic field. The simulation results are monitored to ensure the particles fully encompass and extend well beyond regions of nonzero vorticity with an approximately uniform particle number density. All simulations are performed with a uniform "weight"[26] of the Monte Carlo particles. In the temporal mixing layer, due to flow periodicity in the streamwise and spanwise directions, if the particle leaves the domain at one of these boundaries new particles are introduced at the other boundary with the same compositional values. In the cross-stream directions, the free-slip boundary condition is satisfied by the mirror-reflection of the particles leaving through these boundaries. In the planar jet, new particles are introduced through the inlet boundary at a rate proportional to the local flow velocity and with a velocity makeup dependent on the cross-stream direction only. When the particles leave the computational domain at the outflow, they are no longer tracked. The density of the Monte Carlo particles is determined by the average number of particles N_E within the ensemble domain of size $\Delta_E\times\Delta_E(\times\Delta_E)$. The effects of both of these parameters are assessed to ensure the consistency and the statistical accuracy of the VFDF simulations.

All results are analyzed both "instantaneously" and "statistically." In the former, the instantaneous contours (snap-shots) and scatter plots of the variables of interest are analyzed. In the latter, the "Reynolds-averaged" statistics constructed from the instantaneous data are considered. In the spatially developing flows this averaging procedure is conducted via sampling in time. In the temporal mixing layer, the statistics are constructed by spatial averaging over the x-z plane of statistical homogeneity. All Reynolds averaged results are denoted by an overbar.

C. Consistency and convergence assessments

The objective of this section is to demonstrate the consistency of the VFDF formulation and the convergence of its Monte Carlo simulation procedure. For this purpose, the results via VFDF and LES-FD are compared against each other. Since the accuracy of the finite difference procedure is well-established (at least for the first-order filtered quantities), such a comparative assessment provides a good means of assessing the performance of the Monte Carlo solution of the VFDF. To do so, the statistical results obtained from the Monte Carlo simulations of Eq. (31) are compared with the finite difference solution of Eqs. (25) and (26). Also, no attempt is made to determine the appropriate values of the model constants; the values suggested in the literature are adopted[34] $C_0=2.1(C_1=4.15)$ and $C_\varepsilon=1$.

In Fig. 1, the instantaneous contour plots of the vorticity are shown as determined by (a) VFDF2 and (b) LES-FD. This figure provides a simple visual demonstration of the consistency of the VFDF2. Scatter plots of $\langle u\rangle_L$ vs $\langle v\rangle_L$ are presented in Fig. 2. The correlation and regression coefficients (denoted, respectively, by ρ and r on these figures) are insensitive to Δ_E. Figures 3 and 4 show the Reynolds averaged values of the streamwise velocity and several components of the SGS stress tensor for several values of Δ_E, with $N_E=40$ kept fixed. It is observed that the first filtered moments as obtained by VFDF agree very well with those via LES-FD even for large Δ_E values. However, smaller Δ_E values are required for convergence of the VFDF predicted SGS stresses to those by LES-FD. The relative difference between the L_2 norms of all of the components of the SGS tensor as a function of $(\Delta_E/\Delta)^2$ is presented in Fig. 5. Extrapolation to $\Delta_E=0$ shows that the "error" goes to zero as $\Delta_E\to0$.

The influence of N_E on the first two moments is shown

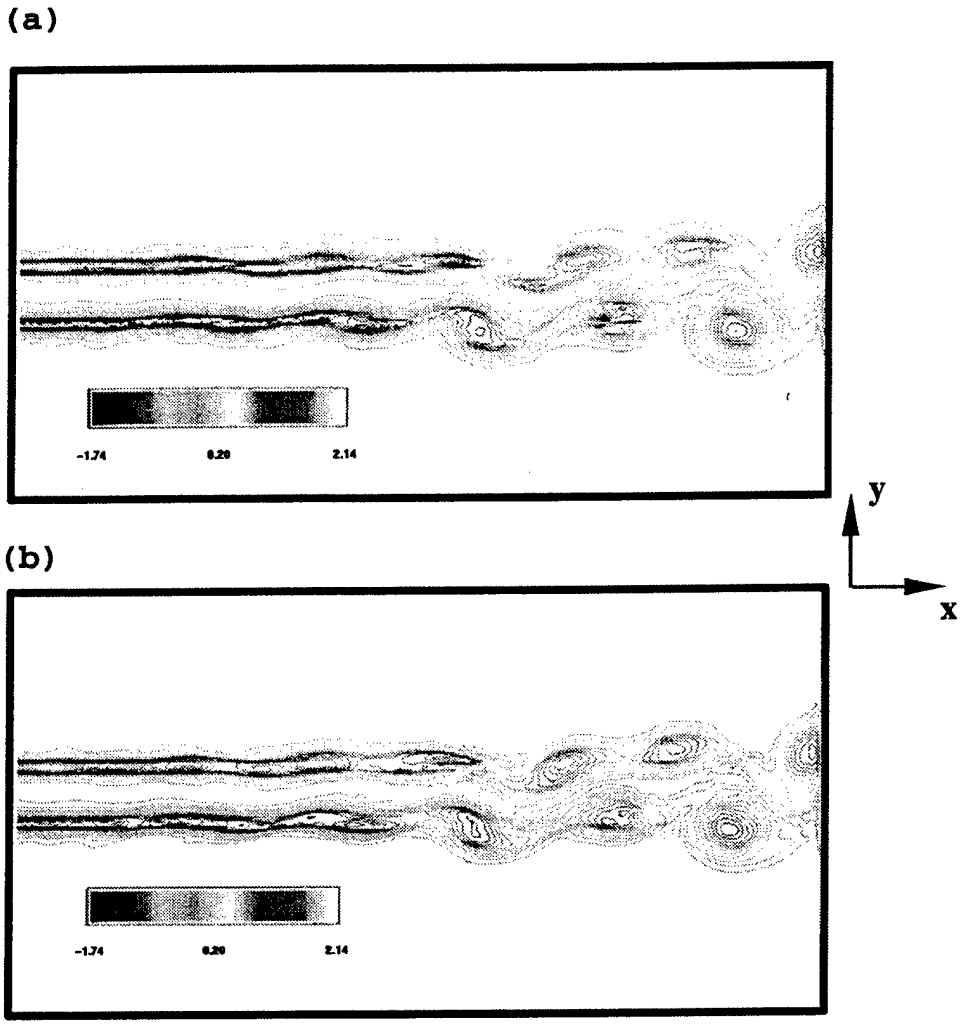

FIG. 1. Plot of the vorticity field contours, (a) VFDF2, (b) LES-FD. $\Delta_E = \Delta$, $N_E = 40$.

in Figs. 6 and 7. It is observed that N_E does not have a significant influence on the first moments, but does slightly influence the second moments. In all the cases considered, $N_E \geq 40$ yields reliable predictions, consistent with previous consistency and convergence assessments of the scalar FDF.[6,8] All the subsequent simulations are conducted with $\Delta_E = \Delta/2$ and $N_E = 40$.

D. Comparative assessments of the VFDF

The objective of this section is to analyze some of the characteristics of the VFDF via comparative assessments against DNS data. This assessment is done via both *a priori* and *a posteriori* analyses. In the former, the DNS results are used to determine the range of the empirical constants appearing in the VFDF sub-closures. In the latter, the final results as predicted by the VFDF are directly compared with those obtained by DNS. The procedure is similar to that in Ref. 20 and considers the 3D temporal mixing layer.

In addition to VFDF, three other LES are conducted with (1) no SGS model, (2) the Smagorinsky[16,60] SGS closure, and (3) the dynamic Smagorinsky[17–19] model. In the case with no model, the contribution of the SGS is completely ignored, i.e., $\tau_L(u_i,u_j)=0$. In this case, the numerical errors amount to an implied model. But as indicated in Ref. 20 this case is included to provide a point of reference for the other closures. The Smagorinsky model is[16,61]

$$\tau_L(u_i,u_j)-\tfrac{2}{3}k\delta_{ij}=-2\nu_t S_{ij},$$

$$S_{ij}=\frac{1}{2}\left(\frac{\partial\langle u_i\rangle_L}{\partial x_j}+\frac{\partial\langle u_j\rangle_L}{\partial x_i}\right), \tag{36}$$

$$\nu_t=C_\nu\Delta_L^2 S.$$

$C_\nu=\sqrt{2}\,0.17^2\approx 0.04$, $S=\sqrt{S_{ij}S_{ij}}$ and Δ_L is the characteristic length of the filter. This model considers the anisotropic part of the SGS stress tensor $a_{ij}=\tau_L(u_i,u_j)-\frac{2}{3}k\delta_{ij}$. The isotropic components are absorbed in the pressure field. The dynamic version of the Smagorinsky model provides a means of approximating C_ν as suggested in Refs. 17–19. The procedure for the implementation of this model in the 3D temporal mixing layer LES is described by Vreman;[20] thus it is not repeated here. (See Refs. 11, 23, 62, and 63 for recent reviews on SGS closure strategy.)

In addition to the resolved velocity field, the primary integral statistical quantities considered for comparative assessments are

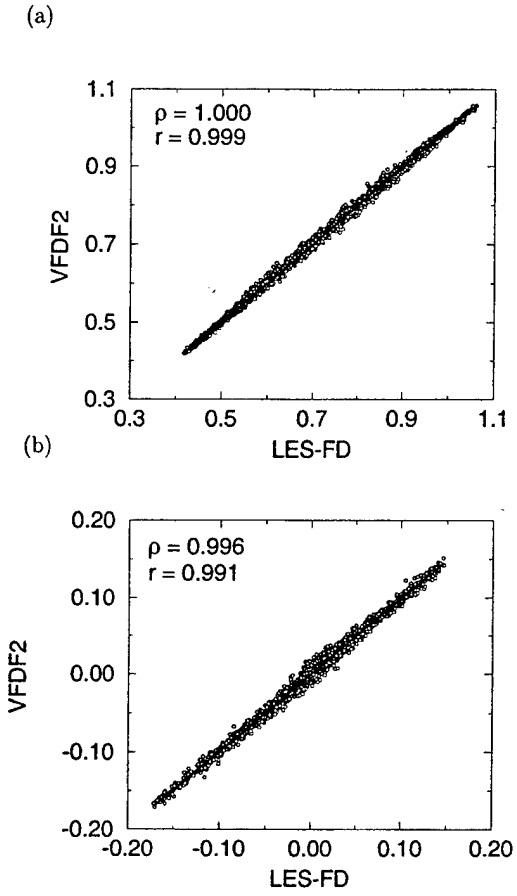

FIG. 2. Scatter plots of the filtered velocity field as obtained via VFDF2 vs LES-FD. (a), $\langle u\rangle_L$; (b), $\langle v\rangle_L$. $\Delta_E=\Delta$, $N_E=40$.

$$E_f=\int \tfrac{1}{2}\langle u_i\rangle_L\langle u_i\rangle_L \mathbf{dx}, \tag{37}$$

$$P_k=\int p_k \mathbf{dx}, \quad \text{with} \quad p_k=-\tau_L(u_i,u_j)\frac{\partial\langle u_i\rangle_L}{\partial x_j},$$

$$E_\nu=\int \varepsilon_\nu \mathbf{dx}, \quad \text{with} \quad \varepsilon_v=\nu\frac{\partial\langle u_i\rangle_L}{\partial x_k}\left(\frac{\partial\langle u_i\rangle_L}{\partial x_k}+\frac{\partial\langle u_k\rangle_L}{\partial x_i}\right), \tag{38}$$

$$B_k=\int \min(0,p_k)\mathbf{dx}.$$

E_f is the kinetic energy of the resolved field, ε_v represents the viscous molecular dissipation rate directly from the filtered field, P_k is the production rate of the SGS kinetic energy (or the rate of energy transfer from the resolved filtered motion to the SGS motion), and B_k is the total backscatter.[64–66] The resolved molecular dissipation rate is always positive (by definition), but the production rate of the SGS kinetic energy can be locally negative. This backscatter is not represented in the Smagorinsky model. The dynamic model is potentially capable of accounting for it, but at the expense of causing numerical instabilities. In the implementation of the dynamic model used here, backscatter is avoided by averaging the numerator and denominator of the expression determining C_v (Refs. 19 and 20) over the homogeneous directions. If negative values are still present, they

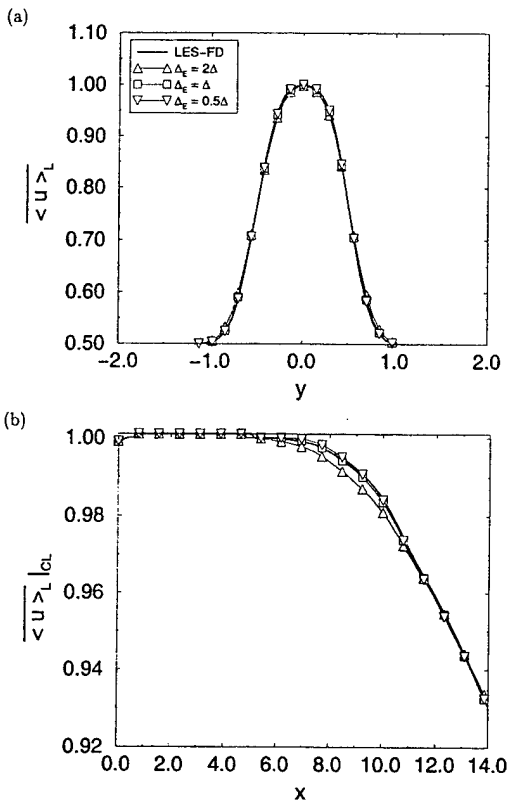

FIG. 3. Reynolds averaged values of the filtered streamwise velocity. (a) Cross-stream variations at $x=7$, (b) streamwise variation at $y=0$ (centerline). $N_E=40$.

are set equal to zero.[20,63] The "resolved" components of the Reynolds-averaged stress tensor are denoted by $\overline{R_{ij}}$ where $R_{ij}=(\langle u_i\rangle_L-\overline{\langle u_i\rangle_L})(\langle u_j\rangle_L-\overline{\langle u_j\rangle_L})$. The "total" Reynolds stresses are denoted by $\overline{r_{ij}}$ where $r_{ij}=(u_i-\overline{u_i})(u_j-\overline{u_j})$. These are approximated by $\overline{r_{ij}}\approx\overline{R_{ij}}+\overline{\tau_L(u_i,u_j)}$.[20,67,68] In DNS, the total stresses are evaluated directly and the results indicate that $\overline{R_{ij}}+\overline{\tau_L(u_i,u_j)}$ does indeed approximate $\overline{r_{ij}}$ with a maximum error of less than 10%.

Figure 8 shows the distribution of the particle number density within the whole computational domain. Assuring an approximately uniform distribution, the values of the moments within local ensembles are compared with those of filtered DNS data. These DNS data are transposed from the original high resolution 193^3 points to the low resolution of 33^3 points, and then are compared with LES results on these coarse points.

The DNS data are also used to make *a priori* estimates of the model constants. The primary terms which require closure are the SGS dissipation and the velocity-pressure scrambling tensors. The model equation [Eq. (20)] involving C_ε is in a scalar form. For an estimate of C_1 (thus C_0), we consider the following norm of the corresponding closure [Eq. (27)]

$$\|-\Pi_{ij}-(\varepsilon_{ij}-\tfrac{2}{3}\varepsilon\delta_{ij})\|\approx C_1\omega\|\tau_L(u_i,u_j)-\tfrac{2}{3}k\delta_{ij}\|, \tag{39}$$

where $\|W_{ij}\|=\sqrt{W_{ji}W_{ij}}$. To estimate the coefficients, a linear regression is performed on all the data points at each computational time step. The optimized constants as obtained in this way are denoted by $\tilde{C}_\varepsilon$ and $\tilde{C}_1$. This procedure is also

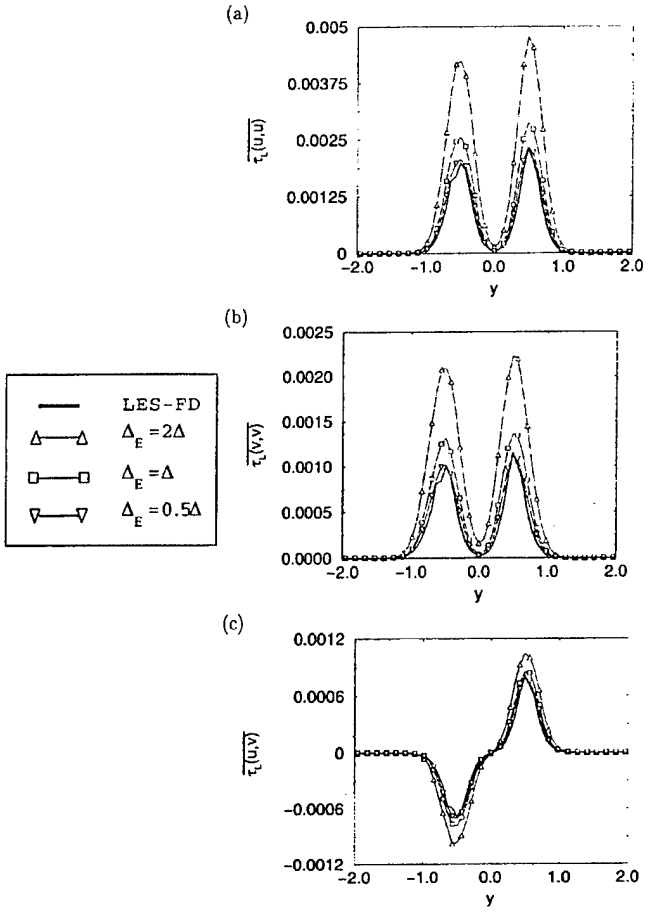

FIG. 4. Cross-stream variations of the Reynolds averaged values of some of the components of the SGS stress tensor at $x=7$ with $N_E=40$. The LES-FD results are obtained with $\Delta_E=0.5\Delta$, $N_E=40$.

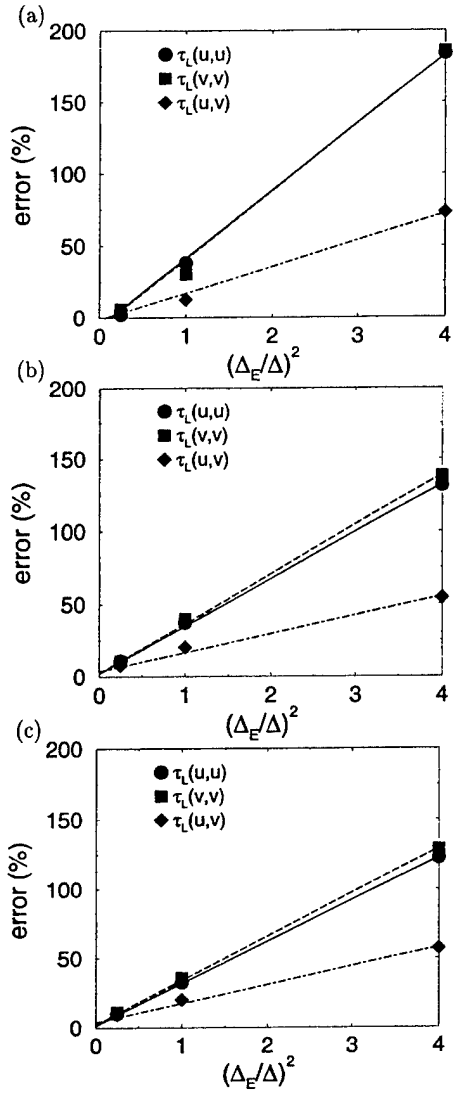

FIG. 5. Percentage of the relative difference between the L_2 norms of the stresses as a function of Δ_E/Δ. (a) $x=2.8$, (b) $x=7$, (c) $x=11.2$.

followed for the Reynolds averaged data, with the optimized models obtained in this way denoted by $\overline{C_\varepsilon}$ and $\overline{C_1}$. The temporal variations of these estimated values are shown in Fig. 9. The nonuniformity of the coefficients indicates the "nonuniversality" of the models. This is expected as the flow evolves from an initially smooth laminar state to a strong three-dimensional state (at $t\approx 40$) before the action of the small scales becomes significant. The closures as adopted are not fully suitable for application in all of these flow regions. Nevertheless, Fig. 9 indicates that the values for these coefficients as suggested in RAS, i.e., $C_1\approx 4.15, C_\varepsilon\approx 1$ are reasonable, at least within the turbulent regime. The influences of these parameters are further investigated via *a posteriori* analysis of the results as discussed below.

Figures 10 and 11 show the contours of the spanwise and the streamwise components of the vorticity field, respectively, at time $t=80$. By this time, the flow has gone through several pairings and exhibits strong 3D effects. This is evident by the formation of large scale spanwise rollers with presence of counter-rotating streamwise vortex pairs in all the simulations. The results via the no-model indicate too many small-scale structures which clearly are not captured accurately on the coarse grid. The amount of SGS diffusion with the Smagorinsky model is very significant at initial times. Due to this dissipative characteristics of the model, the predicted results are too smooth and only contain the large scale structures. The vortical structures as depicted by the dynamic Smagorinsky and the VFDF are very similar and predict the DNS results better than the other two models. The results obtained by VFDF1 and VFDF2 are virtually indistinguishable from each other. This is expected, due to the lack of importance of molecular effects in this free shear flow.

The Reynolds averaged values of the streamwise velocity and the temporal variations of the momentum thickness

$$\delta_m(t)\,\frac{1}{4}=\int_{-L/2}^{L/2}(1-\overline{\langle u\rangle_L})(1+\overline{\langle u\rangle_L})dy, \tag{40}$$

are shown in Figs. 12 and 13, respectively. In Fig. 12 the Reynolds averaged values of both filtered and unfiltered DNS data are considered and are shown to be essentially equivalent. Therefore, the latter are not shown in subsequent figures. The dissipative nature of the Smagorinsky model at initial times resulting in a slow growth of the layer is shown. Several values of the model parameters (C_0, C_ε) are consid-

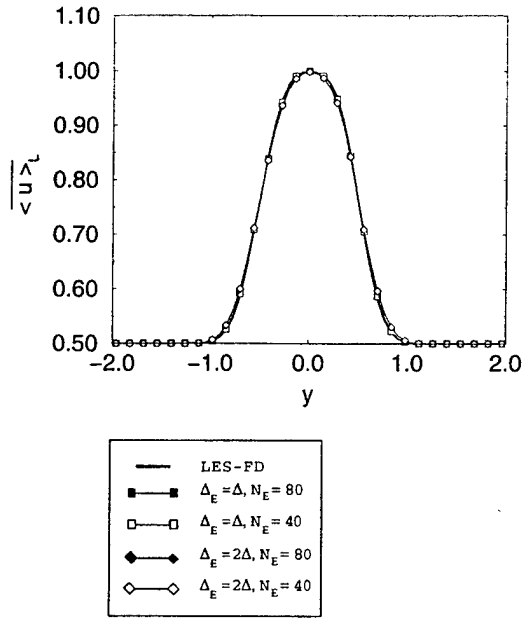

FIG. 6. Cross-stream variations of the Reynolds averaged values of the filtered streamwise velocity at $x=7$. The LES-FD results are obtained with $\Delta_E=0.5\Delta$, $N_E=40$.

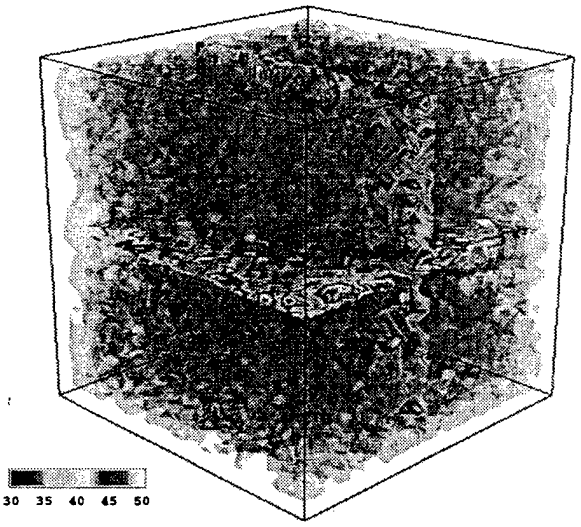

FIG. 8. Particle number density in VFDF2 simulation at $t=60$. The isosurface corresponds to $N_E=40$ set as initial conditions. $C_0=2.1$, $C_\varepsilon=1$.

ered in the VFDF simulations. It is observed that as the magnitude of C_ε decreases, the initial rate of the layer's spread is higher. With the exception of the case with $C_\varepsilon=0.5$ and the Smagorinsky model, all the other VFDF cases, the dynamic Smagorinsky and the no-model yield a similar rate of layer's growth at late times.

The temporal variations of the resolved kinetic energy and all of the terms defined in Eq. (38) are shown in Fig. 14.

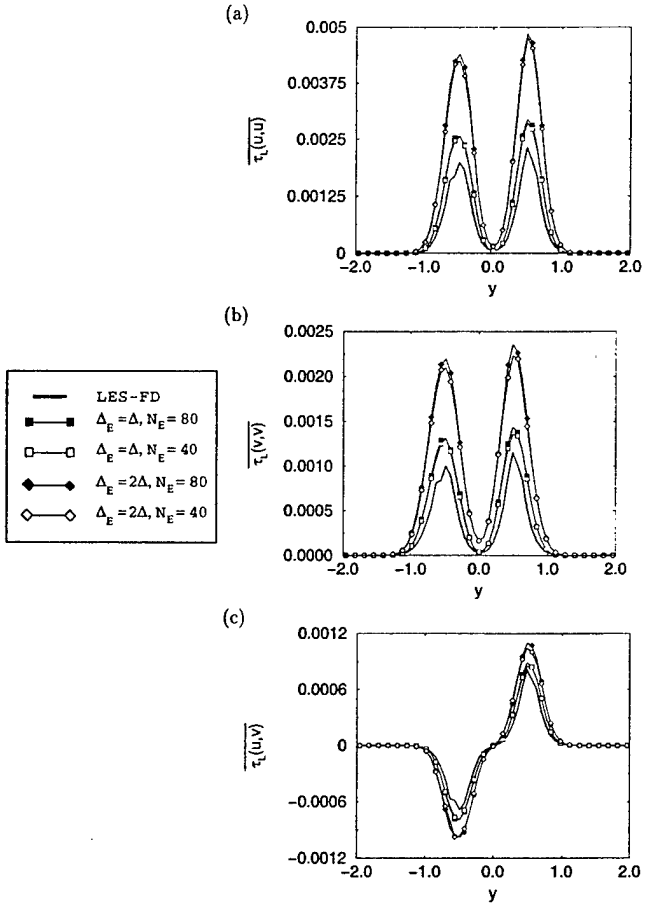

FIG. 7. Cross-stream variations of the Reynolds averaged values of some of the components of the SGS stress tensor at $x=7$. The LES-FD results are obtained with $\Delta_E=0.5\Delta$, $N_E=40$.

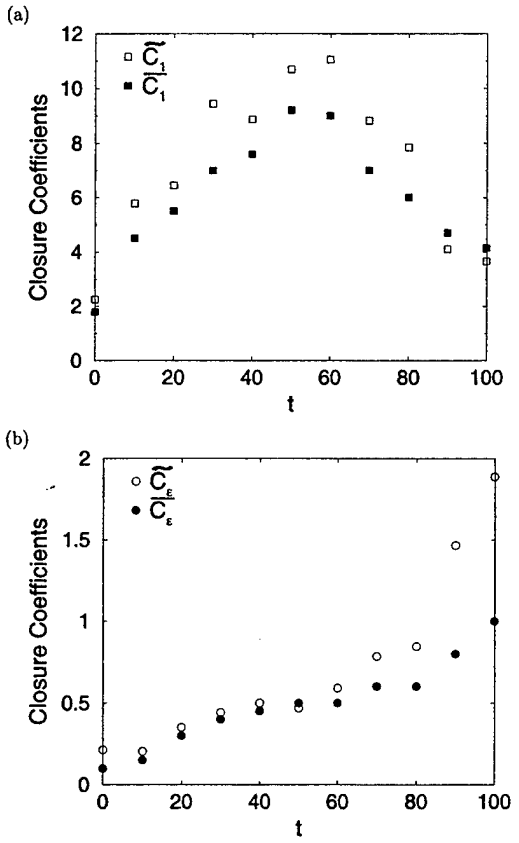

FIG. 9. Time variation of the model coefficients as obtained from *a priori* analysis of the DNS data.

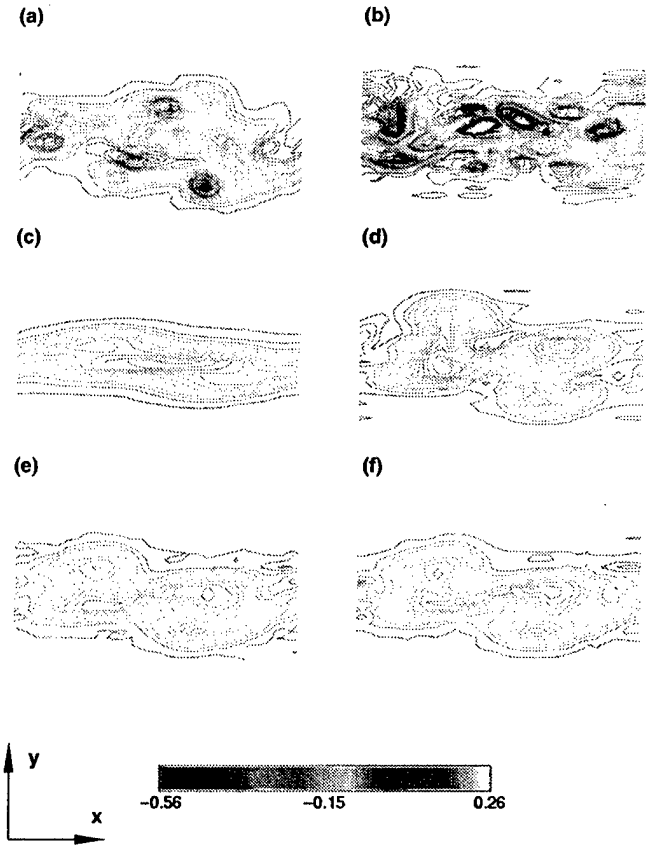

FIG. 10. Contour plots of the spanwise component of the vorticity at $z=0.75L/L_r$, $t=80$. (a) Filtered DNS, (b) no model, (c), Smagorinsky model, (d) dynamic Smagorinsky model, (e) VFDF2, $C_0=2.1$, $C_\varepsilon=1$, (f) VFDF1, $C_0=2.1$, $C_\varepsilon=1$.

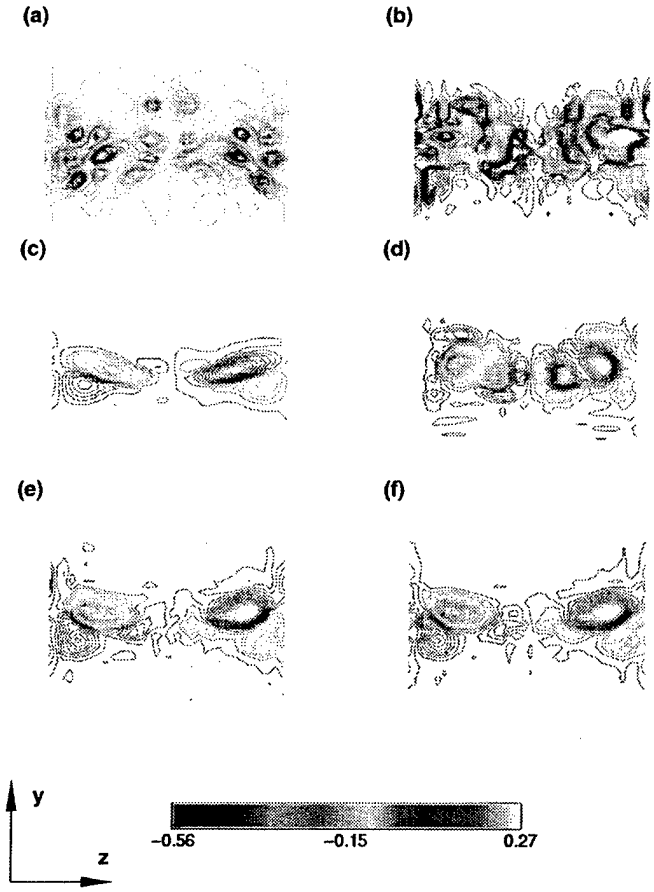

FIG. 11. Contour plots of the streamwise component of the vorticity vector at $x=0.25L/L_r$, $t=80$. (a) Filtered DNS, (b) no model, (c) Smagorinsky model, (d) dynamic Smagorinsky model, (e) VFDF2, $C_0=2.1$, $C_\varepsilon=1$, (f) VFDF1, $C_0=2.1$, $C_\varepsilon=1$.

The overall features displayed in this figure are similar to those reported by Vreman *et al.*[20] for the no model, the Smagorinsky model and the dynamic Smagorinsky model. The initial rate of decay of the resolved kinetic energy for the Smagorinsky model is the highest. This is due to the excessive production of the SGS kinetic energy by this model in the transitional region, and explains the reason for the lack of small scales in the vortical structures as discussed before. For all the other models the initial rate of decrease of the resolved kinetic energy is small and increases as the flow develops. The trend portrayed by DNS results is best captured by the VFDF simulations. For the no model case the only means of dissipation of the resolved kinetic energy is through molecular action and numerical dissipation which become significant at later stages due to presence of a large amount of small scales. In this case, the amount of numerical dissipation is the highest. For all the other closures, the productions rate of the SGS kinetic energy is larger than the molecular dissipation as the flow develops. The dynamic Smagorinsky and the no-model simulations predict the same initial rate of decay for the resolved kinetic energy. This is due to low initial values of P_k predicted by the dynamic Smagorinsky model. After $t=40$ the amount of P_k as predicted by the dynamic model is more than that of molecular dissipation by the no-model. Thus the rate of decay of the resolved kinetic energy becomes higher for the dynamic model and is closer to that obtained by DNS.

With the exception of the no-model case, all the simulations predict similar trends for the molecular dissipation. The magnitude of this dissipation as predicted by VFDF changes slightly with the variation of the model parameter. The production rate of the SGS kinetic energy depends more strongly on the model coefficients; as C_ε decreases, the peak

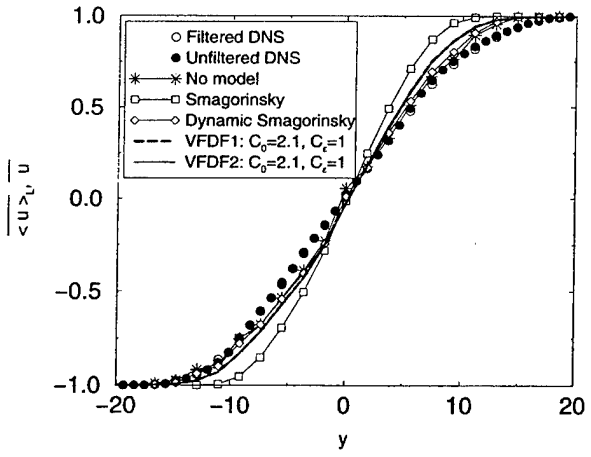

FIG. 12. Cross-stream variations of the Reynolds averaged values of the streamwise velocity at $t=70$.

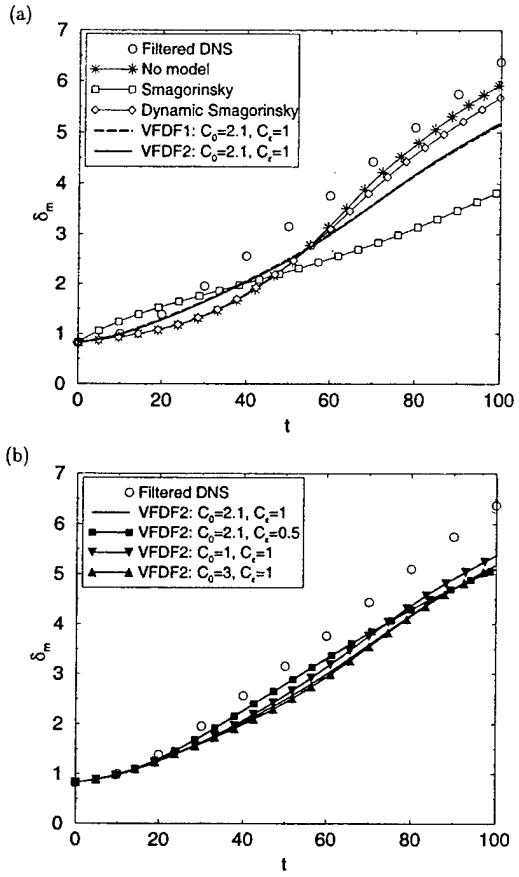

FIG. 13. Temporal variations of the momentum thickness.

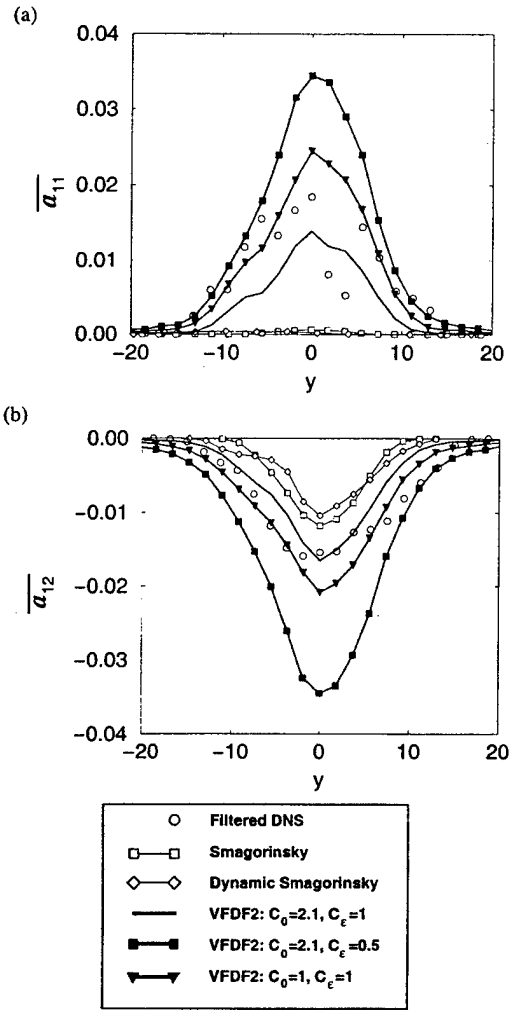

FIG. 15. Cross-stream variations of some of the components of $\overline{a_{ij}}$ at $t = 60$.

magnitude of P_k is larger. The Smagorinsky model does not adequately predict P_k, and the dynamic model yields better predictions at long times. The overall trends are best predicted by VFDF. The same is true in capturing the backscatter phenomenon. By design, the backscatter is identically zero in the Smagorinsky and the dynamic Smagorinsky model. But VFDF is capable of capturing it, and its extent is controlled by the model parameters. In this regard it is important to note that there are no numerical instability problems in the VFDF solver for negative B_k values. However, the amount of predicted backscatter is less than that of

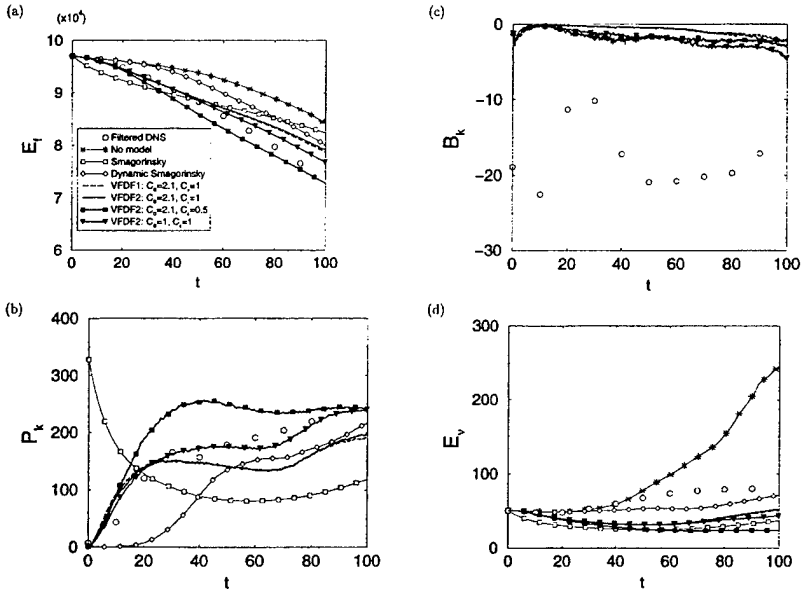

FIG. 14. Temporal variations of (a) total resolved kinetic energy, (b) SGS kinetic energy production rate, (c) total backscatter, (d) total resolved dissipation.

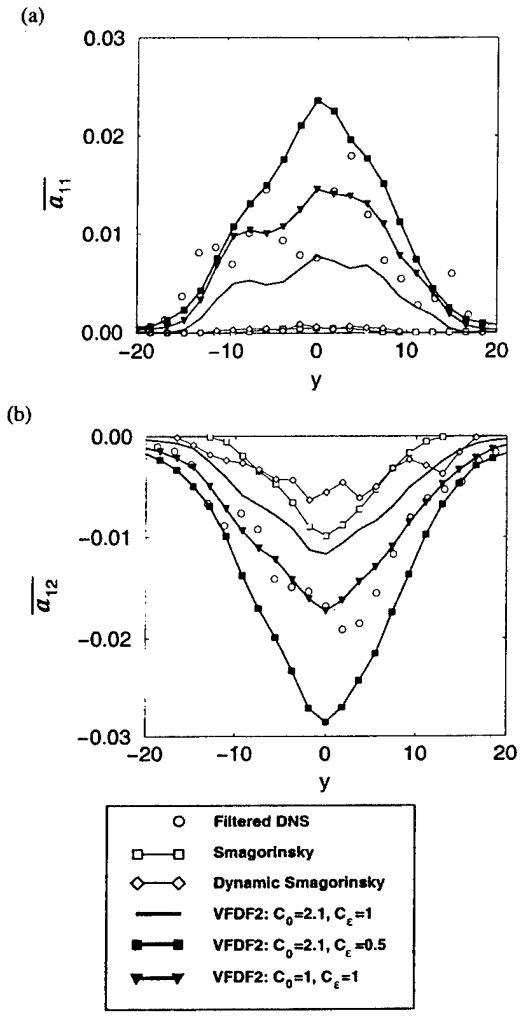

FIG. 16. Cross-stream variations of some of the components of $\overline{a_{ij}}$ at $t=80$.

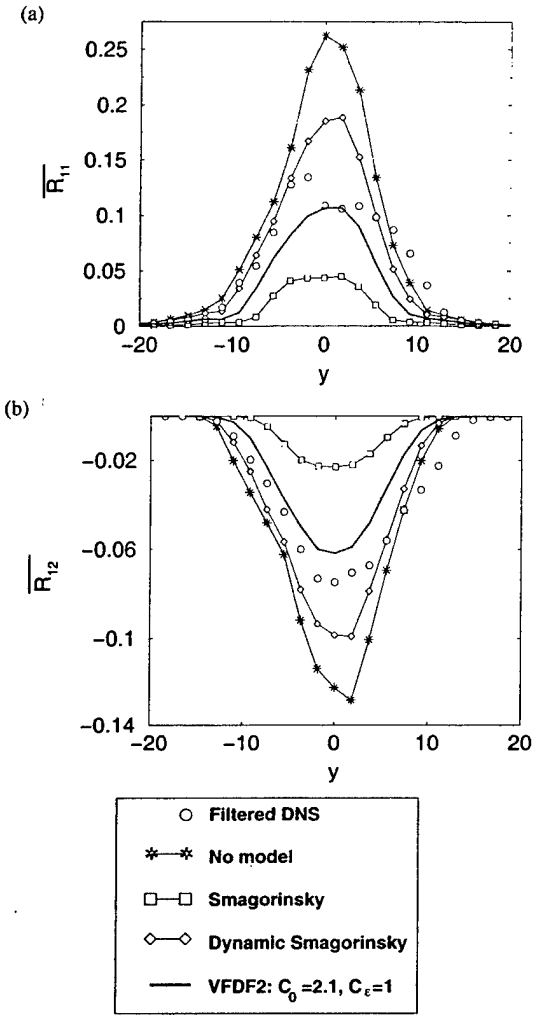

FIG. 17. Cross-stream variations of some of the components of $\overline{R_{ij}}$ at $t=60$.

DNS and its relative magnitude is less than those of P_k and E_v.

Several components of the planar averaged values of the SGS anisotropy tensor, $\overline{a_{ij}}=\overline{\tau_L(u_i,u_j)}-\frac{2}{3}\overline{k}\delta_{ij}$ are presented in Figs. 15 and 16. Both the Smagorinsky and the dynamic model under-predict the components of this stress. The VFDF predictions are more satisfactory. In this regard, the VFDF is expected to be more effective than the other closures for LES of reacting flows since the extent of SGS mixing is influenced by SGS convection.[69,70] "Optimum" values for C_ε and C_0 cannot be suggested to predict all of the components of this tensor at all times, but it is obvious that there is too much SGS energy with $C_\varepsilon=0.5$.

Several components of the resolved stress tensor $\overline{R_{ij}}$ are shown in Figs. 17 and 18. As expected, the performance of the Smagorinsky model is not very good as it does not predict the spread and the peak value of the resolved Reynolds stresses. None of the other models show a distinct superiority in predicting the DNS results. The no-model and the dynamic Smagorinsky model predict large peak values at the middle of the layer. The VFDF predicts both the spread and the peak values reasonably well. The results for small C_ε values are not shown since the amount of energy in the resolved scale decreases too much in favor of the increase of the SGS stress (as shown in Figs. 15 and 16). The cross-stream variations of the total Reynolds stress $\overline{r_{12}}$ are presented in Fig. 19. The peak values by the no-model simulations are again the highest. The dynamic model and VFDF perform similarly and capture the DNS trends equally well.

E. Comparison with previous investigations

All of the results obtained here by DNS, and LES via the Smagorinsky and the dynamic Smagorinsky models agree very well with those of Vreman *et al.*[20] The slight differences are due to the nonidentical flow initializations, and the different computational methodologies employed in the two simulations. To compare with results of other investigations, simulations are conducted of another temporally developing mixing layer with $Re=500$ in a larger computational domain, $L_r=120$. An initial forcing of the form $\mathcal{A}e^{-(y/2)^2}$ is used, where $\mathcal{A}$ is a uniformly distributed random number with an amplitude of 0.05. Rogers and Moser[60] perform DNS of a high Re number flow on $512\times210\times192$ spectral points. The results of these simulations are in excellent agreements with laboratory data of Bell and Mehta.[71] Here, LES is con

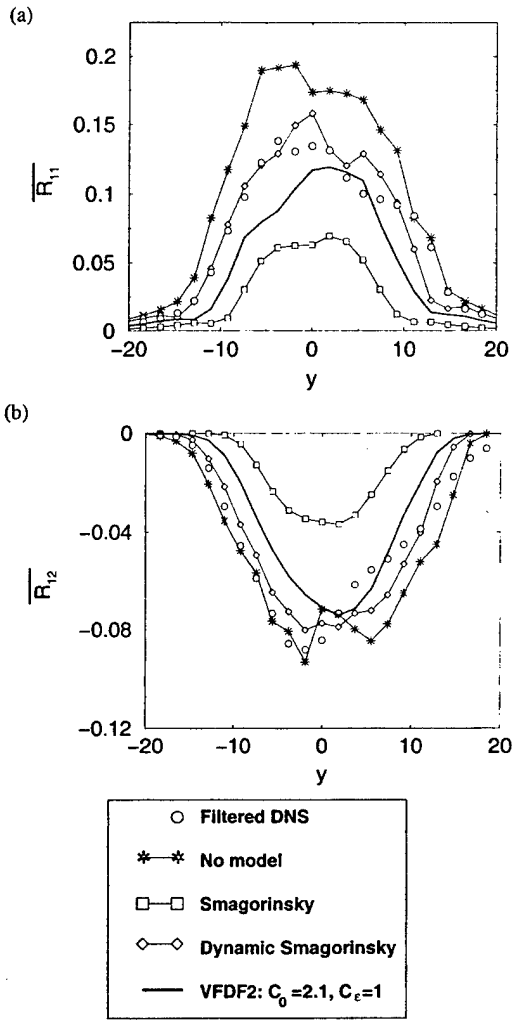

FIG. 18. Cross-stream variations of some of the components of $\overline{R_{ij}}$ at $t=80$.

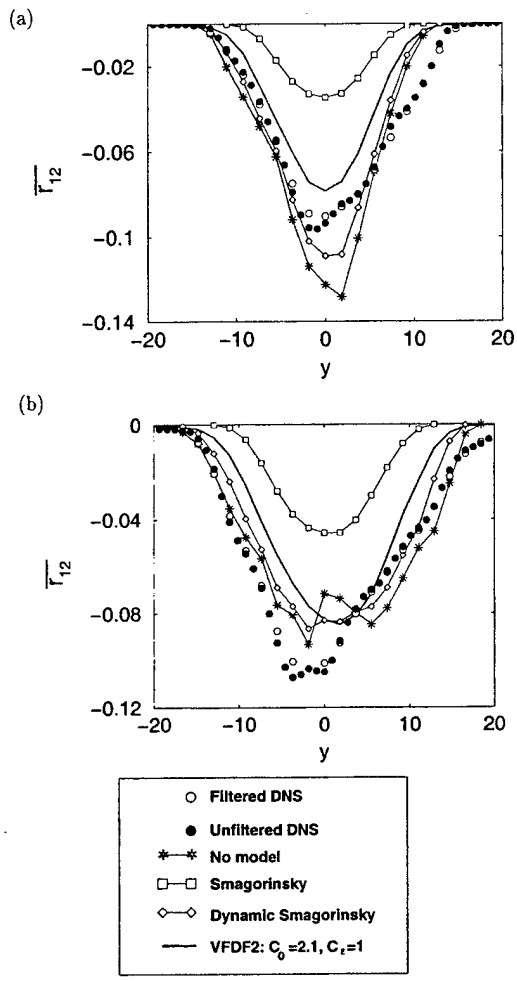

FIG. 19. Cross-stream variations of $\overline{r_{12}}$, (a) $t=60$, (b) $t=80$.

ducted of this flow via the dynamic Smagorinsky model.

The profiles of the mean streamwise velocity and several components of the resolved stresses at $t=250$ are presented in Figs. 20 and 21, respectively. In these figures, $\xi = y/\delta_m(t)$ and the symbols denote the experimental data[71] at several streamwise locations. The good agreement with these data also indicates good agreement with DNS results of Rogers and Moser.[72]

F. Computational requirements

The total computational times associated with simulations of the 3D temporal mixing layer are shown in Table II. Expectedly, the overhead associated with the VFDF simulation is extensive as compared to the other models; nevertheless this requirement is significantly less that of DNS. This overhead was tolerated in present simulations, but can be reduced with utilization of an optimum parallel simulation procedure. This has been discussed for use in PDF[73] and is recommended for future VFDF simulations.

VII. SUMMARY AND CONCLUDING REMARKS

The filtered density function (FDF) methodology[1] has proven very effective for large eddy simulation (LES) of turbulent reacting flows.[3,6–11] In all previous contributions, the LES/FDF of only the scalar quantities are considered. The objective of the present work is to develop the FDF methodology for LES of the velocity field. For this purpose, a methodology termed the velocity filtered density function

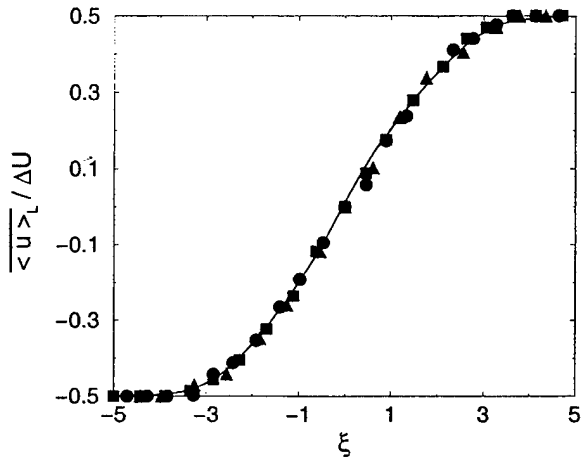

FIG. 20. Cross-stream variation of the Reynolds averaged values of the streamwise velocity at $t=250$. Solid line denotes model predictions via the dynamic Smagorinsky model. Symbols denote experimental data of Bell and Mehta (Ref. 71).

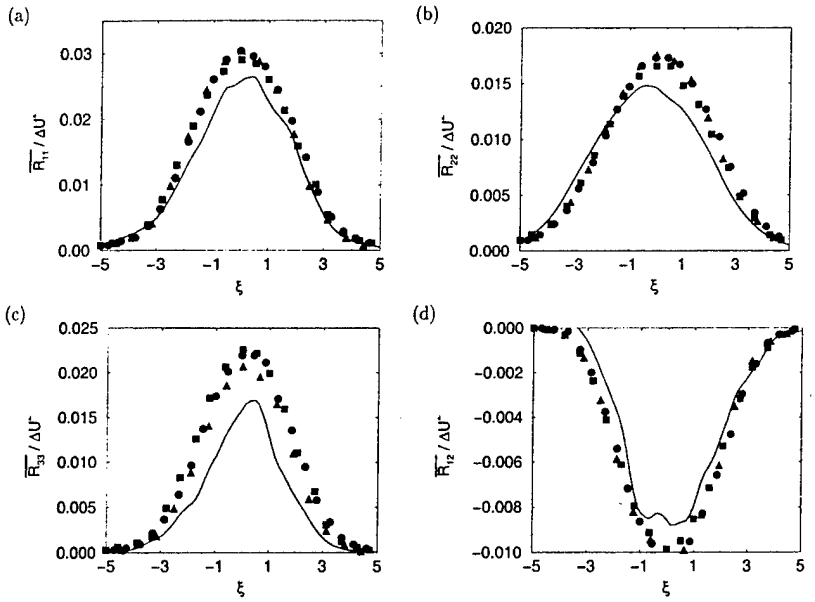

FIG. 21. Cross-stream variations of the Reynolds averaged values of the streamwise velocity at $t=250$. Solid lines denote model predictions via the dynamic Smagorinsky model. Symbols denote experimental data of Bell and Mehta (Ref. 71).

(VFDF) is developed. The VFDF is basically the probability function (PDF) of the subgrid scale (SGS) velocity vector. The exact transport equation governing the evolution of the VFDF is derived. It is shown that the effects of SGS convection in this equation appears in a closed form. The unclosed terms in this transport equation are modeled via two formulations: VFDF1 and VFDF2. The primary difference between the two models is the inclusion of the molecular diffusion in the spatial transport of the VFDF in the first formulation. The closure strategy in the formulation similar to that in PDF methods in Reynolds averaged simulation (RAS) procedures.[32] In this way, the VFDF formulation is at least equivalent to a second-order moment SGS closure.

The modeled VFDF transport equations are solved numerically via a Lagrangian Monte Carlo scheme in which the solutions of the equivalent stochastic differential equations (SDEs) are obtained. Two Monte Carlo procedures are considered. The schemes preserve the Itô–Gikhman nature of the SDEs and provide a reliable solution for the VFDF. The consistency of the VFDF formulation and the convergence of its Monte Carlo solutions are assessed. This is done via comparisons between the results obtained by the Monte Carlo procedure and the finite difference solution of the transport equations of the first two filtered moments of VFDF (LES-FD). With inclusion of the third moments from the VFDF into the LES-FD, the consistency and convergence of the Monte Carlo solution is demonstrated by good agreements of the first two SGS moments with those obtained by LES-FD.

TABLE II. Computer requirements for the 3D temporal mixing layer. One unit corresponds to 1657.2 seconds of CPU time on the SGI origin 2000.

	Resolution	N_E	Normalized CPU time
DNS	193×193×193	···	178
VFDF1	33×33×33	40	33.6
VFDF2	33×33×33	40	30
Dynamic Smagorinsky	33×33×33	···	2.19
Smagorinsky	33×33×33	···	1.05
No model	33×33×33	···	1

The VFDF predictions are compared with those with LES results with no SGS model, with the Smagorinsky[16] SGS closure, and with the dynamic Smagorinsky[17–19] model. All of these results are also compared with direct numerical simulation (DNS) results of a three-dimensional, temporally developing mixing layer in a context similar to that conducted by Vreman *et al.*[20] This comparison provides a means of examining some of the trends and overall characteristics as predicted by LES. It is shown that the VFDF performs well in predicting some of the phenomena pertaining to the SGS transport. The magnitude of the SGS Reynolds stresses as predicted by VFDF is larger than those predicted by the other SGS models and much closer to the filtered DNS results. The temporal evolution of the production rate of the SGS kinetic energy is predicted well by VFDF as compared with those via the other closures. The VFDF is also capable of accounting the SGS backscatter without any numerical instability problems, although the level predicted is substantially less than that observed in DNS.

The results of *a priori* assessment against DNS data indicates that the values of the model coefficients as employed in VFDF (C_0 and C_ε) are of the range suggested in the equivalent models previously used in RAS. The results of *a posteriori* assessments via comparison with DNS data does not give any compelling reasons to use values other than those suggested in RAS, $C_0=2.1$, $C_\varepsilon=1$. However, small values of C_ε are not acceptable as they would yield too much of SGS energy relative to that within the resolved scales.

Most of the overall flow features, including the mean velocity field and the resolved and total Reynolds stresses as predicted by VFDF are similar to those obtained via the dynamic Smagorinsky model. This is interesting in view of the fact that the model coefficients in VFDF are kept fixed. It may be possible to improve the predictive capabilities of the VFDF by two ways: (1) Development of a dynamic proce-

dure to determine the model coefficients, and/or (2) implementation of higher order closures for the generalized Langevin model parameter G_{ij} (see Ref. 34).

Work is in progress towards developments of a joint velocity-scalar FDF for LES of reacting flows. Compared to standard LES, this approach has the advantage of treating reaction in a closed form; and, compared to scalar FDF[6,8] has the advantage of treating convective transport (of momentum and species) in closed form. These modeling advantages have an associated computational penalty. For the cases considered here, VFDF is more expensive computationally than the dynamic Smagorinsky model by a factor of 15. It is expected that VFDF will not be more expensive than scalar FDF, at least for reacting flows with many species.

ACKNOWLEDGMENTS

We are indebted to Dr. A. W. Cook, Dr. T. D. Dreeben, Dr. M. Germano, Dr. S. Heinz, Dr. R. D. Moser, Dr. M. M. Rogers, Dr. P. Sagaut, and Dr. B. Vreman for their comments and very useful suggestions on the first draft of this paper. This work is sponsored by the U.S. Air Force Office of Scientific Research under Grant No. F49620-00-1-0035 to SUNY-Buffalo and Grant No. F49620-00-1-0171 to Cornell University. Dr. Julian M. Tishkoff is the Program Manager for both these grants. Additional support for the work at SUNY-Buffalo is provided by the NASA Langley Research Center under Grant No. NAG-1-2238 with Dr. J. Philip Drummond as the Technical Monitor. Computational resources are provided by the NCSA at the University of Illinois at Urbana and by the CCR at SUNY-Buffalo.

[1]S. B. Pope, "Computations of turbulent combustion: Progress and challenges," Proc. Combust. Inst. **23**, 591 (1990).

[2]C. K. Madnia and P. Givi, "Direct numerical simulation and large eddy simulation of reacting homogeneous turbulence," in *Large Eddy Simulations of Complex Engineering and Geophysical Flows*, edited by B. Galperin and S. A. Orszag (Cambridge University Press, Cambridge, UK, 1993), pp. 315–346.

[3]F. Gao and E. E. O'Brien, "A large-eddy simulation scheme for turbulent reacting flows," Phys. Fluids A **5**, 1282 (1993).

[4]S. H. Frankel, V. Adumitroaie, C. K. Madnia, and P. Givi, "Large eddy simulations of turbulent reacting flows by assumed PDF methods," Engineering Applications of Large Eddy Simulations **162**, 81 (1993).

[5]A. W. Cook and J. J. Riley, "A subgrid model for equilibrium chemistry in turbulent flows," Phys. Fluids **6**, 2868 (1994).

[6]P. J. Colucci, F. A. Jaberi, P. Givi, and S. B. Pope, "Filtered density function for large eddy simulation of turbulent reacting flows," Phys. Fluids **10**, 499 (1998).

[7]J. Réveillon and L. Vervisch, "Subgrid scale turbulent micromixing: Dynamic approach," AIAA J. **36**, 336 (1998).

[8]F. A. Jaberi, P. J. Colucci, S. James, P. Givi, and S. B. Pope, "Filtered mass density function for large eddy simulation of turbulent reacting flows," J. Fluid Mech. **401**, 85 (1999).

[9]S. C. Garrick, F. A. Jaberi, and P. Givi, "Large eddy simulation of scalar transport in a turbulent jet flow," in *Recent Advances in DNS and LES, Fluid Mechanics and its Applications*, edited by D. Knight and L. Sakell (Kluwer Academic, Dordrecht, 1999), Vol. 54, pp. 155–166.

[10]S. James and F. A. Jaberi, "Large scale simulations of two-dimensional nonpremixed methane jet flames," Combust. Flame **123**, 465 (2000).

[11]S. B. Pope, *Turbulent Flows* (Cambridge University Press, Cambridge, UK, 2000).

[12]X. Y. Zhou and J. C. F. Pereira, "Large eddy simulation (2D) of a reacting plan mixing layer using filtered density function," Flow, Turbul. Combust. **64**, 279 (2000).

[13]K. H. Luo, "DNS and LES of turbulence-combustion interactions," in Ref. 22, Chap. 14, pp. 263–293.

[14]T. Poinsot and D. Veynante, *Theoretical and Numerical Combustion* (R. T. Edwards, Philadelphia, 2001).

[15]C. Tong, "Measurements of conserved scalar filtered density function in a turbulent jet," Phys. Fluids **13**, 2923 (2001).

[16]J. Smagorinsky, "General circulation experiments with the primitive equations. I. The basic experiment," Mon. Weather Rev. **91**(3), 99 (1963).

[17]M. Germano, U. Piomelli, P. Moin, and W. H. Cabot, "A dynamic subgrid-scale eddy viscosity model," Phys. Fluids A **3**, 1760 (1991).

[18]M. Germano, "Turbulence: The filtering approach," J. Fluid Mech. **238**, 325 (1992).

[19]D. K. Lilly, "A proposed modification of the Germano sub-grid closure method," Phys. Fluids A **4**, 633 (1992).

[20]B. Vreman, B. Geurts, and H. Kuerten, "Large-eddy simulation of the turbulent mixing layer," J. Fluid Mech. **339**, 357 (1997).

[21]A. A. Aldama, *Filtering Techniques for Turbulent Flow Simulations, Lecture Notes in Engineering, Vol. 49* (Springer-Verlag, New York, 1990).

[22]*Modern Simulation Strategies for Turbulent Flow*, edited by B. J. Geurts (R. T. Edwards, Philadelphia, 2001).

[23]P. Sagaut, *Large Eddy Simulation for Incompressible Flows* (Springer, New York, 2001).

[24]B. Vreman, B. Geurts, and H. Kuerten, "Realizability conditions for the turbulent stress tensor in large-eddy simulation," J. Fluid Mech. **278**, 351 (1994).

[25]E. E. O'Brien, "The probability density function (PDF) approach to reacting turbulent flows," in *Turbulent Reacting Flows*, edited by P. A. Libby and F. A. Williams (Springer-Verlag, Heidelberg, 1980), Chap. 5, pp. 185–218.

[26]S. B. Pope, "PDF methods for turbulent reacting flows," Prog. Energy Combust. Sci. **11**, 119 (1985).

[27]D. C. Haworth and S. B. Pope, "A generalized Langevin model for turbulent flows," Phys. Fluids **29**, 387 (1986).

[28]D. C. Haworth and S. B. Pope, "A PDF modeling study of self-similar turbulent free shear flows," Phys. Fluids **30**, 1026 (1987).

[29]T. D. Dreeben and S. B. Pope, "Probability density function and Reynolds-stress modeling of near-wall turbulent flows," Phys. Fluids **9**, 154 (1997).

[30]T. D. Dreeben and S. B. Pope, "Wall-function treatment in PDF methods for turbulent flows," Phys. Fluids **9**, 2692 (1997).

[31]T. D. Dreeben and S. B. Pope, "Probability density function/Monte Carlo simulation of near-wall turbulent flows," J. Fluid Mech. **357**, 141 (1998).

[32]S. B. Pope, "Lagrangian PDF methods for turbulent flows," Annu. Rev. Fluid Mech. **26**, 23 (1994).

[33]J. Rotta, "Statistiche theorie nichthomogener turbulenz," J. Zeitsch fur Physik **129**, 547 (1951) [translation in English available in NASA TM-14560 (1982)].

[34]S. B. Pope, "On the relationship between stochastic Lagrangian models of turbulence and second-moment closures," Phys. Fluids **6**, 973 (1994).

[35]J. W. Deardorff, "The use of subgrid transport equations in a three-dimensional model of atmospheric turbulence," J. Fluids Eng. **95**, 429 (1973).

[36]H. Risken, *The Fokker–Planck Equation, Methods of Solution and Applications* (Springer, New York, 1989).

[37]C. W. Gardiner, *Handbook of Stochastic Methods* (Springer-Verlag, New York, 1990).

[38]S. Karlin and H. M. Taylor, *A Second Course in Stochastic Processes* (Academic, New York, 1981).

[39]S. B. Pope, "Mean field equations in PDF particle methods for turbulent reactive flows," Technical Report FDA 97-06, Sibley School of Mechanical and Aerospace Engineering, Cornell University, Ithaca, NY, 1997.

[40]M. Muradoglu, P. Jenny, S. B. Pope, and D. A. Caughey, "A consistent hybrid-volume/particle method for the PDF equations of turbulent reactive flows," J. Comput. Phys. **154**, 342 (1999).

[41]M. Muradoglu, S. B. Pope, and D. A. Caughey, "The hybrid method for the PDF equations of turbulent reactive flows: Consistency conditions and correction algorithms," J. Comput. Phys. **172**, 841 (2001).

[42]P. E. Kloeden and E. Platen, *Numerical Solution of Stochastic Differential Equations, Applications of Mathematical Stochastic Modelling and Ap-*

plied Probability, Vol. 23 (Springer-Verlag, New York, 1995).
[43]P. Billingsly, *Probability and Measure* (Wiley, New York, 1979).
[44]D. T. Gillespie, *Markov Processes, An Introduction for Physical Scientists* (Academic, New York, 1992).
[45]K. Itô, *Differential Equations, Memoirs of the American Mathematical Society, Vol. 4* (American Mathematical Society, Providence, RI, 1951).
[46]I. I. Gikhman and A. V. Skorokhod, *Stochastic Differential Equations* (Academic, New York, 1972).
[47]M. H. Carpenter, "A high-order compact numerical algorithm for supersonic flows," in *Proceedings of the 12th International Conference on Numerical Methods in Fluid Dynamics, Lecture Notes in Physics*, edited by K. W. Mortron (Springer-Verlag, Berlin, 1990), Vol. 371, pp. 254–258.
[48]R. W. MacCormack, "The effect of viscosity in hypervelocity impact catering," AIAA Paper AIAA-69-354 (1969).
[49]T. J. Poinsot and S. K. Lele, "Boundary conditions for direct simulations of compressible viscous flows," J. Comput. Phys. **101**, 104 (1992).
[50]D. H. Rudy and J. C. Strikwerda, "Boundary conditions for subsonic compressible Navier–Stokes calculations," J. Comput. Phys. **36**, 327 (1980).
[51]J. J. Riley and R. W. Metcalfe, "Direct numerical simulations of a perturbed, turbulent mixing layer," AIAA Paper AIAA-80-0274 (1980).
[52]N. D. Sandham and W. C. Reynolds, "Three-dimensional simulations of large eddies in the compressible mixing layer," J. Fluid Mech. **224**, 133 (1991).
[53]R. D. Moser and M. M. Rogers, "The three-dimensional evolution of a plane mixing layer: Pairing and transition to turbulence," J. Fluid Mech. **247**, 275 (1993).
[54]R. W. Metcalfe, S. A. Orszag, M. E. Brachet, S. Menon, and J. J. Riley, "Secondary instabilities of a temporally growing mixing layer," J. Fluid Mech. **184**, 207 (1987).
[55]S. J. Lin and G. M. Corcos, "The mixing layer: Deterministic models of a turbulent flow. Part 3. The effect of plane strain on the dynamics of streamwise vortices," J. Fluid Mech. **141**, 139 (1984).
[56]R. D. Moser and M. M. Rogers, "The three-dimensional evolution of a plane mixing layer: The Kelvin–Helmholtz rollup," J. Fluid Mech. **243**, 183 (1992).
[57]R. D. Moser and M. M. Rogers, "Spanwise scale selection in plane mixing layers," J. Fluid Mech. **247**, 321 (1993).
[58]J. H. Ferziger, "Higher level simulations of turbulent flows," Stanford University Report TF-16, Department of Mechanical Engineering, Stanford University, Stanford, CA, 1981.
[59]G. Erlebacher, M. Y. Hussaini, C. G. Speziale, and T. A. Zang, "Toward the large eddy simulation of compressible turbulent flows," J. Fluid Mech. **238**, 155 (1992).
[60]R. S. Rogallo and P. Moin, "Numerical simulation of turbulent flow," Annu. Rev. Fluid Mech. **16**, 99 (1984).
[61]J. W. Deardorff, "On the magnitude of the subgrid scale eddy coefficient," J. Comput. Phys. **7**, 120 (1971).
[62]U. Piomelli, "Large-eddy simulation: Achievements and challenges," Prog. Aerosp. Sci. **35**, 335 (1999).
[63]C. Meneveau and J. Katz, "Scale-invariance and turbulence models for large-eddy simulations," Annu. Rev. Fluid Mech. **32**, 1 (2000).
[64]U. Piomélli, W. H. Cabot, P. Moin, and S. Lee, "Subgrid-scale backscatter in turbulent and transitional flows," Phys. Fluids A **3**, 1766 (1991).
[65]P. J. Mason and D. J. Thomson, "Stochastic backscatter in large eddy simulation of boundary layers," J. Fluid Mech. **242**, 51 (1992).
[66]D. Carati, S. Ghosal, and P. Moin, "On the representation of backscatter in dynamic localization models," Phys. Fluids **7**, 606 (1995).
[67]M. Germano, "A statistical formulation of the dynamic model," Phys. Fluids **8**, 565 (1996).
[68]J. W. Deardorff, "A numerical study of three-dimensional turbulent channel flow at large Reynolds number," J. Fluid Mech. **41**, 453 (1970).
[69]R. W. Bilger, "Future progress in turbulent combustion research," Prog. Energy Combust. Sci. **26**, 367 (2000).
[70]N. Peters, *Turbulent Combustion* (Cambridge University Press, Cambridge, UK, 2000).
[71]J. H. Bell and R. D. Metha, "Development of a two-stream mixing layer from tripped and untripped boundary layer," AIAA J. **28**, 2034 (1990).
[72]M. M. Rogers and R. D. Moser, "Direct simulation of a self-similar turbulent mixing layer," Phys. Fluids **6**, 903 (1994).
[73]A. D. Leonard and F. Dai, "Applications of a coupled Monte Carlo PDF/finite volume, CFD method for turbulent combustion," AIAA Paper AIAA-94-2904 (1994).

A stochastic Lagrangian model for acceleration in turbulent flows

Stephen B. Pope[a)]
Sibley School of Mechanical and Aerospace Engineering, Cornell University, Ithaca, New York 14853

(Received 14 January 2001; accepted 17 April 2002; published 3 June 2002)

A stochastic model is developed for the acceleration of a fluid particle in anisotropic and inhomogeneous turbulent flows. The model consists of an ordinary differential equation for velocity (which contains directly the acceleration due to the mean and rapid pressure gradients), and a stochastic model for the remainder of the acceleration, which is due to the slow pressure gradient and to viscosity. In addition to a rapid-pressure model, the stochastic model involves three tensor coefficients. For isotropic turbulence, the model reverts to that previously proposed by Sawford. At high Reynolds number the model is consistent with local isotropy and the Kolmogorov hypotheses, and tends to the generalized Langevin model for fluid-particle velocity. In this case two of the tensor coefficients are known in terms of the Kolmogorov constant C_0, while the third is related to the coefficient in the generalized Langevin model. A complete analysis of the model is performed for homogeneous turbulent shear flow, for which there are Lagrangian data from direct numerical simulations. The main result is to establish the one-to-one correspondence between the model coefficients and the primary statistics, namely, the velocity and acceleration covariances and the tensor of velocity integral time scales. The autocovariances of velocity and acceleration obtained from the model are in excellent agreement with the direct numerical simulation (DNS) data. Future DNS studies of homogeneous turbulence can be used to investigate the dependence of the model coefficients on Reynolds number and on the imposed mean velocity gradients. The acceleration model can be used to generate a range of turbulence models which, in a natural way, incorporate Reynolds-number effects. © *2002 American Institute of Physics.* [DOI: 10.1063/1.1483876]

I. INTRODUCTION

In order to investigate dispersion in turbulent flows, in 1921 Taylor[1] introduced a stochastic model for the position $\mathbf{X}^+(t)$ of a fluid particle. An analysis of Taylor's model shows that it is equivalent to the Langevin equation as a model for the fluid-particle velocity $\mathbf{U}^+(t)=d\mathbf{X}^+(t)/dt$. (Langevin[2] had proposed this stochastic equation in 1908 to model the velocity of particles undergoing Brownian motion.) The Langevin equation remains the basis for stochastic models of turbulent dispersion (see, e.g., Refs. 3–5). Furthermore the Langevin equation and its generalization[6,7] provide a closure to the transport equation for the (one-point, one-time) probability density function (PDF) of velocity.[8,9] And from the modeled velocity PDF equation can be deduced the corresponding partially modeled Reynolds-stress equation.[10] Thus, an accurate stochastic model for the fluid-particle velocity $\mathbf{U}^+(t)$ is a potent tool in turbulence modeling as well as in the study of turbulent dispersion.

Important conclusions about the performance of the Langevin model can be drawn from the simplest case of statistically stationary homogeneous isotropic turbulence. In general, the fluctuating component of fluid-particle velocity is defined by

$$\mathbf{u}^+(t)=\mathbf{U}^+(t)-\langle\mathbf{U}(\mathbf{X}^+[t],t)\rangle, \tag{1}$$

where $\mathbf{U}(\mathbf{x},t)$ is the Eulerian velocity; and for the case considered $\mathbf{u}^+(t)$ is a statistically stationary process with mean zero. The Lagrangian velocity autocorrelation function is defined by

$$\rho(s)\equiv\langle u^+_{(i)}(t)u^+_{(i)}(t+s)\rangle/\langle u^+_{(i)}(t)u^+_{(i)}(t)\rangle, \tag{2}$$

which is independent of t and i because of stationarity and isotropy, respectively. (Here and below, bracketed suffixes are excluded from the summation convention.) The Langevin model predicts this autocorrelation function to be[9]

$$\rho(s)=\exp\left(\frac{-|s|}{T_L}\right), \tag{3}$$

where T_L is the Lagrangian integral time scale. For not-too-small time intervals $|s|/T_L$, this prediction is in excellent agreement with experimental and direct numerical simulation (DNS) data.[11]

But the form of Eq. (3) reveals three related shortcomings of the Langevin model. First, it contains the single time scale T_L (which is characteristic of the large-scale, energy-containing motions); second, there is no dependence on Reynolds number; and, third, the slope of $\rho(s)$ given by Eq. (3) is discontinuous at the origin [reflecting the fact that the Langevin model for $\mathbf{u}^+(t)$ is continuous but not differentiable]. The same observations can be made[12] regarding the Lagrangian velocity frequency spectrum $E_L(\omega)$—which is the Fourier transform of $\langle u^+_{(i)}u^+_{(i)}\rangle\rho(s)$. According to the Langevin model, at high frequency $E_L(\omega)$ varies at ω^{-2}:

a)Electronic mail: pope@mae.cornell.edu

there is no representation of the more rapid decrease in $E_L(\omega)$ beyond the frequency corresponding to the Kolmogorov time scale τ_η.

In 1991, Sawford[12] introduced (for isotropic turbulence) a stochastic model for the fluid-particle acceleration $\mathbf{A}^+(t) = d\mathbf{U}^+(t)/dt = d^2\mathbf{X}^+(t)/dt^2$. Such a model remedies the above-mentioned deficiencies of the Langevin model: a second time scale (which scales with τ_η) is introduced; there is an intrinsic Reynolds-number dependence (since T_L/τ_η increases with Reynolds number); and, at the origin, the predicted velocity autocorrelation function is once continuously differentiable. Correspondingly, around the Kolmogorov frequency τ_η^{-1}, the Lagrangian velocity spectrum $E_L(\omega)$ smoothly changes its power-law behavior from ω^{-2} to ω^{-4}. For isotropic turbulence, Sawford's model is in excellent agreement with DNS data, including accounting for the Reynolds-number dependence of the acceleration autocorrelation function and the second-order Lagrangian velocity structure function.[12,13]

In this paper we consider a more general stochastic model for the fluid-particle acceleration, which is applicable to anisotropic turbulence and to inhomogeneous turbulent flows. The general form of the model is developed in Sec. II, where particular attention is paid to the contribution to acceleration from the rapid pressure gradient. When applied to homogeneous turbulence (with constant and uniform mean velocity gradients) the stochastic model is of the form

$$da_i^*(t) = -[C_{ij}a_j^*(t) + D_{ij}u_j^*(t)]dt + B_{ij}\,dW_j, \tag{4}$$

where $\mathbf{u}^*(t)$ is the model for $\mathbf{u}^+(t)$, $\mathbf{a}^*(t)$ is its rate of change (i.e., $\mathbf{a}^* \equiv d\mathbf{u}^*/dt$), and $\mathbf{W}(t)$ is an isotropic Wiener process.[9] The coefficients **B**, **C**, and **D** are tensors which can depend on the local state of the flow and the turbulence, but are independent of $\mathbf{a}^*$ and $\mathbf{u}^*$. (The conventional notation is that "+" denotes a fluid-particle property, and "*" denotes a model for that property.)

In the simplest case of isotropic turbulence, all the coefficients in Eq. (4) are isotropic (e.g., $B_{ij} = B\,\delta_{ij}$), and the model reverts to Sawford's.[12] In this case, which is reviewed in Sec. III C, there is a one-to-one correspondence between the three scalar coefficients (B, C, and D) and the three primary statistics: the acceleration variance a'^2; the velocity variance u'^2; and the velocity integral time scale T_L.

Beyond isotropic turbulence, the simplest type of flow to study is statistically stationary homogeneous turbulence with imposed mean velocity gradients—as exemplified by a recent DNS of forced homogeneous turbulent shear flow,[14] and described in Sec. IV. For this case the coefficients **B**, **C**, and **D** are constant, and a complete analysis of the model [Eq. (4)] can be performed. This is done in Sec. IV B, where it is shown that there is a one-to-one correspondence between the tensor coefficients in the model and the primary statistics, namely the velocity-acceleration covariances and the velocity integral time scale tensor. (This analysis parallels the authors's recent analysis of a stochastic model for velocity.[15])

With some approximation (and with an appropriate scaling of the variables), the same analysis can be applied to nonstationary homogeneous turbulence, in particular to (unforced) homogeneous turbulent shear flow for which there are Lagrangian data from the recent DNS studies of Sawford and Yeung.[16,17] It is shown (in Sec. IV C) that the velocity-acceleration autocorrelation functions predicted by the model are in excellent agreement with these DNS data.

As well as being useful in its own right, we also regard the acceleration model as an intermediate step in the development of improved stochastic models for velocity for use in dispersion studies, in PDF methods, and in other turbulence models. Compared to the velocity model, the acceleration model can be more closely related to Lagrangian data from DNS, which are known to contain strong Reynolds-number dependencies.[11,18] Given an acceleration model (i.e., a prescription for the coefficients **B**, **C**, and **D**), a corresponding velocity model can be deduced[15] which yields the same velocity covariances and integral time scales, and which inherits the Reynolds-number dependencies. Such an improved model has direct application in PDF methods, and from it can be deduced a pressure-rate-of-strain model for use in Reynolds-stress models. These and other uses of the acceleration model are discussed in Sec. V.

II. STOCHASTIC MODEL FOR ACCELERATION

We consider the inhomogeneous turbulent flow of a constant-property Newtonian fluid (of density ρ and kinematic viscosity ν). This is governed by the continuity equation $\partial U_i/\partial x_i = 0$, and the Navier–Stokes equation

$$A_i(\mathbf{x},t) \equiv \frac{DU_i}{Dt} = \left(\frac{\partial}{\partial t} + U_j\frac{\partial}{\partial x_j}\right)U_i = -\frac{1}{\rho}\frac{\partial p}{\partial x_i} + \nu\frac{\partial^2 U_i}{\partial x_j \partial x_j}, \tag{5}$$

where $\mathbf{A}(\mathbf{x},t)$, $\mathbf{U}(\mathbf{x},t)$, and $p(\mathbf{x},t)$ are the acceleration, velocity, and pressure. The general fluid particle has position $\mathbf{X}^+(t)$, velocity,

$$\mathbf{U}^+(t) = \frac{d\mathbf{X}^+(t)}{dt} = \mathbf{U}(\mathbf{X}^+[t],t), \tag{6}$$

and acceleration

$$\mathbf{A}^+(t) = \frac{d\mathbf{U}^+(t)}{dt} = \mathbf{A}(\mathbf{X}^+[t],t). \tag{7}$$

A. Decomposition of acceleration

The acceleration can be decomposed into mean and fluctuating contributions based on the mean ($\langle\mathbf{U}\rangle$ and $\langle p\rangle$) and fluctuating ($\mathbf{u}$ and p') components of velocity and pressure. Furthermore, as originally shown by Chou,[19] the fluctuating pressure can be decomposed into rapid, $p^{(r)}$, slow, $p^{(s)}$, and harmonic, $p^{(h)}$, contributions.[9] Thus, the fluid acceleration is

$$A_i = -\frac{1}{\rho}\frac{\partial\langle p\rangle}{\partial x_i} - \frac{1}{\rho}\frac{\partial p^{(r)}}{\partial x_i} - \frac{1}{\rho}\frac{\partial p^{(s)}}{\partial x_i} - \frac{1}{\rho}\frac{\partial p^{(h)}}{\partial x_i} + \nu\frac{\partial^2\langle U_i\rangle}{\partial x_j\partial x_j} + \nu\frac{\partial^2 u_i}{\partial x_j\partial x_j}. \tag{8}$$

The harmonic pressure and the mean viscous term are negligible except in the immediate vicinity of walls (or other

surfaces). Here we neglect these terms, and hence leave to future work the development of the special treatments required for the viscous near-wall region.

B. Structure of the model

The proposed model consists of an ordinary differential equation (ODE) for $\mathbf{U}^*(t)$—a model for the fluid particle velocity $\mathbf{U}^+(t)$—and a stochastic differential equation (SDE) for an acceleration variable denoted by $\mathbf{A}^0(t)$. The model also involves the fluctuating components of these quantities, which are defined by

$$\mathbf{u}^*(t) \equiv \mathbf{U}^*(t) - \langle \mathbf{U}^*(t) | \mathbf{X}^*(t) \rangle \tag{9}$$

and

$$\mathbf{a}^0(t) \equiv \mathbf{A}^0(t) - \langle \mathbf{A}^0(t) | \mathbf{X}^*(t) \rangle, \tag{10}$$

where $\mathbf{X}^*(t)$ denotes the position of the model particle.

The ODE for velocity is

$$\frac{dU_i^*}{dt} = -\left(\frac{1}{\rho}\frac{\partial \langle p \rangle}{\partial x_i}\right)_{\mathbf{X}^*(t)} - \left(\frac{1}{\rho}\frac{\partial p^{(r)}}{\partial x_i}\right)_{\mathbf{X}^*(t)} + a_i^0(t), \tag{11}$$

where the first two contributions on the right-hand side represent acceleration by the mean pressure gradient (which is assumed to be known), and acceleration by the rapid pressure gradient (which has to be modeled). A comparison of Eq. (8) and Eq. (11) then reveals that $\mathbf{a}^0(t)$ is a model for the acceleration due to the slow pressure gradient and the viscous term.

The acceleration variable $\mathbf{A}^0(t)$ is modeled by the general SDE,

$$dA_i^0(t) = -[C_{ij}A_j^0(t) + D_{ij}u_j^*(t)]dt + B_{ij}\,dW_j, \tag{12}$$

where $\mathbf{W}(t)$ is an isotropic Wiener process. The tensor functions $\mathbf{B}(\mathbf{x},t)$, $\mathbf{C}(\mathbf{x},t)$, and $\mathbf{D}(\mathbf{x},t)$ [which in Eq. (12) are evaluated at $[\mathbf{X}^*(t),t]$] depend on the local state of the turbulence, but are independent of $\mathbf{U}^*$ and $\mathbf{A}^0$.

C. Homogeneous turbulence

Before presenting the rationale for the structure of the model, we first note the form that it takes in homogeneous turbulence.

In homogeneous turbulence (with uniform mean velocity gradients), the coefficients $\mathbf{B}$, $\mathbf{C}$, and $\mathbf{D}$ depend only on time, and it follows that the mean $\langle \mathbf{A}^0(t) | \mathbf{X}^*(t) \rangle = \langle \mathbf{A}^0(t) \rangle$ is zero. Consequently $\mathbf{a}^0(t)$ is identical to $\mathbf{A}^0(t)$. And the velocity equation can readily be transformed to an equation for $\mathbf{u}^*(t)$. Thus, for homogeneous turbulence the model becomes

$$\frac{du_i^*}{dt} = -\frac{\partial \langle U_i \rangle}{\partial x_j}u_j^* - \left(\frac{1}{\rho}\frac{\partial p^{(r)}}{\partial x_i}\right)_{\mathbf{X}^*(t)} + a_i^0(t), \tag{13}$$

$$da_i^0(t) = -[C_{ij}a_j^0(t) + D_{ij}u_j^*(t)]dt + B_{ij}\,dW_j. \tag{14}$$

D. Rationale

The structure of the model is such that some contributions to acceleration—namely, from the mean and rapid pressure gradients—appear directly in the ODE for velocity, Eq. (11); whereas the other contributions—from the slow pressure gradient and viscosity—are modeled through the SDE for $\mathbf{A}^0(t)$, Eq. (12). The rationale for this division is based on the response of the system to a rapid distortion, and it can be most easily understood for the case of homogeneous turbulence.

Consider the sudden imposition of a very large strain rate on homogeneous turbulence. Both the mean and rapid pressure fields change suddenly and this leads to a sudden change in the fluid acceleration. On the other hand, the fluctuating velocity field and the slow pressure change continuously in response to the suddenly imposed distortion.

The model is qualitatively in accord with this behavior. It may be seen from Eq. (11) and Eq. (13) that the acceleration changes suddenly if there is a sudden change in $\partial \langle U_i \rangle / \partial x_j$, with accompanying sudden changes in $\partial \langle p \rangle / \partial x_i$ and $\partial p^{(r)}/\partial x_i$. In the acceleration equation [Eq. (12) and Eq. (14)], these sudden changes can result in sudden changes in the coefficients, $\mathbf{B}$, $\mathbf{C}$, and $\mathbf{D}$, but nevertheless, $\mathbf{a}^0(t)$ changes continuously.

E. Rapid-pressure models

As is usual, and in keeping with the physics, we consider deterministic models for the rapid pressure gradient. The quantity then to be modeled is the conditional mean rapid pressure gradient—conditional on the modeled state of the fluid particle.

For homogeneous turbulence, the rapid pressure varies linearly with the imposed mean velocity gradient, and hence the general model can be written[20]

$$\left\langle -\frac{1}{\rho}\frac{\partial p^{(r)}}{\partial x_i}\middle| \mathbf{a}^0, \mathbf{u}^* \right\rangle = 2\frac{\partial \langle U_k \rangle}{\partial x_\ell} N_{\ell ki}. \tag{15}$$

The third-order tensor function $N_{\ell ki}$ is given in terms of two-point conditional velocity statistics in Refs. 20 and 8 (where it is denoted by $B_{\ell ki}$), and it satisfies the relations

$$N_{\ell ii} = u_\ell^*, \quad N_{\ell \ell i} = 0, \quad N_{\ell ki} = N_{\ell ik}. \tag{16}$$

Rapid distortions of homogeneous turbulence can be treated exactly using the wave-vector model of Van Slooten and Pope.[9,21] This requires that the modeled state of the fluid particle be supplemented by the wave vector $\mathbf{e}^*(t)$—which, among other conditions, satisfied the relations

$$e_i^* e_i^* \equiv 1, \quad e_i^* u_i^* = 0. \tag{17}$$

Then the tensor $N_{\ell ki}$ in Eq. (15) is given by

$$N_{\ell ki} = u_\ell^* e_k^* e_i^*. \tag{18}$$

For rapid distortions, the wave-vector model consists of ODE's for $\mathbf{e}^*(t)$ and $\mathbf{u}^*(t)$, the latter being Eq. (13) with the neglect of $\mathbf{a}^0$, and with the rapid-pressure model given by Eqs. (15) and (18). This model is exact for arbitrary rapid distortions of homogeneous turbulence, in the sense that it yields the correct evolution of the Reynolds stresses.

As is conventional in Reynolds-stress and velocity-PDF modeling, we are primarily concerned here with models based on velocity and its one-point statistics, i.e., $\mathbf{u}^*(t)$ and

the Reynolds stress $\langle u_i u_j \rangle$. The unfortunate fact of the matter is that these quantities are inadequate to describe rapid distortions (see, e.g., Reynolds and Kassinos[22]): additional directional information is needed, as is provided by the wave vector. However, the hope is that rapid-pressure models based on velocity alone may be adequate for the moderate and slowly varying mean strain rates encountered in many turbulent shear flows.

Following Ref. 20, it is natural to consider a rapid-pressure model that is linear in velocity, and which therefore can be written

$$\left\langle -\frac{1}{\rho}\frac{\partial p^{(r)}}{\partial x_i}\middle| \mathbf{a}^0, \mathbf{u}^* \right\rangle = G_{ij}^{(r)} u_j^* = H_{ijk\ell}^{(r)} u_j^* \frac{\partial \langle U_k \rangle}{\partial x_\ell}, \tag{19}$$

or, equivalently,

$$N_{\ell ki} = \tfrac{1}{2} H_{ijk\ell}^{(r)} u_j^*, \tag{20}$$

where the tensors $G_{ij}^{(r)}$ and $H_{ijk\ell}^{(r)}$ correspond to the analogous tensors in the Haworth–Pope model.[7,9] The nondimensional fourth-order tensor $\mathbf{H}^{(r)}$ is modeled as a linear function of the Reynolds-stress anisotropy tensor

$$b_{ij} \equiv \frac{\langle u_i u_j \rangle}{\langle u_k u_k \rangle} - \frac{1}{3}\delta_{ij}, \tag{21}$$

and indeed a nontrivial dependence on b_{ij} is required to satisfy the condition that the rapid pressure neither produces nor removes turbulent kinetic energy.

In subsequent sections we confine attention to this linear model, not least because it is amenable to analysis. In DNS, the rapid pressure gradient can extracted, its linearity in $\mathbf{u}^+$ can be examined, and specific models for $H_{ijk\ell}^{(r)}$ can be assessed. With this model, Eq. (13) can be rewritten

$$\frac{du_i^*}{dt} = -K_{ij} u_j^* + a_i^0, \tag{22}$$

where the tensor K_{ij} is defined by

$$K_{ij} = \frac{\partial \langle U_i \rangle}{\partial x_j} - G_{ij}^{(r)} = \frac{\partial \langle U_k \rangle}{\partial x_\ell}[\delta_{ik}\delta_{j\ell} - H_{ijk\ell}^{(r)}]. \tag{23}$$

Finally, we caution that in future studies of rapid-pressure modeling (e.g., based on DNS) nonlinear models should not be discounted. For example, the simple model

$$N_{\ell ki} = \frac{1}{2} u_\ell \left(\delta_{ik} - \frac{u_i^* u_k^*}{u_j^* u_j^*} \right), \tag{24}$$

satisfies all known constraints (without requiring a dependence on b_{ij}).

F. Summary

The model consists of an ODE for velocity, Eq. (11), which contains the mean pressure gradient and a model for the rapid pressure gradient [e.g., Eq. (19)]. The remainder of the acceleration—owing to the slow pressure gradient and the viscous term—is modeled by an SDE, Eq. (12), which contains three tensor coefficients, **B**, **C**, and **D**. Various properties of these coefficients are revealed in subsequent sections.

III. PROPERTIES OF THE MODEL

In this section we examine some of the mathematical properties of the model, and their connections to the physics of turbulent motions.

A. Equivalent first-order and second-order systems

For homogeneous turbulence, the model [Eq. (14) and Eq. (22)] can be written as a first-order system of SDE's,

$$du_i^* = [-K_{ij} u_j^* + a_i^0]dt, \tag{25}$$

$$da_i^0 = -[C_{ij} a_j^0 + D_{ij} u_j^*]dt + B_{ij}\, dW_j, \tag{26}$$

or, in an inferior notation, as a first-order system of ODE's

$$\frac{du_i^*}{dt} = -K_{ij} u_j^* + a_i^0, \tag{27}$$

$$\frac{da_i^0}{dt} = -C_{ij} a_j^0 - D_{ij} u_j^* + B_{ij}\dot{W}_j, \tag{28}$$

where $\dot{\mathbf{W}}$ denotes white noise, which has the property $\int_0^t \dot{\mathbf{W}}(t')dt' = \mathbf{W}(t)$.

Alternatively, by differentiating Eq. (27) with respect to t, the model can be re-expressed as the second-order system

$$\frac{d^2 u_i^*}{dt^2} + (C_{ij} + K_{ij})\frac{du_j^*}{dt} + \left(D_{ij} + \frac{dK_{ij}}{dt} \right) u_j^* = B_{ij}\dot{W}_j. \tag{29}$$

It may be seen that the system is governed fundamentally by just three coefficient tensors, not four as suggested by the appearance of **B**, **C**, **D**, and **K** in Eqs. (25)–(28). In particular, if **K** is constant—as is the case in the analysis below (Sec. IV B)—the behavior of $\mathbf{u}^*(t)$ is determined by **B**, **D** and the sum

$$\bar{\mathbf{C}} \equiv \mathbf{C} + \mathbf{K}, \tag{30}$$

but not by **C** and **K** individually. Thus, for constant **K**, Eqs. (25) and (26) are equivalent to the system

$$du_i^* = a_i^*\, dt, \tag{31}$$

$$da_i^* = -[\bar{C}_{ij} a_j^* + D_{ij} u_j^*]dt + B_{ij}\, dW_j, \tag{32}$$

in which Eq. (31) defines $\mathbf{a}^* \equiv d\mathbf{u}^*/dt$, and $\mathbf{a}^0$ can be recovered as

$$a_i^0 = a_i^* + K_{ij} u_j^*. \tag{33}$$

The model is analyzed below via Eqs. (31) and (32).

B. Scaled model equations and coefficients

It is informative to scale the variables and coefficients in the model equations for homogeneous turbulence so that they become nondimensional quantities of order unity. A preliminary is to define the quantities used to perform these scalings.

The velocity and acceleration variables are scaled by their standard deviations u' and a', which are given by

$$u'^2 \equiv \tfrac{1}{3}\langle u_i^* u_i^* \rangle = \tfrac{2}{3}k, \quad a'^2 \equiv \tfrac{1}{3}\langle a_i^* a_i^* \rangle, \tag{34}$$

TABLE I. Summary of different time scales.

$\tau \equiv k/\epsilon$	Turbulence time scale
$\tau_\eta \equiv (\nu/\epsilon)^{1/2}$	Kolmogorov time scale
$\tau_S \equiv \mathcal{S}^{-1}$	Shear time scale
$T_L \equiv \frac{1}{3}\hat{T}^u_{ii}$	Lagrangian velocity integral time scale
$\tau_a \equiv u'^2/(a'^2\tau)$	Acceleration time scale
$T_\infty \equiv \lambda_1^{-1}$, Eq. (55)	Velocity eigen-time scale
$\tau_0 \equiv \lambda_2^{-1}$, Eq. (57)	Acceleration eigen-time scale
$\mathbf{T}$, Eq. (102)	Integral time scale (6×6) matrix
$\hat{\mathbf{T}}^{uu}$, Eq. (109)	Velocity integral time scale tensor

where k is the turbulent kinetic energy. There are four relevant time scales. The turbulence time scale is defined by

$$\tau \equiv \frac{k}{\epsilon}, \tag{35}$$

where ϵ is the rate of dissipation of k. The shear time scale, characteristic of the imposed mean velocity gradients, is defined by

$$\tau_S \equiv \mathcal{S}^{-1}, \tag{36}$$

where

$$\mathcal{S}^2 \equiv \frac{\partial \langle U_i \rangle}{\partial x_j}\frac{\partial \langle U_i \rangle}{\partial x_j}. \tag{37}$$

The Kolmogorov time scale is

$$\tau_\eta \equiv \left(\frac{\nu}{\epsilon}\right)^{1/2}, \tag{38}$$

and the acceleration time scale is defined by

$$\tau_a \equiv \frac{u'^2}{a'^2\tau}. \tag{39}$$

The ratio τ_η/τ decreases with Reynolds number as

$$\frac{\tau_\eta}{\tau} = \mathrm{Re}^{-1/2} = \left(\frac{20}{3}\right)^{1/2} R_\lambda^{-1}, \tag{40}$$

where the turbulence Reynolds number is $\mathrm{Re} \equiv k^2/(\epsilon\nu)$, and the Taylor-scale Reynolds number is $R_\lambda \equiv (\frac{20}{3}\mathrm{Re})^{1/2}$. The various time scales used throughout the paper are summarized in Table I.

With a_0 being the Kolmogorov-scaled acceleration variance

$$a_0 \equiv \frac{a'^2\tau_\eta}{\epsilon}, \tag{41}$$

the acceleration and Kolmogorov time scales are related by

$$\frac{\tau_a}{\tau_\eta} = \frac{2}{3a_0}. \tag{42}$$

It may be seen then that (at least approximately at high Reynolds number) τ_a scales with τ_η, since according to the Kolmogorov hypotheses a_0 is a universal constant.[23] In fact, it is known[11,24–26] that, at moderate Reynolds numbers, a_0 increases weakly with R_λ—in accord with the refined Kolmogorov hypotheses. In discussing scalings we ignore this weak dependence and write $\tau_a/\tau \sim \mathrm{Re}^{-1/2}$.

The ODE for velocity, Eq. (13) and Eq. (15), can be written

$$\frac{1}{u'}\frac{du_i^*}{d\hat{t}} = \frac{\tau}{u'}\frac{du_i^*}{dt} = \frac{\tau}{\tau_S}\left[\tau_S \frac{\partial \langle U_k \rangle}{\partial x_\ell}\right]\left[\frac{2N_{\ell ki}}{u'} - \frac{u_\ell^*}{u'}\delta_{ik}\right] + \left(\frac{\tau}{\tau_a}\right)^{1/2}\left[\frac{a_i^0}{a'}\right]. \tag{43}$$

Each term is nondimensional; expressions in square brackets are of order unity; and time is scaled by the turbulence time scale, i.e., $\hat{t} \equiv t/\tau$. If the linear rapid-pressure model, Eq. (19), is used, then the ODE for $\mathbf{u}^*(t)$ can alternatively be written

$$\frac{1}{u'}\frac{du_i^*}{d\hat{t}} = -\frac{\tau}{\tau_S}\tilde{K}_{ij}\left[\frac{u_j^*}{u'}\right] + \left(\frac{\tau}{\tau_a}\right)^{1/2}\left[\frac{a_i^0}{a'}\right], \tag{44}$$

where the nondimensional, order-one coefficient $\tilde{\mathbf{K}}$ is

$$\tilde{K}_{ij} = \tau_S K_{ij} = \tau_S \frac{\partial \langle U_k \rangle}{\partial x_\ell}[\delta_{ik}\delta_{j\ell} - H^{(r)}_{ijk\ell}]. \tag{45}$$

It is clear from Eqs. (43) and (44) that $\mathbf{u}_i^*/u'$ responds to the mean velocity gradients at the normalized rate $\tau/\tau_S = \mathcal{S}k/\epsilon$. Under usual circumstances this is of order one, but for rapid distortions it is arbitrarily large. Evidently, the term in $\mathbf{a}^0$ is of order $\sqrt{\tau/\tau_a} \sim \mathrm{Re}^{1/4}$. But since $\mathbf{a}^0$ is a zero-mean random function with normalized time scale τ_a/τ, the cumulative effect of the term on the covariances of $\mathbf{u}^*/u'$ over a time interval $\Delta\hat{t} \gg \tau_a/\tau$ is of order $\sqrt{\tau/\tau_a}^2(\Delta\hat{t}\tau_a/\tau) \sim \Delta\hat{t}$. Thus, although the term in $\mathbf{a}^0$ is relatively large instantaneously (of order $\mathrm{Re}^{1/4}$), its cumulative effect is of order one.

For the SDE for $\mathbf{a}^0(t)$, Eq. (14), we define the scaled coefficients by

$$\tilde{\mathbf{B}}^2 = \frac{\tau_a}{a'^2}\mathbf{B}^2, \quad \tilde{\mathbf{C}} = \tau_a\mathbf{C}, \quad \tilde{\mathbf{D}} = \tau\tau_a\mathbf{D}. \tag{46}$$

The subsequent analysis confirms that these scalings are appropriate, in that each of these scaled coefficients is of order unity. With these definitions, Eq. (14) can be written

$$\frac{da_i^0}{a'} = -\left[\tilde{C}_{ij}\frac{a_j^0}{a'} + \left(\frac{\tau_a}{\tau}\right)^{1/2}\tilde{D}_{ij}\frac{u_j^*}{u'}\right]\frac{dt}{\tau_a} + \tilde{B}_{ij}\frac{dW_j}{\sqrt{\tau_a}}. \tag{47}$$

Clearly τ_a is the characteristic time scale of the process: the mean of the term in $\tilde{\mathbf{C}}$, and the variance of the term in $\tilde{\mathbf{B}}$ is each of order dt/τ_a. However, the term in $\tilde{\mathbf{D}}$ is smaller by the factor of $(\tau_a/\tau)^{1/2} \sim \mathrm{Re}^{-1/4}$.

If the mean velocity gradients are constant, then the equations for $\mathbf{u}^*(t)$ and $\mathbf{a}^0(t)$ [Eqs. (25) and (26)] can be re-expressed as equations for $\mathbf{u}^*(t)$ and $\mathbf{a}^*(t)$ [Eqs. (31) and (32)]. The scaled forms of these equations are

$$\frac{\tau}{u'}\frac{du_i^*}{dt} = \left(\frac{\tau}{\tau_a}\right)^{1/2}\frac{a_i^*}{a'} \tag{48}$$

and

$$\frac{da_i^*}{a'}=-\left[\tilde{C}_{ij}\frac{a_j^*}{a'}+\left(\frac{\tau_a}{\tau_S}\right)\tilde{K}_{ij}\frac{a_j^*}{a'}+\left(\frac{\tau_a}{\tau}\right)^{1/2}\tilde{D}_{ij}\frac{u_j^*}{u'}\right]\frac{dt}{\tau_a}+\tilde{B}_{ij}\frac{dW_j}{\sqrt{\tau_a}}. \tag{49}$$

For the case considered τ/τ_S is of order unity, so that (compared to the leading-order terms) the terms in $\tilde{\mathbf{K}}$ and $\tilde{\mathbf{D}}$ are of order $\tau_a/\tau\sim \mathrm{Re}^{-1/2}$ and $(\tau_a/\tau)^{1/2}\sim \mathrm{Re}^{-1/4}$, respectively.

C. Isotropic turbulence

We consider in this section the simplest case of homogeneous isotropic turbulence made statistically stationary by artificial forcing. We do so to relate the general model proposed here to Sawford's,[12] and to provide a characterization of the model's behavior in this simple setting. This provides a useful reference for the results obtained below for the general case.

For isotropic turbulence without mean velocity gradients, there is no rapid pressure, and $\mathbf{a}^*(t)=d\mathbf{u}^*/dt$ is the model for the fluid-particle acceleration. The coefficients in the model, Eq. (32), are inevitably isotropic ($B_{ij}=B\delta_{ij}$, $\tilde{B}_{ij}=\tilde{B}\delta_{ij}$, etc.), and so the three components of $\mathbf{a}^*(t)$ are statistically identical and independent. Writing $a^*(t)$ for one component of acceleration [e.g., $a^*(t)\equiv a_1^*(t)$], and with $u^*(t)$ being the corresponding component of velocity, the model for isotropic turbulence is

$$da^*=-[Ca^*+Du^*]dt+B\,dW. \tag{50}$$

This is identical to Sawford's model,[12] but with the coefficients expresses differently.

An analysis of Eq. (50) (see Refs. 12 and 13 and Sec. IV B) shows that the acceleration variance is

$$\langle a^{*2}\rangle=\frac{B^2}{2C}=a'^2\frac{\tilde{B}^2}{2\tilde{C}}, \tag{51}$$

the velocity variance is

$$\langle u^{*2}\rangle=\frac{B^2}{2CD}=u'^2\frac{\tilde{B}^2}{2\tilde{C}\tilde{D}}, \tag{52}$$

and that the Lagrangian velocity integral time scale is

$$T_L\equiv\int_0^\infty\rho(s)ds=\frac{C}{D}=\tau\frac{\tilde{C}}{\tilde{D}}, \tag{53}$$

where $\rho(s)$ is the Lagrangian velocity autocorrelation function defined by Eq. (2).

There is a one-to-one correspondence between the three model coefficients B, C, and D, and the three primary statistics a'^2, u'^2, and T_L. Equations (51)–(53) are readily inverted to yield for the scaled coefficients

$$\tilde{C}=\frac{T_L}{\tau},\quad \tilde{B}^2=\frac{2T_L}{\tau},\quad \tilde{D}=1. \tag{54}$$

The velocity autocorrelation function $\rho(s)$ obtained from the model is most conveniently and naturally written in terms of two different (but related) time scales, T_∞ and τ_0 ($T_\infty>\tau_0$). These are the inverses of the two eigenvalues of the system, which are given by the solution to the quadratic equation

$$\lambda^2-C\lambda+D=0. \tag{55}$$

The solutions are given in terms of T_L and τ_a by

$$\lambda_1^{-1}=T_\infty=\frac{1}{2}T_L\left[1+\left(1-\frac{4\tau_a\tau}{T_L^2}\right)^{1/2}\right] \tag{56}$$

and

$$\lambda_2^{-1}=\tau_0=\frac{1}{2}T_L\left[1-\left(1-\frac{4\tau_a\tau}{T_L^2}\right)^{1/2}\right]. \tag{57}$$

Conversely we have

$$T_L=T_\infty+\tau_0 \tag{58}$$

and

$$\tau_a=\frac{T_\infty\tau_0}{\tau}. \tag{59}$$

It may be observed that as τ_a/T_L tends to zero, T_∞ and τ_0 tend to T_L and $\tau_a(\tau/T_L)$, respectively. The coefficients B, C, and D given by Eq. (54) can be re-expressed in terms of T_∞ and τ_0, which is the form originally given by Sawford.[12]

The velocity autocorrelation function given by the model is

$$\rho(s)=\left[e^{-|s|/T_\infty}-\left(\frac{\tau_0}{T_\infty}\right)e^{-|s|/\tau_0}\right]\Big/\left(1-\frac{\tau_0}{T_\infty}\right), \tag{60}$$

which is a linear combination of two decaying exponentials, with time scales τ_0 and T_∞.

To conclude, based on this examination of the model in isotropic turbulence, we summarize some important observations which are mirrored in the analysis of the general model presented below.

(1) The three model coefficients B, C, and D are uniquely related to the three primary statistics, a'^2, u'^2, and T_L.
(2) The autocorrelation function $\rho(s)$ is a linear combination of decaying exponentials, the time scales of which are the inverses of the eigenvalues of the system.
(3) The predictions of the model are in excellent agreement with Lagrangian statistics obtained from DNS (see Refs. 12 and 13).
(4) Given the primary statistics, a separate acceleration time scale cannot be imposed on the model: instead the acceleration time scale τ_a is given by Eq. (39).
(5) The simplest scaling arguments show that T_L scales with τ, and that τ_a scales with τ_η, so that the scaled coefficients $\tilde{B}$, $\tilde{C}$, and $\tilde{D}$ are of order unity.

D. Gaussianity

For homogeneous turbulence, the model takes the form of a set of SDEs, Eqs. (31) and (32), in which the drift coefficients ($-\bar{C}_{ij}a_j^*$ and $-D_{ij}u_j^*$) are linear in the dependent variables, while the diffusion coefficient B_{ij} is independent of $\mathbf{a}^*$ and $\mathbf{u}^*$. Such linear stochastic differential equa-

tions are known[27] to yield Gaussian processes. Thus, according to the model, the processes $\mathbf{a}^*(t)$ and $\mathbf{u}^*(t)$ are jointly Gaussian.

For homogeneous turbulent shear flow, the experiments of Tavoularis and Corrsin[28] clearly show that the one-point one-time joint PDF of velocity is joint normal. Hence the model is correct in predicting that the one-time PDF $\mathbf{u}^*(t)$ is joint normal. However, it is known from DNS[11] and experiments[26,29] that both acceleration and two-time velocity statistics depart from Gaussianity, an effect which is not represented by the model. It is possible to represent these effects in stochastic models by making the model coefficients themselves stochastic processes.[30,31] In particular, Beck[31] shows that the experimental acceleration distribution can be accurately represented by a stochastic model with gamma-distributed coefficients. Here, however, we retain constant coefficients and do not attempt to represent these higher-order effects.

It is emphasized that the Gaussianity of the model is confined to homogeneous turbulence. For inhomogeneous flows, non-Gaussian statistics such as the velocity triple correlation can be accurately calculated by linear stochastic models.

E. High Reynolds number and local isotropy

We now consider the limit of very high Reynolds number, which is equivalent to the limit of τ_a/τ tending to zero. In this limit, according to the Kolmogorov hypotheses, the turbulence is locally isotropic. As is now shown, the stochastic model for acceleration is consistent with local isotropy provided that the scaled coefficients $\tilde{\mathbf{B}}$ and $\tilde{\mathbf{C}}$ tend to the following isotropic constant tensors:

$$\tilde{B}_{ij}^2 = 2(\tfrac{3}{4}C_0)^{-1}\delta_{ij} \quad \text{and} \quad \tilde{C}_{ij} = (\tfrac{3}{4}C_0)^{-1}\delta_{ij}, \tag{61}$$

where C_0 is the Kolmogorov constant associated with the second-order Lagrangian structure function [see Eq. (69)].

In general, variations in $\mathbf{u}^*(t)$ and $\mathbf{a}^0(t)$ occur on the time scales τ and τ_a, respectively. For the case considered, $\tau_a \ll \tau$, $\mathbf{u}^*(t)$ changes very slowly compared to $\mathbf{a}^0(t)$; and so $\mathbf{a}^0(t)$ is in a statistically quasistationary state, the statistics of which change slowly in response to the changes in $\mathbf{u}^*(t)$. This state is governed by Eq. (47), with the coefficients given by Eq. (61), which can be rewritten

$$da_i^0 = -(a_i^0 - \mu_i[\mathbf{u}^*(t)])\frac{dt}{\frac{3}{4}C_0\tau_a} + \frac{a'\,dW_i}{\sqrt{\frac{3}{8}C_0\tau_a}}, \tag{62}$$

with

$$\mu_i(\mathbf{u}^*) \equiv -\frac{3}{4}C_0 a'\left(\frac{\tau_a}{\tau}\right)^{1/2}\tilde{D}_{ij}\frac{u_j^*}{u'} = -\frac{3}{4}C_0\frac{\tilde{D}_{ij}u_j^*}{\tau}. \tag{63}$$

With μ_i being considered as a frozen coefficient, Eq. (62) is simply the Langevin equation; and hence each component of $\mathbf{a}^0(t)$ is an independent Ornstein–Uhlenbeck (OU) process with conditional mean $\mu_i(\mathbf{u}^*(t))$, variance a'^2, and time scale $\frac{3}{4}C_0\tau_a$. The normalized mean μ_i/a' tends to zero as (τ_a/τ) tends to zero [see Eq. (63)], and hence $\mathbf{a}^0(t)$ tends to a locally isotropic process.

We now examine the model equation for velocity in the high Reynolds number limit. For a general inhomogeneous flow, the model for $\mathbf{u}^*(t)$ [Eqs. (13) and (19)] is

$$\frac{du_i^*}{dt} = \left(-\frac{\partial\langle U_i\rangle}{\partial x_j} + G_{ij}^{(r)}\right)u_j^* + a_i^0(t). \tag{64}$$

As τ_a/τ tends to zero, $\mathbf{a}^0(t)$ tends to white noise; or, more precisely, for a time interval δt such that both $\tau_a/\delta t$ and $\delta t/\tau$ tend to zero, the increment in velocity

$$\int_t^{t+\delta t}\mathbf{a}^0(t')dt', \tag{65}$$

tends to a Gaussian random vector with mean $\boldsymbol{\mu}(\mathbf{u}^*(t))\,\delta t$, Eq. (63), and covariance

$$2a'^2(\tfrac{3}{4}C_0\tau_a)\delta_{ij}\delta t = C_0\epsilon\delta_{ij}\delta t. \tag{66}$$

Thus, in the limit, Eq. (64) tends to a diffusion process given by the SDE,

$$du_i^* = \left(-\frac{\partial\langle U_i\rangle}{\partial x_j} + G_{ij}\right)u_j^*\,dt + (C_0\epsilon)^{1/2}dW_i, \tag{67}$$

with

$$G_{ij} \equiv G_{ij}^{(r)} - \frac{3}{4}C_0\frac{\tilde{D}_{ij}}{\tau}. \tag{68}$$

It may be recognized that Eq. (67) is the generalized Langevin model (GLM[7,9]); and from this observation we draw two important conclusions. First, it is well known that the GLM is consistent with local isotropy and the Kolmogorov hypotheses in yielding (for the second-order Lagrangian structure function)

$$\langle[u_i^*(t+s)-u_i^*(t)][u_j^*(t+s)-u_j^*(t)]\rangle = C_0\epsilon s\delta_{ij}, \quad \text{for } s \ll \tau. \tag{69}$$

Second, in the high Reynolds number limit being considered, Eq. (68) gives the GLM coefficient G_{ij} which corresponds to the acceleration model coefficients $G_{ij}^{(r)}$ and $\tilde{D}_{ij}$.

For forced, statistically stationary homogeneous isotropic turbulence, the GLM coefficient G_{ij} is constrained to be $-\frac{3}{4}C_0\delta_{ij}/\tau$.[9] Correspondingly, Eq. (68) yields $\tilde{D}_{ij} = \delta_{ij}$, consistent with Sawford's model, Eq. (54). In general, if the GLM coefficient G_{ij} is decomposed into slow and rapid contributions, i.e.,

$$G_{ij} = G_{ij}^{(s)} + G_{ij}^{(r)}, \tag{70}$$

then Eq. (68) yields

$$G_{ij}^{(s)} = -\frac{3}{4}C_0\frac{\tilde{D}_{ij}}{\tau}. \tag{71}$$

The simplest specification of $G_{ij}^{(s)}$ (for unforced turbulence) is

$$G_{ij}^{(s)} = -\left(\frac{1}{2} + \frac{3}{4}C_0\right)\frac{\delta_{ij}}{\tau}. \tag{72}$$

for which the corresponding value of $\tilde{D}_{ij}$ is

$$\tilde{D}_{ij}=\left(1+\frac{2}{3C_0}\right)\delta_{ij}. \tag{73}$$

In summary, with the coefficients $\tilde{\mathbf{B}}$ and $\tilde{\mathbf{C}}$ specified by Eq. (61), the model is consistent with the Kolmogorov hypotheses. At very high Reynolds number (corresponding to τ_a/τ tending to zero), the acceleration statistics are locally isotropic, and the model tends to the generalized Langevin model (GLM) for velocity, Eq. (67). There is then a one-to-one correspondence between the remaining acceleration model coefficient $\tilde{\mathbf{D}}$ and the GLM coefficient G_{ij}, Eq. (68) and Eq. (71).

IV. HOMOGENEOUS TURBULENT SHEAR FLOW

In this section we examine the stochastic model for acceleration applied to homogeneous turbulent shear flow for which there are Lagrangian data from DNS.[16,17] The analysis (performed in Sec. IV B) depends on the processes considered being statistically stationary. We therefore define (in Sec. IV A) a scaled time $\hat{t}$, a scaled velocity $\hat{\mathbf{u}}(\hat{t})$, and the acceleration $\hat{\mathbf{a}}(\hat{t})\equiv d\hat{\mathbf{u}}(\hat{t})/d\hat{t}$ such that $\hat{\mathbf{u}}(\hat{t})$ and $\hat{\mathbf{a}}(\hat{t})$ are statistically stationary processes—at least to a reasonable approximation. Results from the analysis are compared to the DNS data in Sec. IV C.

A. Scaling for statistical stationarity

1. Forced homogeneous turbulent shear flow

We consider first the case of forced homogeneous turbulent shear flow corresponding to the DNS of Schumacher.[14] This case is relatively simple because the flow is statistically stationary. The imposed shear rate $\mathcal{S}$ is constant, as are the turbulent kinetic energy k and its dissipation rate ϵ. The nondimensional time $\hat{t}$ is defined by

$$\hat{t}\equiv t\frac{\epsilon}{k}=\frac{t}{\tau}, \tag{74}$$

and $\hat{\mathbf{u}}(\hat{t})$ is defined as the model for the fluctuating component of velocity following the fluid particle, $\mathbf{u}^*(t)$, normalized by u':

$$\hat{\mathbf{u}}(\hat{t})\equiv\frac{\mathbf{u}^*(t)}{u'}. \tag{75}$$

With these definitions, the velocity covariance $\langle\hat{u}_i\hat{u}_j\rangle$ is of order unity, and so also are the integral time scales of $\hat{\mathbf{u}}(\hat{t})$ (in scaled time). In fact, because of the equality of one-point, one-time Eulerian and Lagrangian statistics in homogeneous turbulence, we have the normalization condition following from Eq. (75):

$$\langle\hat{u}_i(\hat{t})\hat{u}_i(\hat{t})\rangle=3. \tag{76}$$

Since the velocity gradients are constant, the general stochastic model for $\mathbf{u}^*(t)$ and $\mathbf{a}^*(t)$ is given by Eqs. (31) and (32). With the transformations

$$\hat{\mathbf{u}}(\hat{t})=\frac{\mathbf{u}^*(t)}{u'},\quad \hat{\mathbf{a}}(\hat{t})\equiv\frac{d\hat{\mathbf{u}}}{d\hat{t}}=\frac{\tau\mathbf{a}^*(t)}{u'},$$

$$d\hat{t}=\frac{dt}{\tau},\quad d\hat{\mathbf{W}}(\hat{t})=\frac{d\mathbf{W}(t)}{\tau^{1/2}}, \tag{77}$$

these stochastic model equations transform to

$$d\hat{u}_i(\hat{t})=\hat{a}_i(\hat{t})d\hat{t}, \tag{78}$$

$$d\hat{a}_i(\hat{t})=-[\hat{C}_{ij}\hat{a}_j(\hat{t})+\hat{D}_{ij}\hat{u}_j(\hat{t})]d\hat{t}+\hat{B}_{ij}\,d\hat{W}_j(\hat{t}), \tag{79}$$

where the transformed (nondimensional) coefficients are

$$\hat{C}_{ij}=\tau\bar{C}_{ij}=\frac{\tau}{\tau_a}\tilde{C}_{ij}+\tau K_{ij},$$

$$\hat{D}_{ij}=\tau^2D_{ij}=\frac{\tau}{\tau_a}\tilde{D}_{ij}, \tag{80}$$

and

$$\hat{B}_{ij}=\frac{\tau^{3/2}}{u'}B_{ij}=\frac{\tau}{\tau_a}\tilde{B}_{ij}. \tag{81}$$

For a given orientation of the shear, i.e., $\partial\langle U_i\rangle/\partial x_j=\mathcal{S}\delta_{i1}\delta_{j2}$, the coefficients $\hat{\mathbf{B}}$, $\hat{\mathbf{C}}$, and $\hat{\mathbf{D}}$ are constant and depend only on the Reynolds number.

2. Unforced homogeneous turbulent shear flow

The DNS of Sawford and Yeung[16] are consistent with the supposition that (after an initial transient) the energy-containing motions in (unforced) homogeneous turbulent shear flow become (approximately) self-similar. The normalized Reynolds-stress tensor $\langle u_iu_j\rangle/k$ becomes constant, as does the ratio of the turbulence-to-shear time scales, $\tau/\tau_S=\mathcal{S}k/\epsilon$, and hence also the ratio of production $\mathcal{P}$ to dissipation ϵ. (The values deduced from the DNS are $\mathcal{S}k/\epsilon=4.83$ and $\mathcal{P}/\epsilon=1.54$.) The turbulent kinetic energy equation then dictates that k and ϵ increase exponentially with time—as is observed.

As previously argued,[15] this picture suggests that the definitions of $\hat{t}$ and $\hat{\mathbf{u}}(\hat{t})$ by Eq. (74) and Eq. (75) remain appropriate, although now the velocity scale $u'(t)$ used in Eq. (75) depends on time. This time dependence is quantified by the parameter

$$\Pi\equiv\frac{\tau}{u'}\frac{du'}{dt}=\frac{1}{2}\left(\frac{\mathcal{P}}{\epsilon}-1\right), \tag{82}$$

the value of which is $\Pi\approx0.27$ in the present case. (The value is $\Pi=0$ for the forced case, and $\Pi=-\frac{1}{2}$ for decaying turbulence.) Given the (approximately) self-similar state of the energy-containing motions, it is reasonable to suppose that $\hat{\mathbf{u}}(\hat{t})$ is (approximately) statistically stationary. But these states can only be realized approximately since the Reynolds number increases with time. Hence, while we again define $\hat{\mathbf{a}}(\hat{t})$ as the derivative of $\hat{\mathbf{u}}(\hat{t})$, this process cannot be completely stationary: according to Kolmogorov scaling, the amplitude of $\hat{\mathbf{a}}$ increases as $R_\lambda^{1/2}$ and its time scale decreases as R_λ^{-1}.

A quantification of the variation of R_λ in homogeneous turbulent shear flow shows that the departure from stationar-

ity is not large. Based on the exponential increase of k with time it can be shown that R_λ increases as $R_\lambda \sim \exp(\Pi\hat{t})$, and the DNS data are consistent with this behavior (except at the beginning and end of the simulation). The normalized Lagrangian velocity integral time scale is found to be $T_L/\tau = 0.3$.[15] Hence, over a time interval of $2T_L$, R_λ increases by a factor of $\exp(0.27\times 0.6)\approx 1.18$. Thus, over the relevant time interval, the amplitude of $\hat{\mathbf{a}}(\hat{t})$ increases by approximately 10%, while its time scale decreases by about 20%.

As in the forced case, the model equations [Eqs. (31) and (32)] for $\mathbf{u}^*(t)$ and $\mathbf{a}^*(t)$ can be transformed into equations for $\hat{\mathbf{u}}(\hat{t})$ and $\hat{\mathbf{a}}(\hat{t})$. The transformations are those given by Eq. (77), except that $\hat{\mathbf{a}}(\hat{t})$ is given by

$$\hat{\mathbf{a}}(\hat{t}) \equiv \frac{d\hat{\mathbf{u}}(\hat{t})}{d\hat{t}} = \tau \frac{d}{dt}\left(\frac{\mathbf{u}^*(t)}{u'(t)}\right) = \frac{\tau \mathbf{a}^*(t)}{u'} - \Pi\hat{\mathbf{u}}(\hat{t}). \tag{83}$$

The transformed model equations are again Eqs. (78) and (79), with $\hat{\mathbf{B}}$ given by Eq. (81), but with $\hat{\mathbf{C}}$ and $\hat{\mathbf{D}}$ given by

$$\begin{aligned} \hat{C}_{ij} &= \tau \bar{C}_{ij} + 2\Pi\delta_{ij}, \\ \hat{D}_{ij} &= \tau^2 \bar{D}_{ij} + \tau\Pi \bar{C}_{ij} + \Pi^2 \delta_{ij}. \end{aligned} \tag{84}$$

It may be noted that Eq. (84) for $\hat{C}_{ij}$ and $\hat{D}_{ij}$ also applies to the forced case, since in that case Π is zero.

To conclude, the stochastic model Eq. (78) and Eq. (79) is analyzed in the next section, with the assumptions that $\hat{\mathbf{u}}(\hat{t})$ and $\hat{\mathbf{a}}(\hat{t})$ are statistically stationary. For homogeneous turbulent shear flow, the departures from stationarity are sufficiently small that the results of the analysis can usefully be compared to the DNS data of Sawford and Yeung.[17] This is done in Sec. IV C.

B. Analysis of the stochastic model

In this section we analyze the model in application to homogeneous turbulent shear flow. The analysis is somewhat involved: for the reader wishing to avoid the details, the principal results are summarized in Sec. IV B 6.

1. Model equations

When written for the scaled variables $\hat{\mathbf{u}}(\hat{t})$ and $\hat{\mathbf{a}}(\hat{t})$ in homogeneous turbulent shear flow, the model equations are Eqs. (78) and (79), and the coefficients are given by Eqs. (81) and (84).

It is convenient to use vector-matrix notation, and hence we write the model equations as

$$d\hat{\mathbf{a}}(\hat{t}) = -[\hat{\mathbf{C}}\hat{\mathbf{a}}(\hat{t}) + \hat{\mathbf{D}}\hat{\mathbf{u}}(\hat{t})]d\hat{t} + \hat{\mathbf{B}}\, d\hat{\mathbf{W}}(\hat{t}), \tag{85}$$

$$d\hat{\mathbf{u}}(\hat{t}) = \hat{\mathbf{a}}(\hat{t})d\hat{t}, \tag{86}$$

where the coefficients $\hat{\mathbf{B}}$, $\hat{\mathbf{C}}$, and $\hat{\mathbf{D}}$ are 3×3 matrices. Furthermore, it is convenient to combine $\hat{\mathbf{a}}(\hat{t})$ and $\hat{\mathbf{u}}(\hat{t})$ into a six-vector

$$\mathbf{z}(\hat{t}) \equiv \begin{bmatrix} \hat{\mathbf{a}}(\hat{t}) \\ \hat{\mathbf{u}}(\hat{t}) \end{bmatrix}, \tag{87}$$

so that the model can be written as the single SDE

$$d\mathbf{z}(\hat{t}) = -\mathbf{F}\mathbf{z}(\hat{t})d\hat{t} + \mathbf{E}\, d\bar{\mathbf{W}}(\hat{t}). \tag{88}$$

Here $\bar{\mathbf{W}}(t)$ is a six-vector-valued Wiener process, and the 6×6 matrix coefficients $\mathbf{E}$ and $\mathbf{F}$ are

$$\mathbf{E} = \begin{bmatrix} \hat{\mathbf{B}} & 0 \\ 0 & 0 \end{bmatrix} \tag{89}$$

and

$$\mathbf{F} = \begin{bmatrix} \hat{\mathbf{C}} & \hat{\mathbf{D}} \\ -\mathbf{I} & 0 \end{bmatrix}, \tag{90}$$

where $\mathbf{I}$ is the 3×3 identity matrix.

It is known from the theory of diffusion processes[9,27,32,33] that the diffusion coefficient (e.g., $\hat{\mathbf{B}}$) affects the process only through the symmetric positive–semidefinite from $\hat{\mathbf{B}}\hat{\mathbf{B}}^T$, where "$T$" denotes the transpose. Hence, without loss of generality, $\hat{\mathbf{B}}$ and therefore $\mathbf{E}$ can themselves be taken to be symmetric positive semidefinite.

It is assumed that the eigenvalues of the drift matrix $\mathbf{F}$ have positive real parts, which is a sufficient condition for Eq. (88) to yield a statistically stationary solution.[33]

2. Autocovariance

Since $\mathbf{z}(t)$ is a Gaussian process, its statistics are completely described by its autocovariance, which we define by

$$\mathbf{R}(s) \equiv \langle \mathbf{z}(\hat{t}+s)\mathbf{z}(\hat{t})^T \rangle. \tag{91}$$

It should be noted that this is the transpose of the conventional definition in that the time increment s appears in the first variable. The present definition yields simpler equations in the subsequent analysis.

The autocovariance of $\mathbf{z}(\hat{t})$ can be decomposed into the autocovariances of $\hat{\mathbf{a}}(\hat{t})$ and $\hat{\mathbf{u}}(\hat{t})$:

$$\mathbf{R}(s) = \begin{bmatrix} \mathbf{R}^{aa}(s) & \mathbf{R}^{au}(s) \\ \mathbf{R}^{ua}(s) & \mathbf{R}^{uu}(s) \end{bmatrix}, \tag{92}$$

where

$$\mathbf{R}^{ua}(s) \equiv \langle \hat{\mathbf{u}}(\hat{t}+s)\hat{\mathbf{a}}(\hat{t})^T \rangle, \tag{93}$$

and $\mathbf{R}^{aa}(s)$, $\mathbf{R}^{au}(s)$, and $\mathbf{R}^{uu}(s)$ are similarly defined.

In view of statistical stationarity, the autocovariances are independent of time $\hat{t}$ (as implied by the notation), and they possess the following symmetries:

$$\begin{aligned} &\mathbf{R}(s) = \mathbf{R}(-s)^T, \quad \mathbf{R}^{aa}(s) = \mathbf{R}^{aa}(-s)^T, \\ &\mathbf{R}^{uu}(s) = \mathbf{R}^{uu}(-s)^T, \end{aligned} \tag{94}$$

$$\mathbf{R}^{ua}(s) = \mathbf{R}^{au}(-s)^T = -\mathbf{R}^{au}(s). \tag{95}$$

Stemming from the definition $\hat{\mathbf{a}} = d\hat{\mathbf{u}}/d\hat{t}$, properties of derivatives of the autocovariances are

$$\begin{aligned} &\frac{d}{ds}\mathbf{R}^{uu}(s) = \mathbf{R}^{au}(s), \quad \frac{d}{ds}\mathbf{R}^{ua}(s) = \mathbf{R}^{aa}(s), \\ &\frac{d}{ds}\mathbf{R}^{au}(s) = -\mathbf{R}^{aa}(s), \end{aligned} \tag{96}$$

and hence

$$\frac{d^2\mathbf{R}^{uu}(s)}{ds^2} = -\mathbf{R}^{aa}(s). \tag{97}$$

Thus, all autocovariances [including $\mathbf{R}(s)$] can be determined from $\mathbf{R}^{uu}(s)$.

The covariances are denoted by

$$\mathbf{Q}\equiv\mathbf{R}(0)=\begin{bmatrix}\mathbf{Q}^{aa} & \mathbf{Q}^{au}\\ \mathbf{Q}^{ua} & \mathbf{Q}^{uu}\end{bmatrix}. \tag{98}$$

The covariance matrices $\mathbf{Q}$, $\mathbf{Q}^{aa}$, and $\mathbf{Q}^{uu}$ are symmetric positive definite; while the off-diagonal matrices are [in view of Eq. (95)] antisymmetric and the transposes of each other,

$$\mathbf{Q}^{ua}=-(\mathbf{Q}^{ua})^T=(\mathbf{Q}^{au})^T. \tag{99}$$

It may be observed from Eqs. (96) and (97) that all of the covariances can be obtained from $\mathbf{R}^{uu}(s)$ and its derivatives at the origin ($s=0$).

An important quantity in the subsequent analysis is the *autocorrelation matrix* which is defined by

$$\mathbf{P}(s)\equiv\mathbf{R}(s)\mathbf{Q}^{-1}, \tag{100}$$

and which has the property

$$\mathbf{P}(0)=\mathbf{I}. \tag{101}$$

3. Integral time scales

The matrix $\mathbf{T}$ of integral time scales, which also plays a central role in the analysis, is defined by

$$\mathbf{T}\equiv\int_0^\infty\mathbf{P}(s)ds. \tag{102}$$

This matrix has a special structure, now revealed, which stems from the fact that $\hat{\mathbf{a}}(\hat{t})$ is the derivative of $\hat{\mathbf{u}}(\hat{t})$. We define the 6×6 matrix $\mathbf{M}$ by

$$\mathbf{M}\equiv\int_0^\infty\mathbf{R}(s)ds, \tag{103}$$

which is related to $\mathbf{T}$ by

$$\mathbf{T}=\mathbf{M}\mathbf{Q}^{-1}\quad\text{or}\quad\mathbf{M}=\mathbf{T}\mathbf{Q}, \tag{104}$$

and which is partitioned as

$$\mathbf{M}=\begin{bmatrix}\mathbf{M}^{aa} & \mathbf{M}^{au}\\ \mathbf{M}^{ua} & \mathbf{M}^{uu}\end{bmatrix}. \tag{105}$$

For $\mathbf{M}^{aa}$ we obtain

$$\begin{aligned}\mathbf{M}^{aa}\equiv\int_0^\infty\mathbf{R}^{aa}(s)ds&=\int_0^\infty\langle\hat{\mathbf{a}}(\hat{t}+s)\hat{\mathbf{a}}(\hat{t})^T\rangle ds\\&=\left\langle\int_0^\infty\hat{\mathbf{a}}(\hat{t}+s)ds\,\hat{\mathbf{a}}(\hat{t})^T\right\rangle\\&=\langle[\hat{\mathbf{u}}(\infty)-\hat{\mathbf{u}}(\hat{t})]\hat{\mathbf{a}}(\hat{t})^T\rangle\\&=-\langle\hat{\mathbf{u}}(\hat{t})\hat{\mathbf{a}}(\hat{t})^T\rangle=-\mathbf{Q}^{ua}.\end{aligned} \tag{106}$$

A similar treatment can be applied to $\mathbf{M}^{ua}$ and $\mathbf{M}^{au}$ to show that $\mathbf{M}$ is given by

$$\mathbf{M}=\begin{bmatrix}-\mathbf{Q}^{ua} & -\mathbf{Q}^{uu}\\ \mathbf{Q}^{uu} & \mathbf{M}^{uu}\end{bmatrix}. \tag{107}$$

It then follows that $\mathbf{T}$ is of the form

$$\mathbf{T}=\begin{bmatrix}0 & -\mathbf{I}\\ \mathbf{T}^{ua} & \mathbf{T}^{uu}\end{bmatrix}, \tag{108}$$

since the first row of the product $\mathbf{TQ}$ yields the first row of $\mathbf{M}$ [given by Eq. (107)] in accordance with Eq. (104).

By analogy to Eq. (104), we define the *velocity integral time scale tensor* by

$$\hat{\mathbf{T}}^{uu}\equiv\mathbf{M}^{uu}(\mathbf{Q}^{uu})^{-1}, \tag{109}$$

which is just (the transpose of) the time scale tensor that arises in the analysis of the stochastic model for velocity.[15] And we define the (scalar) Lagrangian velocity integral time scale by

$$T_L\equiv\tfrac{1}{3}\hat{\mathbf{T}}^{uu}_{ii}. \tag{110}$$

We see below that the autocovariance $\mathbf{R}(s)$—and therefore all other statistics—are determined by the covariance matrix $\mathbf{Q}$ and the time scale matrix $\mathbf{T}$ (as previously shown[15]). Because of the special structure of the model, the information content in $\mathbf{Q}$ and $\mathbf{T}$ is less than it appears at first sight. Specifically, the symmetric and nonsymmetric 6×6 matrices $\mathbf{Q}$ and $\mathbf{T}$ can be constructed from the 3×3 matrices $\mathbf{Q}^{aa}$, $\mathbf{Q}^{uu}$, $\mathbf{Q}^{ua}$, and $\hat{\mathbf{T}}^{uu}$—which have an information content equivalent to three symmetric and two antisymmetric 3×3 matrices. It is marvelous—although most likely inevitable—that this is precisely the information content in the model coefficients $\hat{\mathbf{B}}$, $\hat{\mathbf{C}}$, and $\hat{\mathbf{D}}$.

4. Solution for the autocorrelation matrix

It is readily deduced from the model equation, Eq. (88), that the autocovariance satisfies the ODE,

$$\frac{d}{ds}\mathbf{R}(s)=-\mathbf{F}\mathbf{R}(s)\quad\text{for } s\geq0. \tag{111}$$

By post-multiplying both sides of this equation by $\mathbf{Q}^{-1}$, we find that $\mathbf{P}(s)$ [defined by Eq. (100)] satisfies the same equation,

$$\frac{d}{ds}\mathbf{P}(s)=-\mathbf{F}\mathbf{P}(s)\quad\text{for } s\geq0, \tag{112}$$

with the simple initial condition $\mathbf{P}(0)=\mathbf{I}$. The solution to this equation (satisfying the initial condition) is[33]

$$\mathbf{P}(s)=\exp(-\mathbf{F}s)\equiv\sum_{n=0}^{\infty}\frac{(-1)^n}{n!}\mathbf{F}^n s^n\quad\text{for } s\geq0, \tag{113}$$

as may be verified by differentiating with respect to s. It has been assumed that the eigenvalues of $\mathbf{F}$ have positive real part, which is a sufficient condition for $\exp(-\mathbf{F}s)$ to converge to zero as s tends to infinity.

The matrix $\mathbf{F}$ deduced from the DNS (in Sec. IV C) has the simplest structure—real positive eigenvalues, and linearly independent eigenvectors. In that case $\mathbf{F}$ can be decomposed as

$$\mathbf{F}=\mathbf{V}\mathbf{\Lambda}\mathbf{V}^{-1}, \tag{114}$$

where the columns of the 6×6 matrix $\mathbf{V}$ are the eigenvectors of $\mathbf{F}$, and $\mathbf{\Lambda}$ is the 6×6 diagonal matrix of eigenvalues. The solution for $\mathbf{P}(s)$, Eq. (113), can then be re-expressed as

$$\mathbf{P}(s)=\mathbf{V}\exp(-\mathbf{\Lambda}s)\mathbf{V}^{-1} \quad \text{for } s\geqslant 0, \tag{115}$$

showing that $\mathbf{P}(s)$ is a linear combination of six decaying exponentials, the time scales of which are the inverses of the eigenvalues.

For the general case, the time scale matrix $\mathbf{T}$ [Eq. (102)] is obtained as the definite integral of the solution, Eq. (113). The indefinite integral is

$$\int \mathbf{P}(s)ds=-\mathbf{F}^{-1}\exp(-\mathbf{F}s), \tag{116}$$

from which we obtain

$$\mathbf{T}\equiv\int_0^\infty \mathbf{P}(s)ds=\mathbf{F}^{-1}. \tag{117}$$

The 6×6 drift matrix $\mathbf{F}$ is defined in terms of the 3×3 drift matrices $\hat{\mathbf{C}}$ and $\hat{\mathbf{D}}$ in the stochastic model for acceleration by Eq. (90). Given this structure of $\mathbf{F}$, it is readily deduced (from the equation $\mathbf{F}\mathbf{F}^{-1}=\mathbf{I}$) that its inverse is

$$\mathbf{F}^{-1}=\begin{bmatrix} 0 & -\mathbf{I} \\ \hat{\mathbf{D}}^{-1} & \hat{\mathbf{D}}^{-1}\hat{\mathbf{C}} \end{bmatrix}, \tag{118}$$

which, according to Eq. (117), equals $\mathbf{T}$. The first row of $\mathbf{F}^{-1}$ indeed matches that of $\mathbf{T}$ [Eq. (108)], while equating the elements of the second rows yields

$$\mathbf{T}^{ua}=\hat{\mathbf{D}}^{-1}, \quad \mathbf{T}^{uu}=\hat{\mathbf{D}}^{-1}\hat{\mathbf{C}}, \tag{119}$$

or conversely

$$\hat{\mathbf{D}}=(\mathbf{T}^{ua})^{-1}, \quad \hat{\mathbf{C}}=(\mathbf{T}^{ua})^{-1}\mathbf{T}^{uu}. \tag{120}$$

(The assumptions made about $\mathbf{F}$ are sufficient to ensure that $\hat{\mathbf{D}}$ is nonsingular.)

The important conclusions are that there is a one-to-one correspondence between the drift coefficients $\hat{\mathbf{C}}$ and $\hat{\mathbf{D}}$ and the time scale matrices $\mathbf{T}^{uu}$ and $\mathbf{T}^{ua}$ and that the autocorrelation matrix $\mathbf{P}(s)$ is explicitly determined by the drift coefficients $\hat{\mathbf{C}}$ and $\hat{\mathbf{D}}$ [through Eq. (90), Eq. (114), and Eq. (115)]. The autocovariances are given by

$$\mathbf{R}(s)=\mathbf{P}(s)\mathbf{Q}=\exp(-\mathbf{F}s)\mathbf{Q} \quad \text{for } s\geqslant 0, \tag{121}$$

where $\mathbf{F}$ is given in terms of $\hat{\mathbf{C}}$ and $\hat{\mathbf{D}}$ by Eq. (90).

5. Solution for the covariance matrix

The solution is completed by determining the covariance matrix $\mathbf{Q}$. An evolution equation for the covariance is readily derived from the model equation [Eq. (88)], and then the condition that $\mathbf{Q}$ is independent of time yields

$$\mathbf{E}\mathbf{E}^T=\mathbf{E}^2=\mathbf{F}\mathbf{Q}+(\mathbf{F}\mathbf{Q})^T. \tag{122}$$

Thus $\mathbf{E}^2$ is twice the symmetric part of $\mathbf{F}\mathbf{Q}$.

From the definition of $\mathbf{E}$ in terms of $\hat{\mathbf{B}}$ [Eq. (89)] we have

$$\mathbf{E}^2=\begin{bmatrix} (\mathbf{E}^2)^{aa} & (\mathbf{E}^2)^{au} \\ (\mathbf{E}^2)^{ua} & (\mathbf{E}^2)^{uu} \end{bmatrix}=\begin{bmatrix} \hat{\mathbf{B}}^2 & 0 \\ 0 & 0 \end{bmatrix}; \tag{123}$$

and from the definitions of $\mathbf{F}$ [Eq. (90)] and $\mathbf{Q}$ [Eq. (92)] we have

$$\mathbf{F}\mathbf{Q}=\begin{bmatrix} \hat{\mathbf{C}}\mathbf{Q}^{aa}+\hat{\mathbf{D}}\mathbf{Q}^{ua} & \hat{\mathbf{C}}\mathbf{Q}^{au}+\hat{\mathbf{D}}\mathbf{Q}^{uu} \\ -\mathbf{Q}^{aa} & -\mathbf{Q}^{au} \end{bmatrix}. \tag{124}$$

Equation (122) can be used to relate the blocks of $\mathbf{E}^2$ to $\mathbf{F}\mathbf{Q}$, and evidently [from Eq. (123)] only the upper left-hand block is nonzero.

For the lower right-hand block we have, correctly,

$$(\mathbf{E}^2)^{uu}=-\mathbf{Q}^{au}-\mathbf{Q}^{auT}=0, \tag{125}$$

in view of the antisymmetry of $\mathbf{Q}^{au}$ [Eq. (99)]; and in the Appendix it is shown that the off-diagonal blocks are also zero. Thus, the only nonzero block of $\mathbf{E}^2$ given by Eq. (122) is

$$(\mathbf{E}^2)^{aa}=\hat{\mathbf{B}}^2=(\hat{\mathbf{C}}\mathbf{Q}^{aa}+\hat{\mathbf{D}}\mathbf{Q}^{ua})+(\hat{\mathbf{C}}\mathbf{Q}^{aa}+\hat{\mathbf{D}}\mathbf{Q}^{ua})^T. \tag{126}$$

6. Conclusions

The major conclusion now drawn from the analysis is that there is a one-to-one correspondence between the model coefficients ($\hat{\mathbf{B}}$, $\hat{\mathbf{C}}$, and $\hat{\mathbf{D}}$) and the primary statistics ($\mathbf{Q}$ and $\mathbf{T}$). These primary statistics are known in terms of the velocity and acceleration covariances $\mathbf{Q}^{uu}$, $\mathbf{Q}^{ua}$, and $\mathbf{Q}^{aa}$ and the velocity integral time scale tensor $\hat{\mathbf{T}}^{uu}$, Eq. (109).

Given $\mathbf{Q}$ and $\mathbf{T}$, the coefficients $\hat{\mathbf{C}}$ and $\hat{\mathbf{D}}$ are given by Eq. (120), and then $\hat{\mathbf{B}}^2$ is determined by Eq. (126).

Conversely, given the coefficients ($\hat{\mathbf{B}}$, $\hat{\mathbf{C}}$, and $\hat{\mathbf{D}}$), $\mathbf{T}$ is determined by Eq. (119); and the covariances are determined by Eq. (126) together with the equation

$$\mathbf{Q}^{aa}=\hat{\mathbf{C}}\mathbf{Q}^{au}+\hat{\mathbf{D}}\mathbf{Q}^{uu}. \tag{127}$$

This equation is derived in the Appendix, where the solution of Eq. (126) and Eq. (127) for $\mathbf{Q}$ is also discussed. Together these equations yield a linear system which determines $\mathbf{Q}$, but unfortunately an explicit solution is not evident.

Once both the model coefficients and primary statistics are known, then the autocovariance given by the model $\mathbf{R}(s)=\mathbf{P}(s)\mathbf{Q}$ can be determined from Eq. (115). These autocovariances are linear combinations of the six decaying exponentials, $\exp(-\lambda_i s)$, where $\{\lambda_1,\lambda_2,\ldots,\lambda_6\}$ are the eigenvalues of the coefficient matrix $\mathbf{F}$, Eq. (90).

The analysis is complete, since the autocovariances $\mathbf{Q}(s)$ fully characterize the Gaussian model processes $\hat{\mathbf{a}}(\hat{t})$ and $\hat{\mathbf{u}}(\hat{t})$.

For Sawford's model for isotropic turbulence, the eigenvalues of $\mathbf{F}$ are τ/T_∞ and τ/τ_0 (each with multiplicity 3), corresponding to time scales T_∞ and τ_0 [Eq. (56) and Eq. (57)] which scale with the integral time scale and Kolmogorov time scale, respectively. And the time scale matrices are

$$\mathbf{T}^{uu}=\hat{\mathbf{T}}^{uu}=\left(\frac{T_\infty+\tau_0}{\tau}\right)\mathbf{I}=\frac{T_L}{\tau}\mathbf{I} \tag{128}$$

and

$$\mathbf{T}^{ua}=\frac{T_\infty\tau_0}{\tau^2}\mathbf{I}=\frac{\tau_a}{\tau}\mathbf{I}. \tag{129}$$

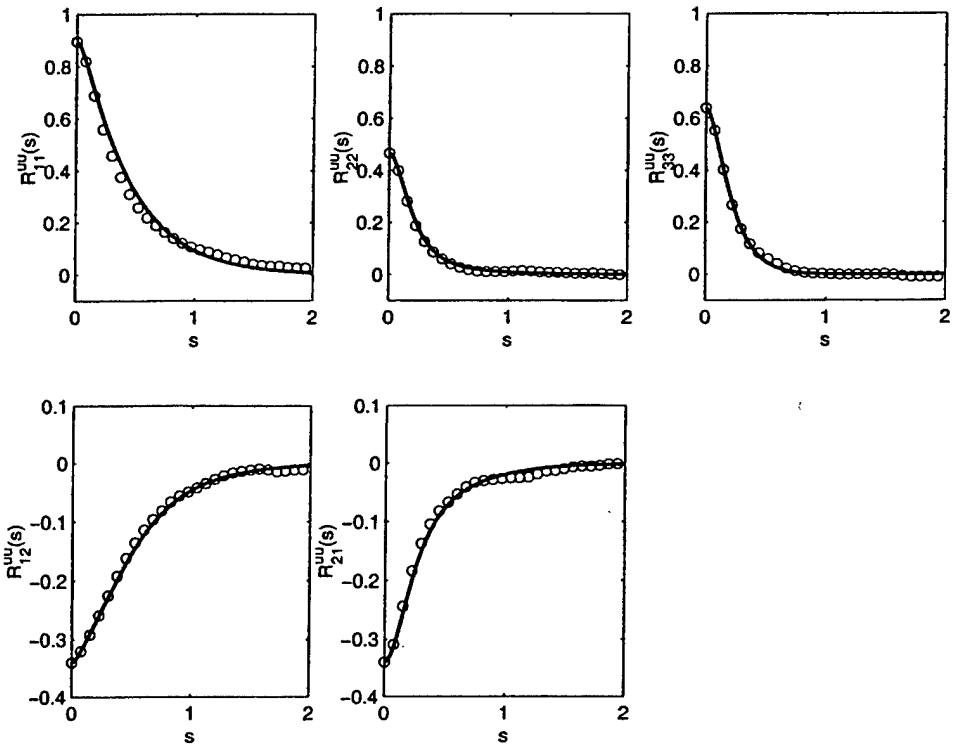

FIG. 1. Velocity autocovariances $\mathbf{R}^{uu}_{ij}(s)$ against normalized time. Symbols, DNS of Sawford and Yeung (Ref. 16); lines, from the acceleration model.

C. Comparison to DNS data

In this section, for the DNS of homogeneous turbulent shear flow,[16] the stochastic model coefficients $\hat{\mathbf{B}}$, $\hat{\mathbf{C}}$, and $\hat{\mathbf{D}}$ are deduced from the data; and then the velocity and acceleration autocovariances predicted by the model are compared to those from the DNS.

All the DNS information is extracted from the time series of the normalized velocity autocovariance $\mathbf{R}^{uu}(s)$. The remaining autocovariances [$\mathbf{R}^{ua}(s)$, $\mathbf{R}^{au}(s)$, and $\mathbf{R}^{aa}(s)$] are obtained from Eq. (96) and Eq. (97) by numerical differentiation of $\mathbf{R}^{uu}(s)$, and then the covariances are obtained as $\mathbf{Q}\equiv\mathbf{R}(0)$. Clearly this differentiation amplifies the statistical noise in the data, as is particularly evident in $\mathbf{R}^{aa}(s)$ (see Fig. 3 below). [In future DNS designed for this purpose, it would be preferable to form all covariances directly from $\hat{\mathbf{a}}(\hat{t})$ and $\hat{\mathbf{u}}(\hat{t})$.]

The velocity covariance integrals $\mathbf{M}^{uu}$ [Eqs. (103) and (105)] are formed from the time series of $\mathbf{R}^{uu}(s)$ by numerical quadrature, and then the matrix of integral time scales $\mathbf{T}$ is obtained from Eq. (104).

Based on the DNS values of the covariances and the velocity integral time scales, the values of the model coefficient $\hat{\mathbf{B}}$, $\hat{\mathbf{C}}$, and $\hat{\mathbf{D}}$ are deduced which lead to the model's matching these statistics. The values of $\hat{\mathbf{C}}$ and $\hat{\mathbf{D}}$ are obtained from Eq. (120), and then $\hat{\mathbf{B}}^2$ from Eq. (126). (The values thus obtained are reported below.) The autocovariances predicted by the model are then deduced from Eqs. (114), (115), and (100).

Figures 1–3 show a comparison of the autocovariances from the DNS (symbols) and from the model (solid lines). Clearly the agreement is excellent, especially for the velocity autocovariances (Fig. 1). It should be noted that an acceleration time scale is not an input to the model, and so the matching of the location and magnitudes of the peaks of $\mathbf{R}^{ua}(s)$ and $\mathbf{R}^{aa}(s)$ in Figs. 2 and 3 is not inevitable.

Figure 4 compares the velocity autocovariances from the DNS, from the present acceleration model, and from the stochastic model for velocity[15] (dashed lines). Only the early times are shown where the differences between the two models are most evident. As may be seen, the acceleration model provides a much more accurate representation of the curvature of the autocovariances at small times. As the Reynolds number increases, the differences between the two models decreases, and is confined to smaller times.

The values of the coefficients $\hat{\mathbf{B}}$, $\hat{\mathbf{C}}$, and $\hat{\mathbf{D}}$ deduced from the DNS are reported in scaled form as $\tilde{\mathbf{B}}$ and $\tilde{\mathbf{D}}$ [defined by Eq. (46)] and $\bar{\bar{\mathbf{C}}}\equiv\tau_a\bar{\mathbf{C}}$. Their values are

$$\tilde{\mathbf{B}}^2=\begin{bmatrix} 0.70 & -0.15 & 0 \\ -0.15 & 0.48 & 0 \\ 0 & 0 & 0.64 \end{bmatrix}, \tag{130}$$

$$\bar{\bar{\mathbf{C}}}=\begin{bmatrix} 0.33 & -0.03 & 0 \\ 0.07 & 0.29 & 0 \\ 0 & 0 & 0.27 \end{bmatrix}, \tag{131}$$

$$\tilde{\mathbf{D}}=\begin{bmatrix} 0.70 & 0.15 & 0 \\ 0.33 & 1.41 & 0 \\ 0 & 0 & 1.11 \end{bmatrix}. \tag{132}$$

Given that $\partial\langle U_1\rangle/\partial x_2$ is the only nonzero velocity gradient, the symmetries in the problem dictate that the off-diagonal components in the third rows and columns of these matrices are zero—as is observed. The magnitudes of all three coef-

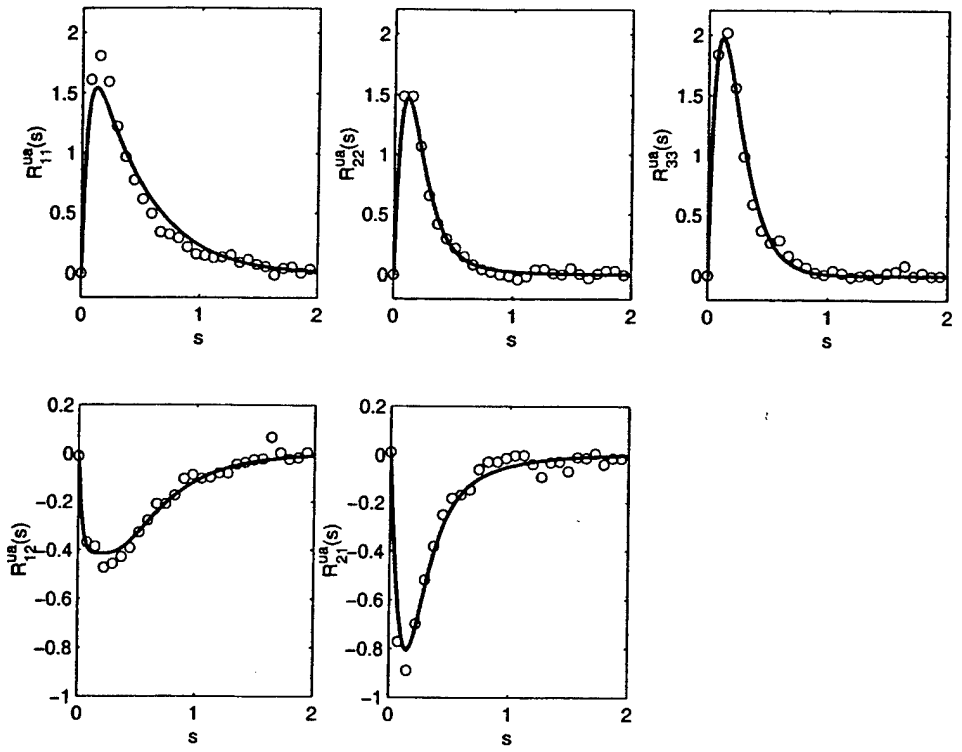

FIG. 2. Velocity-acceleration autocovariances $\mathbf{R}^{ua}_{ij}(s)$ against normalized time. Symbols, DNS of Sawford and Yeung (Ref. 16); lines, from the acceleration model. [Note that $\mathbf{R}^{au}_{ij}(s) = -\mathbf{R}^{ua}_{ij}(s)$.]

ficients are as expected from Eq. (54) given that the velocity integral time scale is $T_L/\tau \approx 0.3$.

As discussed in Sec. III E, if local isotropy prevailed at high Reynolds number, then the acceleration statistics would be isotropic (to leading order in R_λ^{-1}). A sufficient condition for the model to yield such local isotropy is that $\tilde{\mathbf{B}}$ and $\tilde{\mathbf{C}}$ (but not $\tilde{\mathbf{C}}$) become isotropic as the Reynolds number increases. It is evident from Eq. (130) that, at the moderate Reynolds number of the DNS, $\tilde{\mathbf{B}}^2$ exhibits significant anisotropy.

V. APPLICATION TO TURBULENCE MODELLING

The general model proposed here consists of an ODE Eq. (11) for the fluid-particle velocity $\mathbf{U}^*(t)$, which includes

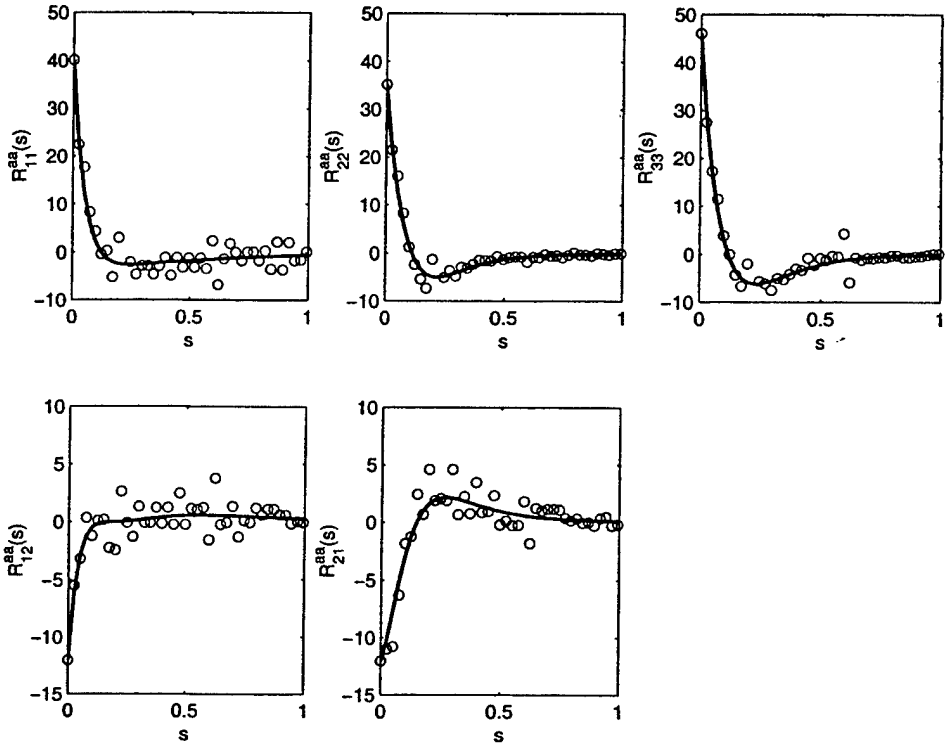

FIG. 3. Acceleration autocovariances $\mathbf{R}^{aa}_{ij}(s)$ against normalized time. Symbols, DNS of Sawford and Yeung (Ref. 16); lines, from the acceleration model.

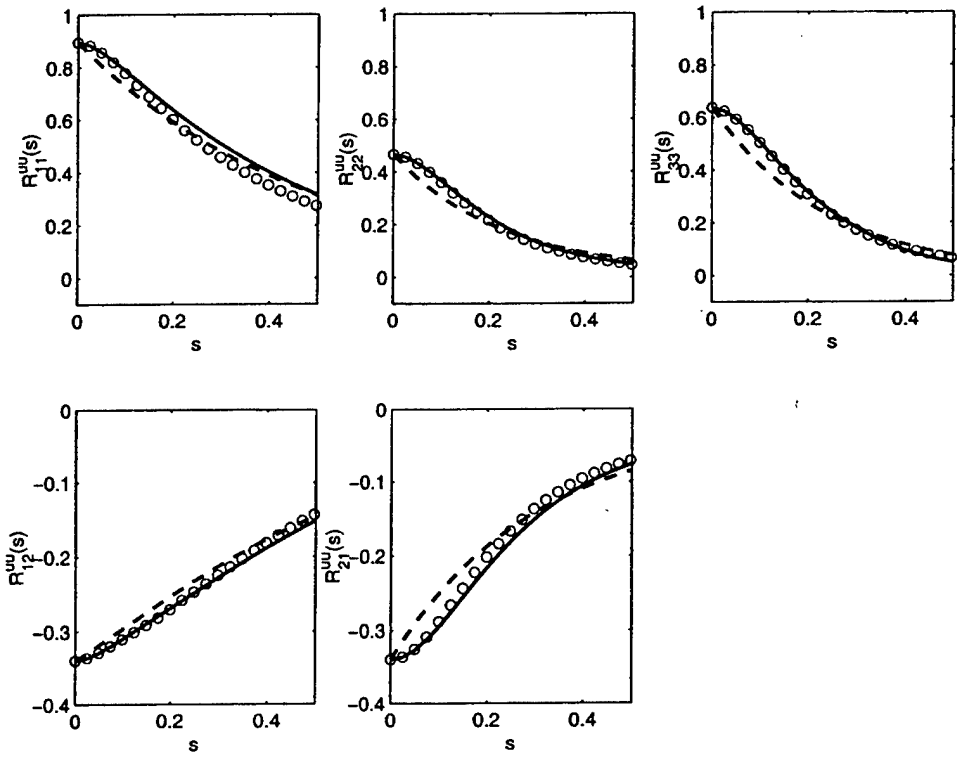

FIG. 4. Velocity autocovariances $\mathbf{R}^{uu}_{ij}(s)$ at early times. Symbols, DNS data of Sawford and Yeung (Ref. 17); solid line, from the acceleration model; dashed line, from the velocity model (Ref. 15).

a rapid-pressure model [Eq. (15)]; and an SDE [Eq. (12)] for the acceleration variable $\mathbf{A}^0(t)$. A specific model consists of a specification of the coefficients appearing in these equations, namely, N_{ijk}, B_{ij}, C_{ij}, and D_{ij}.

Beyond proposing the general model, the objective here is not to suggest a specific model, but rather to show that all of the coefficients can be deduced from DNS data on homogeneous turbulence. Hence, future DNS studies—at different Reynolds numbers and with different imposed mean velocity gradients—can be used to guide the construction of a specific model.

As outlined in the following subsections, the acceleration model can be used at different levels of turbulence modeling. In each case, the turbulent time scale τ is needed, which can be obtained from the standard model equation for ϵ or $\omega \equiv \tau^{-1}$, or from particle models for such quantities.[30,34]

A. Velocity–acceleration–wave-vector model

In addition to the model equations for $\mathbf{U}^*(t)$ and $\mathbf{A}^0(t)$, an additional SDE can be solved for the unit wave vector $\mathbf{e}^*(t)$ (Refs. 9 and 21), so that Eq. (18) can be used as the rapid-pressure model. Such a model has the virtue of representing exactly the evolution of the Reynolds stresses for arbitrary rapid distortions of homogeneous turbulence. Although it has not been convincingly demonstrated, the model should also be capable of providing a more accurate representation of the rapid pressure away from the rapid-distortion limit.

B. Velocity–acceleration model

Without the wave-vector model, the rapid pressure has to be modeled in terms of the particle velocity and Reynolds stresses (among other quantities). The standard model [Eq. (19)] is linear in the velocity, but nonlinear models [e.g., Eq. (24)] can also be considered. It has to be acknowledged that, at this level of closure, there is insufficient directional information to model accurately rapid distortions. But such models may be adequately accurate for the moderate distortions that typically occur in turbulent shear flows.

Compared to a velocity model (discussed in the next section), a velocity-acceleration model has two advantages. First, in essence it models the velocity as a second-order system, Eq. (29), rather than as a first-order system. Consequently, the rapid and slow responses of the turbulence to a sudden change in the mean velocity gradients can be modeled in a natural way. The second advantage is that acceleration is modeled realistically rather than as white noise, and thereby Reynolds number effects can be incorporated in a natural way.

An apparent disadvantage is that, in a numerical implementation, time steps Δt of order τ_a (or equivalently τ_η) are needed to resolve the acceleration time series; whereas with a velocity model the time steps can be of order T_L (or equivalently τ). With time steps of order τ_η, the computational cost increases as $\mathrm{Re}^{1/2}$. However, in most applications the details of the short-time behavior are not required, and temporal resolution on a time scale of order τ is sufficient. It is fortunate, therefore, that the model equations can be solved accurately by numerical methods that take time steps Δt that are large compared to τ_η (but small compared to τ). This is because the model coefficients vary on the time scale τ, and the model equations [e.g., Eq. (25) and Eq. (26)] with frozen coefficients admit analytic solutions. Consequently, if resolution on the Kolmogorov time scale is not required, the velocity-acceleration model can be implemented with a computational cost that is independent of Reynolds number.

C. Velocity model

Given a specific velocity-acceleration model, a corresponding velocity model can be defined—as now outlined.

When applied to (approximately) self-similar homogeneous turbulence (at a given Reynolds number and with given imposed mean velocity gradients), the velocity-acceleration model yields a value of the normalized Reynolds stress tensor ($\mathbf{Q}^{uu}$) and of the velocity integral time scale tensor ($\hat{\mathbf{T}}^{uu}$). The corresponding velocity model is defined to be the linear SDE for velocity that yields these same statistics. The drift and diffusion coefficients in the velocity model are uniquely determined by $\mathbf{Q}^{uu}$ and $\hat{\mathbf{T}}^{uu}$.[15]

[This procedure for determining the velocity-model coefficients is straightforward to implement numerically; but an analytical treatment is hampered by the lack of an explicit solution to Eq. (122) for $\mathbf{Q}$.]

The form of the velocity model thus obtained is the same as the generalized Langevin model (GLM[7,9]) but with an anisotropic diffusion coefficient. The advantage of obtaining a velocity model by this route is that it inherits the Reynolds-number dependence (and other attributes) of the velocity-acceleration model. At very high Reynolds number the acceleration model tends to the GLM with isotropic diffusion, Eq. (67), and with the coefficient G_{ij} given by Eq. (71).

D. Reynolds-stress model

Given a particle model for velocity, it is straightforward to derive a corresponding Reynolds-stress equation.[10,20,35] Again, such a model inherits from its antecedents a Reynolds-number dependence and other attributes.

VI. CONCLUSIONS

We have considered a stochastic model for fluid-particle velocity and acceleration in inhomogeneous turbulent flows. The model consists of an ODE for velocity, Eq. (11), and an SDE for an acceleration variable, Eq. (12). This structure produces the correct qualitative response to rapid distortions. If the model is supplemented by the wavevector equation, then the resulting model [Eq. (15) and Eq. (18)] is exact for arbitrary rapid distortions of homogeneous turbulence. Otherwise, a standard linear model, Eq. (19), for the rapid pressure can be used.

For isotropic turbulence, the SDE for acceleration reduces to Sawford's model.[12] For very high Reynolds number the model is consistent with local isotropy and the Kolmogorov hypotheses, and tends to the generalized Langevin model for velocity. For homogeneous turbulence (with constant and uniform imposed mean velocity gradients) a full analysis of the model is performed. This establishes the one-to-one correspondence between the model coefficient tensors $\mathbf{B}$, $\mathbf{C}$, and $\mathbf{D}$ and the primary statistics of the model, namely, the velocity-acceleration covariances and the velocity integral time scale tensor. Details are given in Sec. IV B 6. For homogeneous turbulence, the modeled processes (i.e., the velocity and acceleration time series) are Gaussian, and hence are completely characterized by their autocovariance, which is given explicitly by Eq. (121). The Gaussianity of acceleration and of multitime velocity statistics is physically incorrect, and reflects the fact that the model does not account for internal intermittency.

For homogeneous turbulent shear flow, the model coefficients are evaluated from the DNS data of Sawford and Yeung.[17] The model autocovariances thus obtained (Figs. 1–4) are in excellent agreement with those from the DNS, including the short-time (Kolmogorov scale) behavior (see Fig. 4).

Compared to a linear stochastic model for velocity, the velocity-acceleration model has the advantage of providing a realistic representation of the behavior on the Kolmogorov time scale; and, as a consequence, of naturally incorporating Reynolds-number effects. The purpose here has not been to propose a specific model (i.e., a specification of the model coefficients), but rather to show that these coefficients can be deduced from DNS of homogeneous turbulence, as functions of the Reynolds number and of the imposed mean velocity gradients.

As discussed in Sec. V, the velocity-acceleration model can be used as a basis for generating a range of (Reynolds-number dependent) PDF and Reynolds-stress turbulence models.

ACKNOWLEDGMENTS

The author is grateful to Professor P. K. Yeung and Dr. B. L. Sawford for making available their DNS data and to Professor R. O. Fox for clarifying the necessary conditions for the satisfaction of Eq. (112). This work was supported by Air Force Office of Scientific Research Grant No. F49620-00-1-0171.

APPENDIX: SOLUTION FOR THE COVARIANCE MATRIX

The purposes of this appendix are to derive Eq. (127); to show that the off-diagonal blocks of $\mathbf{E}^2$ given by Eq. (122) and Eq. (124) are zero; and to discuss the solution of Eq. (126) and Eq. (127) for the covariances.

The covariances are related to the derivatives of the autocovariances at the origin, Eq. (96). From the ODE for the model autocovariance [Eq. (111)] we obtain

$$\left[\frac{d}{ds}\mathbf{R}(s)\right]_{s=0} = -\mathbf{F}\mathbf{Q} = -\begin{bmatrix} \hat{\mathbf{C}} & \hat{\mathbf{D}} \\ -\mathbf{I} & 0 \end{bmatrix}\begin{bmatrix} \mathbf{Q}^{aa} & \mathbf{Q}^{au} \\ \mathbf{Q}^{ua} & \mathbf{Q}^{uu} \end{bmatrix} = \begin{bmatrix} -\hat{\mathbf{C}}\mathbf{Q}^{aa} - \hat{\mathbf{D}}\mathbf{Q}^{ua} & -\hat{\mathbf{C}}\mathbf{Q}^{au} - \hat{\mathbf{D}}\mathbf{Q}^{uu} \\ \mathbf{Q}^{aa} & \mathbf{Q}^{au} \end{bmatrix}. \tag{A1}$$

The bottom row of this last matrix is consistent with the first two relations in Eq. (96); while the consistency of the upper right block with the third relation in Eq. (96) yields

$$\mathbf{Q}^{aa} = \hat{\mathbf{C}}\mathbf{Q}^{au} + \hat{\mathbf{D}}\mathbf{Q}^{uu}, \tag{A2}$$

which is Eq. (127).

The second derivative at the origin is

$$\left[\frac{d^2}{ds^2}\mathbf{R}(s)\right]_{s=0} = \mathbf{F}^2\mathbf{Q}. \tag{A3}$$

By expanding the right-hand side and invoking Eq. (97) we obtain

$$-\left[\frac{d^2}{ds^2}\mathbf{R}^{uu}(s)\right]_{s=0} = \mathbf{Q}^{aa} = \hat{\mathbf{C}}\mathbf{Q}^{au} + \hat{\mathbf{D}}\mathbf{Q}^{uu}, \tag{A4}$$

which provides no new information, but is consistent with Eq. (A2).

From Eq. (122) and Eq. (124), we obtain for the upper right block of $\mathbf{E}^2$,

$$(\mathbf{E}^2)^{au} = \hat{\mathbf{C}}\mathbf{Q}^{au} + \hat{\mathbf{D}}\mathbf{Q}^{uu} - \mathbf{Q}^{aa^T} \tag{A5}$$

$$= \mathbf{Q}^{aa} - \mathbf{Q}^{aa^T} = 0, \tag{A6}$$

where the second line follows from Eq. (A2) and the symmetry of $\mathbf{Q}^{aa}$.

We turn now to the solution of Eq. (126) and Eq. (127) for $\mathbf{Q}^{uu}$, $\mathbf{Q}^{aa}$, and $\mathbf{Q}^{ua}$ given $\hat{\mathbf{B}}$, $\hat{\mathbf{C}}$, and $\hat{\mathbf{D}}$. Recall that $\mathbf{Q}^{uu}$ and $\mathbf{Q}^{aa}$ are symmetric, while $\mathbf{Q}^{ua}$ is antisymmetric. Both sides of Eq. (126) are identically symmetric, whereas the right hand side of Eq. (127) is not identically symmetric. Hence, together, these equations represent a linear system for the components of $\mathbf{Q}^{uu}$, $\mathbf{Q}^{aa}$, $\mathbf{Q}^{ua}$—with the same number of independent equations as the number of independent unknowns, i.e., 15.

It is very unfortunate that there appears not to be a simple explicit solution for the covariances. It should be possible, however, to obtain an explicit solution using tensor representation theorems.[36,37] That is, the covariance can be written

$$\mathbf{Q}^{uu} = \sum_{n=1}^{N_s} r_{uu}^{(n)}\mathbf{S}^{(n)}, \quad \mathbf{Q}^{aa} = \sum_{n=1}^{N_s} r_{aa}^{(n)}\mathbf{S}^{(n)}, \quad \mathbf{Q}^{ua} = \sum_{n=1}^{N_a} r_{ua}^{(n)}\mathbf{A}^{(n)}, \tag{A7}$$

where $\{\mathbf{S}^{(n)}\}$ is a complete set of N_s linearly independent symmetric tensor functions that can be formed for $\hat{\mathbf{B}}$, $\hat{\mathbf{C}}$, and $\hat{\mathbf{D}}$; and similarly $\{\mathbf{A}^{(n)}\}$ is a complete set of N_a antisymmetric tensors. The coefficients $\{r_{uu}^{(n)}\}$, $\{r_{aa}^{(n)}\}$, and $\{r_{ua}^{(n)}\}$ can then be deduced from Eq. (126) and Eq. (127): they are invariants of $\hat{\mathbf{B}}$, $\hat{\mathbf{C}}$, and $\hat{\mathbf{D}}$. However such a solution is unlikely to be simple (or easy to obtain).

[1] G. I. Taylor, "Diffusion by continuous movements," Proc. London Math. Soc. **20**, 196 (1921).
[2] P. Langevin, "Sur la théorie du mouvement Brownien," C.R. Acad. Sci. (Paris) **146**, 530 (1908).
[3] J. C. R. Hunt, "Turbulent diffusion from sources in complex flows," Annu. Rev. Fluid Mech. **17**, 447 (1985).
[4] D. J. Thomson, "Criteria for the selection of stochastic models of particle trajectories in turbulent flows," J. Fluid Mech. **180**, 529 (1987).
[5] B. L. Sawford, "Rotation in Lagrangian stochastic models of turbulent dispersion," Boundary-Layer Meteorol. **93**, 411 (1999).
[6] S. B. Pope, "A Lagrangian two-time probability density function equation for inhomogeneous turbulent flows," Phys. Fluids **26**, 3448 (1983).
[7] D. C. Haworth and S. B. Pope, "A generalized Langevin model for turbulent flows," Phys. Fluids **29**, 387 (1986).
[8] S. B. Pope, "PDF methods for turbulent reactive flows," Prog. Energy Combust. Sci. **11**, 119 (1985).
[9] S. B. Pope, *Turbulent Flows* (Cambridge University Press, Cambridge, 2000).
[10] S. B. Pope, "On the relationship between stochastic Lagrangian models of turbulence and second-moment closures," Phys. Fluids **6**, 973 (1994).
[11] P. K. Yeung and S. B. Pope, "Lagrangian statistics from direct numerical simulations of isotropic turbulence," J. Fluid Mech. **207**, 531 (1989).
[12] B. L. Sawford, "Reynolds number effects in Lagrangian stochastic models of turbulent dispersion," Phys. Fluids A **3**, 1577 (1991).
[13] S. B. Pope, "Lagrangian PDF methods for turbulent flows," Annu. Rev. Fluid Mech. **26**, 23 (1994).
[14] J. Schumacher, "Derivative moments in stationary homogeneous shear turbulence," J. Fluid Mech. **441**, 109 (2001).
[15] S. B. Pope, "Stochastic Lagrangian models of velocity in homogeneous turbulent shear flow," Phys. Fluids **14**, 1696 (2002).
[16] B. L. Sawford and P. K. Yeung, "Eulerian acceleration statistics as a discriminator between Lagrangian stochastic models in uniform shear flow," Phys. Fluids **12**, 2033 (2000).
[17] B. L. Sawford and P. K. Yeung, "Lagrangian statistics in uniform shear flow: direct numerical simulation and Lagrangian stochastic models," Phys. Fluids **13**, 2627 (2001).
[18] S. B. Pope, "Lagrangian microscales in turbulence," Proc. R. Soc. London, Ser. A **333**, 309 (1990).
[19] P. Y. Chou, "On velocity correlations and the solution of the equations of turbulent fluctuation," Q. Appl. Math. **3**, 38 (1945).
[20] S. B. Pope, "Transport equation for the joint probability density function of velocity and scalars in turbulent flow," Phys. Fluids **24**, 588 (1981).
[21] P. R. Van Slooten and S. B. Pope, "PDF modeling of inhomogeneous turbulence with exact representation of rapid distortions," Phys. Fluids **9**, 1085 (1997).
[22] W. C. Reynolds and S. C. Kassinos, "A one-point modeling of rapidly deformed homogeneous turbulence," Proc. R. Soc. London, Ser. A **451**, 87 (1995).
[23] W. Heisenberg, "Zur statistichen Theorie der Turbulenz," Z. Phys. **124**, 628 (1948).
[24] P. Shen and P. K. Yeung, "Fluid particle dispersion in homogeneous turbulent shear," Phys. Fluids **9**, 3472 (1997).
[25] G. A. Voth, K. Satyanarayan, and E. Bodenschatz, "Lagrangian acceleration measurements at large Reynolds number," Phys. Fluids **10**, 2268 (1998).
[26] A. La Porta, G. A. Voth, A. M. Crawford, J. Alexander, and E. Bodenschatz, "Fluid particle accelerations in fully developed turbulence," Nature (London) **409**, 1017 (2001).
[27] L. Arnold, *Stochastic Differential Equations: Theory and Applications* (Wiley, New York, 1974).
[28] S. Tavoularis and S. Corrsin, "Experiments in nearly homogeneous turbulent shear flow with a uniform mean temperature gradient. Part 1," J. Fluid Mech. **104**, 311 (1981).
[29] N. Mordant, P. Metz, O. Michel, and J.-F. Pinton, "Measurement of Lagrangian velocity in fully developed turbulence," Phys. Rev. Lett. **87**, 214501 (2001).
[30] S. B. Pope and Y. L. Chen, "The velocity-dissipation probability density function model for turbulent flows," Phys. Fluids A **2**, 1437 (1990).
[31] C. Beck, "Dynamical foundations of nonextensive statistical mechanics," Phys. Rev. Lett. **87**, 180601 (2001).
[32] S. Karlin and H. M. Taylor, *A Second Course in Stochastic Processes* (Academic, New York, 1981).
[33] C. W. Gardiner, *Handbook of Stochastic Methods for Physics, Chemistry and the Natural Sciences*, 2nd ed. (Springer-Verlag, Berlin, 1985).
[34] P. R. Van Slooten, Jayesh, and S. B. Pope, "Advances in PDF modeling for inhomogeneous turbulent flows," Phys. Fluids **10**, 246 (1998).
[35] P. A. Durbin and C. G. Speziale, "Realizability of second-moment closure via stochastic analysis," J. Fluid Mech. **280**, 395 (1994).
[36] S. B. Pope, "A more general effective-viscosity hypothesis," J. Fluid Mech. **72**, 331 (1975).
[37] S. Pennisi, "On third order tensor-valued isotropic functions," Int. J. Eng. Sci. **30**, 679 (1992).